ANL/ESD/11-56

Computational Mechanics Research and Support for Aerodynamics and Hydraulics at TFHRC, Year 1 Quarter 4 Progress Report

Energy Systems Division

About Argonne National Laboratory

Argonne is a U.S. Department of Energy laboratory managed by UChicago Argonne, LLC under contract DE-AC02-06CH11357. The Laboratory's main facility is outside Chicago, at 9700 South Cass Avenue, Argonne, Illinois 60439. For information about Argonne and its pioneering science and technology programs, see www.anl.gov.

Availability of This Report

This report is available, at no cost, at http://www.osti.gov/bridge. It is also available on paper to the U.S. Department of Energy and its contractors, for a processing fee, from:

U.S. Department of Energy
Office of Scientific and Technical Information
P.O. Box 62
Oak Ridge, TN 37831-0062
phone (865) 576-8401
fax (865) 576-5728
reports@adonis.osti.gov

ANL/ESD/11-56

Computational Mechanics Research and Support for Aerodynamics and Hydraulics at TFHRC, Year 1 Quarter 4 Progress Report

by
S.A. Lottes, R.F. Kulak, and C. Bojanowski
Transportation Research and Analysis Computing Center (TRACC)
Energy Systems Division, Argonne National Laboratory

November 2011

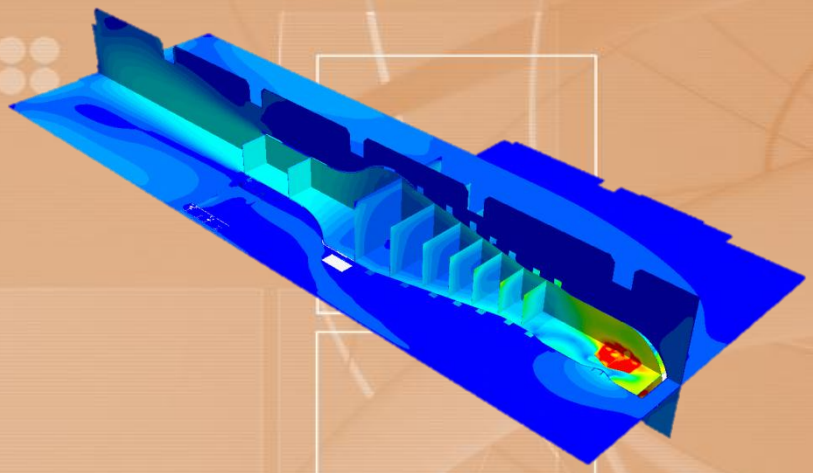

Argonne NATIONAL LABORATORY

Computational Mechanics Research and Support for Aerodynamics and Hydraulics at **TFHRC**

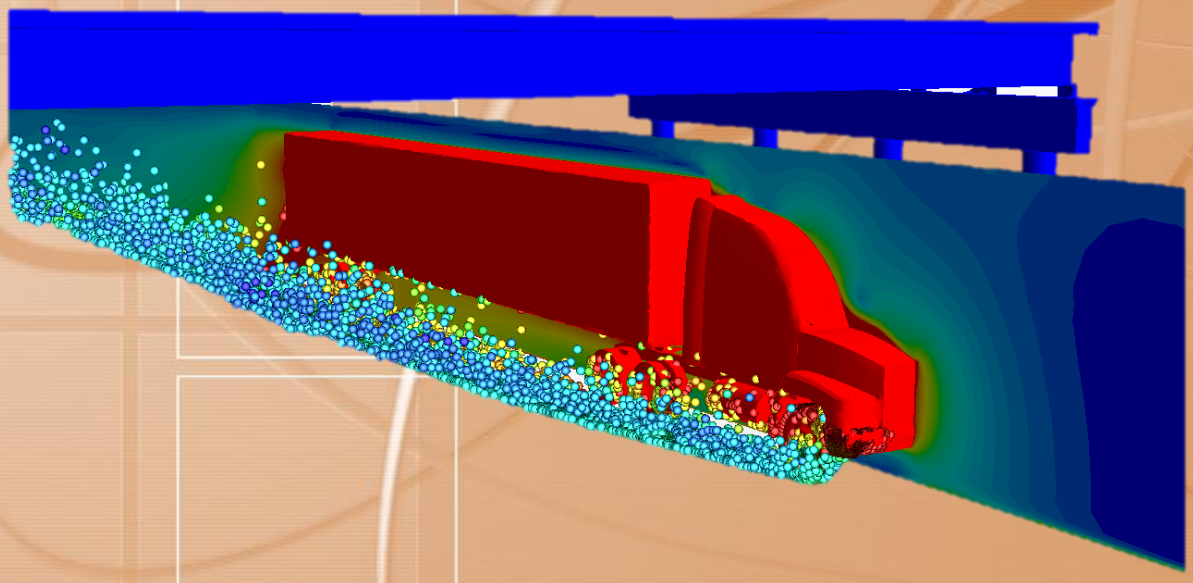

Quarterly Report

July through September 2011

Y1Q4

Computational Mechanics Research and Support for Aerodynamics and Hydraulics at TFHRC
Year 1 Quarter 4 Progress Report

Energy Systems Division (ES)
Argonne National Laboratory (ANL)

Principal Investigators:
Steven A. Lottes, Ph.D.

Ronald F Kulak, Ph.D., PE, FASME

Contributor:
Cezary Bojanowski, Ph.D.

Submitted to:
Federal Highway Administration

Kornel Kerenyi, Ph.D.
Turner-Fairbank Highway Research Center
Federal Highway Administration
6300 Georgetown Pike
McLean, VA 22101

Harold Bosch, Ph.D.
Turner-Fairbank Highway Research Center
Federal Highway Administration
6300 Georgetown Pike
McLean, VA 22101

November 2011

Table of Contents

List of Figures

List of Tables

1. Introduction and Objectives

The computational fluid dynamics (CFD) and computational structural mechanics (CSM) focus areas at Argonne's Transportation Research and Analysis Computing Center (TRACC) initiated a project to support and compliment the experimental programs at the Turner-Fairbank Highway Research Center (TFHRC) with high performance computing based analysis capabilities in August 2010. The project was established with a new interagency agreement between the Department of Energy and the Department of Transportation to provide collaborative research, development, and benchmarking of advanced three-dimensional computational mechanics analysis methods to the aerodynamics and hydraulics laboratories at TFHRC for a period of five years, beginning in October 2010. The analysis methods employ well-benchmarked and supported commercial computational mechanics software. Computational mechanics encompasses the areas of Computational Fluid Dynamics (CFD), Computational Wind Engineering (CWE), Computational Structural Mechanics (CSM), and Computational Multiphysics Mechanics (CMM) applied in Fluid-Structure Interaction (FSI) problems.

The major areas of focus of the project are wind and water effects on bridges — superstructure, deck, cables, and substructure (including soil), primarily during storms and flood events — and the risks that these loads pose to structural failure. For flood events at bridges, another major focus of the work is assessment of the risk to bridges caused by scour of stream and riverbed material away from the foundations of a bridge. Other areas of current research include modeling of flow through culverts to assess them for fish passage, modeling of the salt spray transport into bridge girders to address suitability of using weathering steel in bridges, CFD analysis of the operation of the wind tunnel in the TFCHR wind engineering laboratory, vehicle stability under high wind loading, and the use of electromagnetic shock absorbers to improve vehicle stability under high wind conditions.

This quarterly report documents technical progress on the project tasks for the period of July through September 2011.

1.1. Computational Fluid Dynamics Summary

The primary Computational Fluid Dynamics (CFD) activities during the quarter concentrated on the development of models and methods needed to complete the next steps in scour and culvert modeling.

During this quarter, modeling and analysis of the separation of flow at the leading edge of a flooded bridge deck was begun to aid in the development of an enhanced approach for evaluating scour due to submergence of bridge decks during floods in the federal guidelines. Modeling of flow through culverts for fish passage continued with the addition of a porous media model to capture the effects of large diameter gravel in the bottom of the culvert. TFHRC provided geometry files for their wind tunnel laboratory, and a new CFD model was developed to analyze flow in the wind tunnel and the room under a variety of flow conditions including with and without furniture. A CFD model using the sliding mesh capabilities of STAR-CCM+ with multiphase droplet tracking was developed and tested for application to the analysis of the interaction of road salt spray from large truck traffic with bridges using weathering steel beams.

1.2. Computational Multiphyics Mechanics Summary

Research for the Turner-Fairbank Highway Research Center during this quarter focused on vehicle stability under high crosswind loading conditions. This is a Master of Science thesis topic for a student at Northern Illinois University. Numerical simulations on a finite element model of an 8000S vehicle (e.g., a Ford F800 single unit truck) subjected to several high wind conditions were performed. Based on vehicle speed and wind velocities, regions in which sideslip and rollover occur were identified. A second thesis topic was the development of an electromagnetic shock absorber control algorithm that can increase the stability of trucks driving in high wind conditions. Preliminary results show that the algorithm does offer an improvement in terms of reducing the acceleration of the sprung and unsprung masses, thus, potentially making the vehicle more stable in high winds.

2. Computational Fluid Dynamics for Hydraulic and Aerodynamic Research

During the fourth quarter modeling and analysis of the separation of flow at the leading edge of a flooded bridge deck was begun to aid in the development of an enhanced approach for evaluating scour due to submergence of bridge decks during floods. Modeling of flow through culverts for fish passage continued with the addition of a porous media model to capture the effects of large diameter gravel in the bottom of the culvert. TFHRC provided geometry files for their wind tunnel laboratory and a new CFD model was developed to analyze flow in the wind tunnel and the room under a variety of flow conditions including with and without furniture. A CFD model using the sliding mesh capabilities of STAR-CCM+ with multiphase droplet tracking was developed and tested for application to the analysis of road salt spray from large truck traffic under bridges with weathering steel.

2.1. CFD Analysis of Flow Separation under an Inundated Bridge Deck for Application to Pressure Scour Evaluation

An update to the submerged-flow bridge scour evaluation procedure in HEC 18 [1] is being prepared by TFHRC. The approach to scour hole estimation assumes that the scour process will enlarge the area under the bridge until it is large enough to pass the flow with a condition of critical shear stress at the bed. The bridge deck is a bluff body in the flow and flow separation will normally occur at the upstream bottom edge of the submerged bridge deck. The separation zone under the bridge restricts the area open to flow under the deck and is therefore an important parameter in conservatively predicting the depth of the scour hole. A set of CFD simulations were performed to investigate the relation between the initial opening height under the submerged deck before scour and the thickness of the separation zone, and one test was done to see if the thickness of the separation zone changed during the scour process.

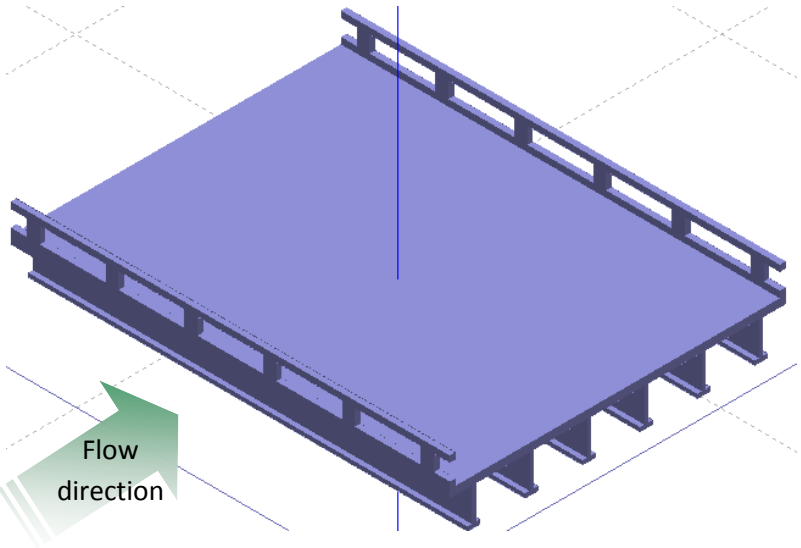

Figure 2.1: Bridge deck geometry

The bridge deck geometry is shown in Figure 2.1, and a schematic of the flow domain is shown in Figure 2.2. To reduce computer time and eliminate the effects of the flume side walls, the simulations were performed using a section of the bridge deck cut through the middle of a post and running half the distance to the center of the next post. This geometry is shown in Figure 2.3.

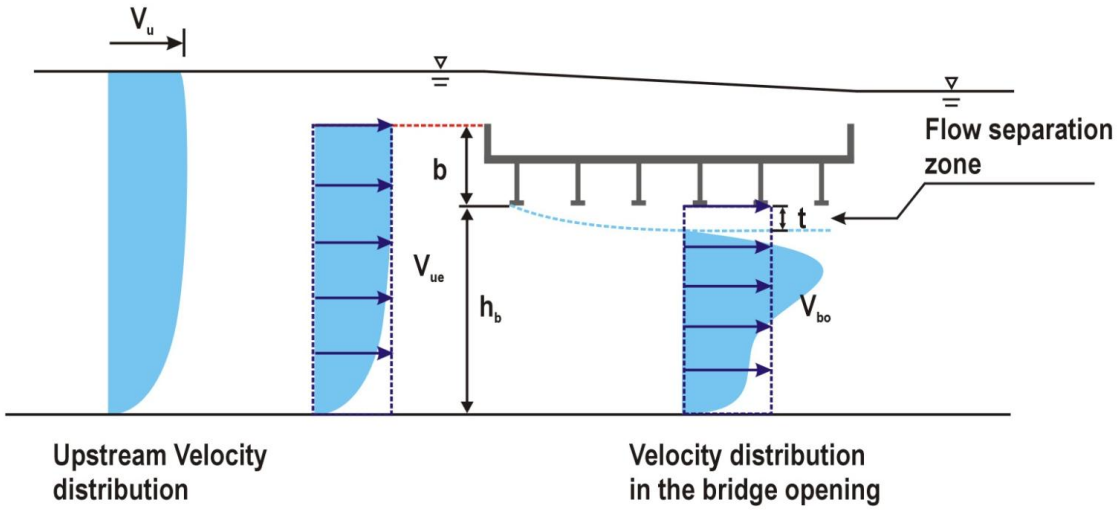

Figure 2.2: Schematic of flow domain for separation zone simulations

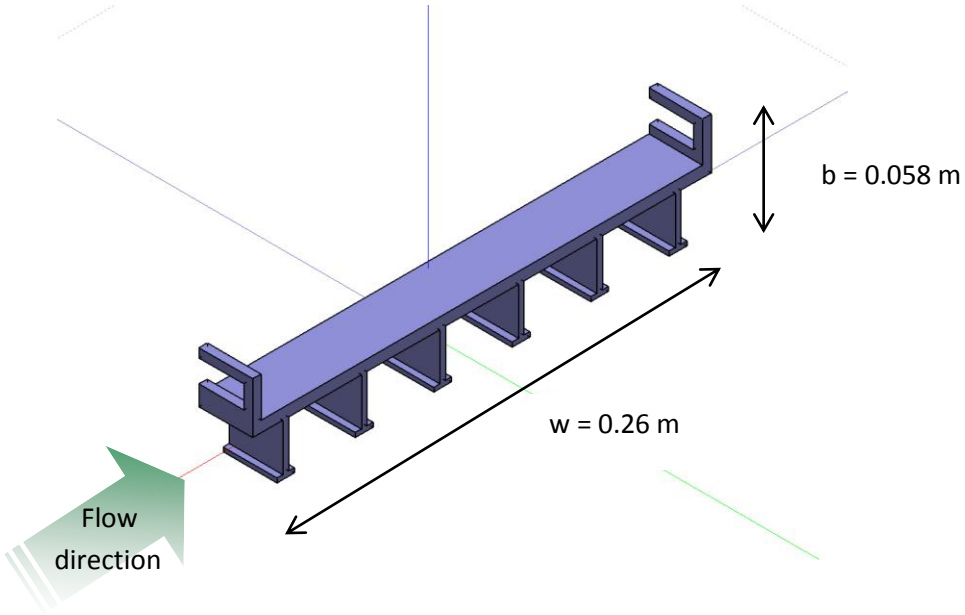

Figure 2.3: Symmetric section of bridge deck from center of a railing post to halfway to the next post

Symmetric boundary conditions were used on the cross stream sides of the domain. The simulations were done as single phase flow with a flat water surface using a symmetry boundary condition at the surface. Previous tests have been done using the multiphase VOF model for free surface flow, and the

flat surface assumption is good except in the case with the bridge deck very close to the surface but still overtopped. The inlet boundary was taken to be a uniform velocity located just at the outlet of the honeycomb in the TFHRC scour flume. The honeycomb is a flow straightener that also strips off boundary layers, and therefore the uniform inlet velocity is a reasonably good assumption applied at this position.

2.1.1. Separation Zone Before and After Scour Hole Formation

To determine the effect of scour hole formation on the size of the separation zone below the bridge deck, the maximum thickness of the separation zone before and after scour was calculated using an existing scour model that does not include sediment transport. The model is based on a TFHRC scour experiment with water depth of 25 cm, bridge height above the bed, h_b, of 16 cm, and mean inlet flow velocity of 0.482 m/s. Figure 2.4: shows the velocity field under the deck for the initial un-scoured flat bed. High velocity under the deck caused by the deck blockage in the flow causes scour of the bottom. The velocity distribution under the deck after scour in shown in Figure 2.5: plotted using the same scale as the flat bed pre-scour condition. The reduced velocity under the deck is apparent. With the scour hole present the maximum shear stress under the deck is reduced to the critical shear stress.

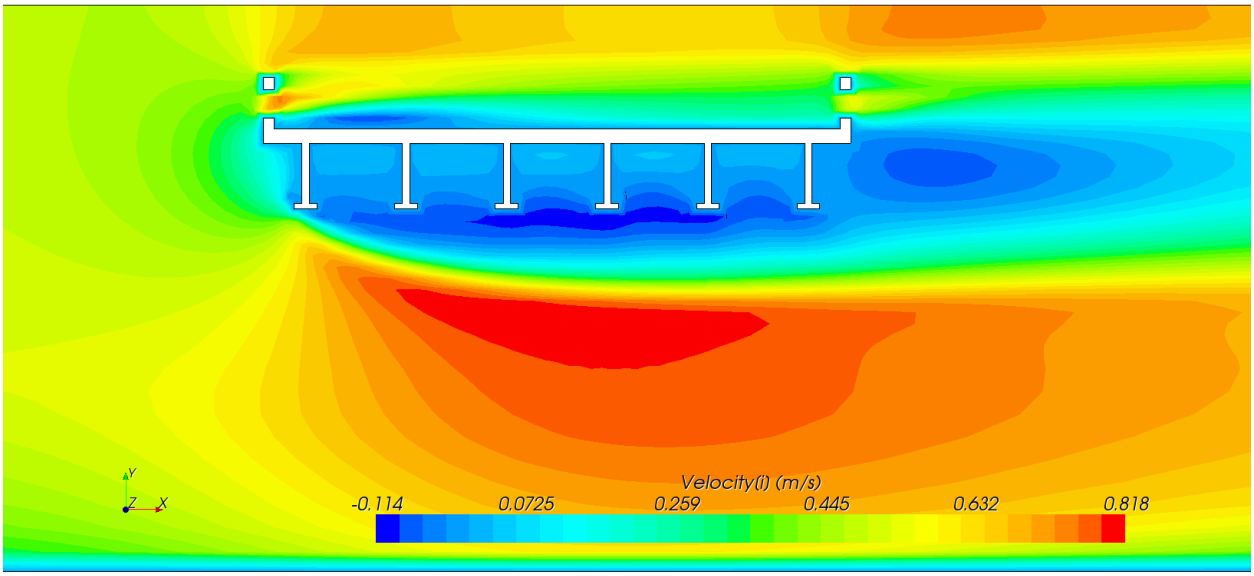

Figure 2.4: Velocity field under bridge deck before scour

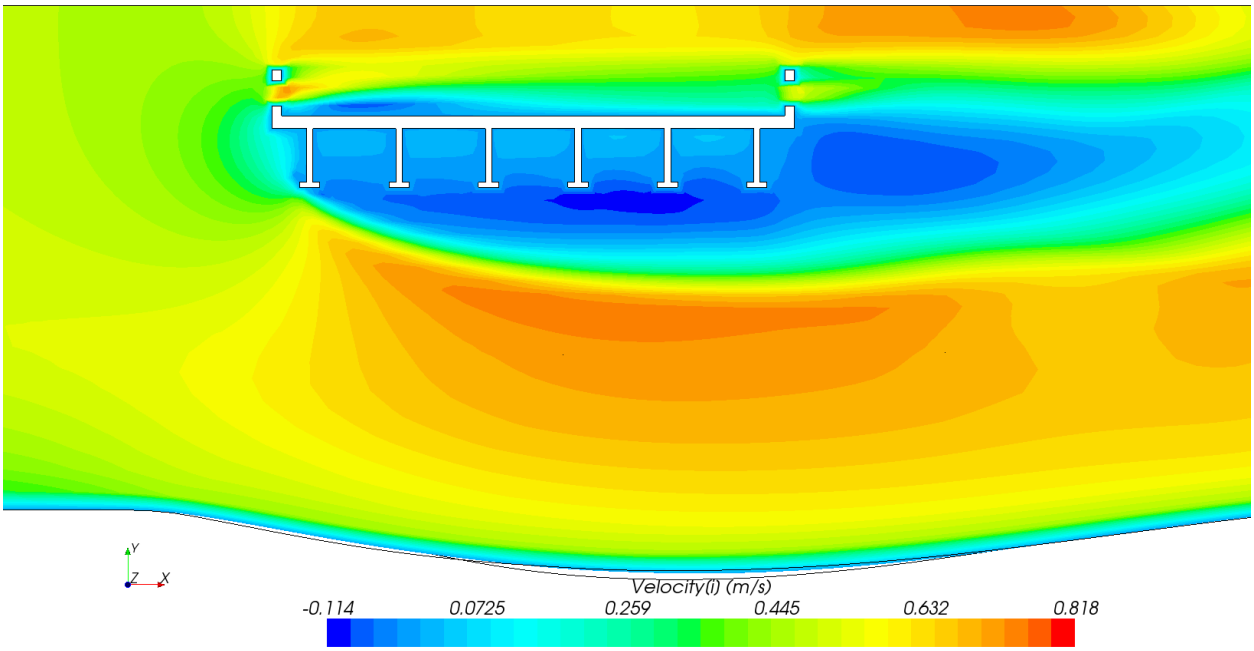

Figure 2.5: Velocity field under bridge deck after scour

Velocity profiles in the upstream of the deck (blue line) and 15 cm under the deck (red line) before scour are shown in Figure 2.6:. The negative x-direction velocity due to recirculation in the separation zone beneath the deck can be seen.

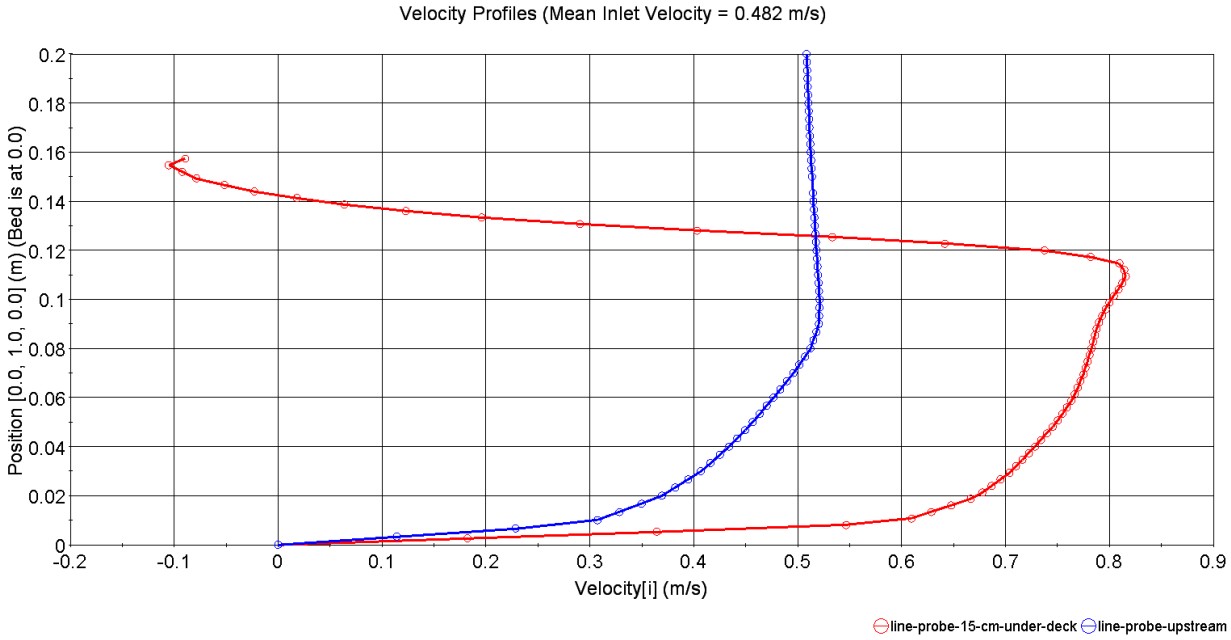

Figure 2.6: Velocity profiles upstream and 15 cm under the deck

The size of the separation zone for both the pre and post scour conditions is determined by computing the streamline that starts from the leading edge at the bottom of the first I-beam. A plot of this streamline for the pre scour condition is shown in Figure 2.7:. It is colored with the height above the flume bed. The maximum thickness of the separation zone is determined by using a STAR-CCM+ report to find the minimum height of the streamline at the zone boundary above the bed and subtracting the result from the height of the deck above the bed in another report. For the pre scour condition, the thickness of the separation zone is 0.033 m. For the post scour condition, the thickness of the separation zone grows to 0.046 m. Therefore, the larger opening under the deck when the scour hole has formed does lead to a larger separation zone under the bridge deck.

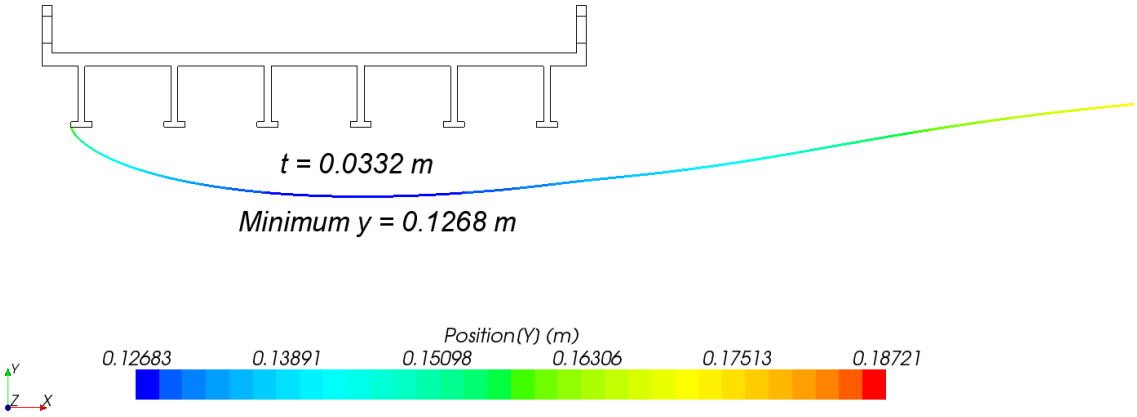

Figure 2.7: Streamline bounding the separation zone under the deck before scour

The qualitative differences in the separation zones for the pre and post scour conditions can also be seen in Figure 2.8: and Figure 2.9:. These figures show a set of streamlines seeded from a line upstream of the deck blockage. The stagnation point on the upstream side of the deck is approximately at the height of the road surface, and with more area for flow under the deck after the scour hole forms, the stagnation point moves only slightly downward. The separation zone leading into the wake is larger when the scour hole is present. The maximum thickness increases from 0.033 m to 0.46 m and the position of the point of maximum thickness moves from 14 cm downstream of the leading edge of the first I-beam to 18 cm downstream of the leading edge.

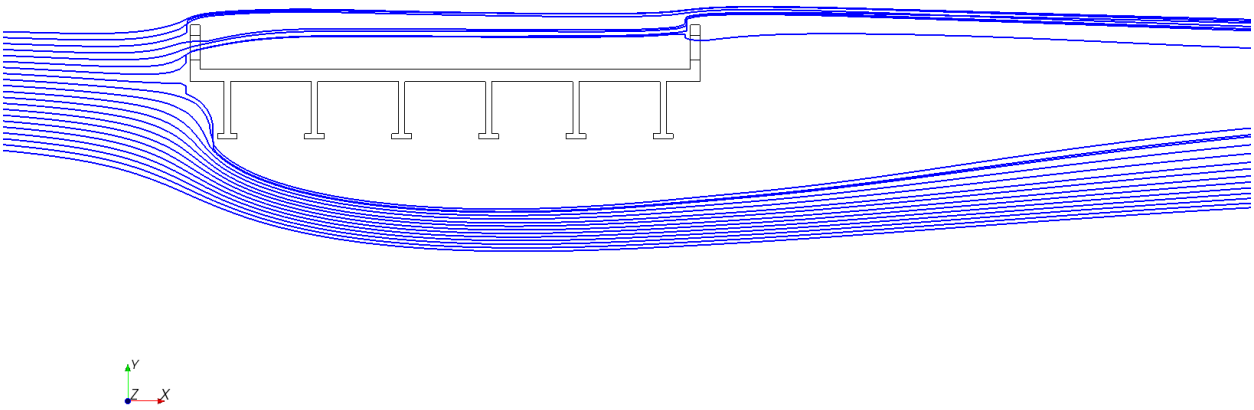

Figure 2.8: Streamlines seeded from the upstream of the deck blockage showing the stagnation point before scour

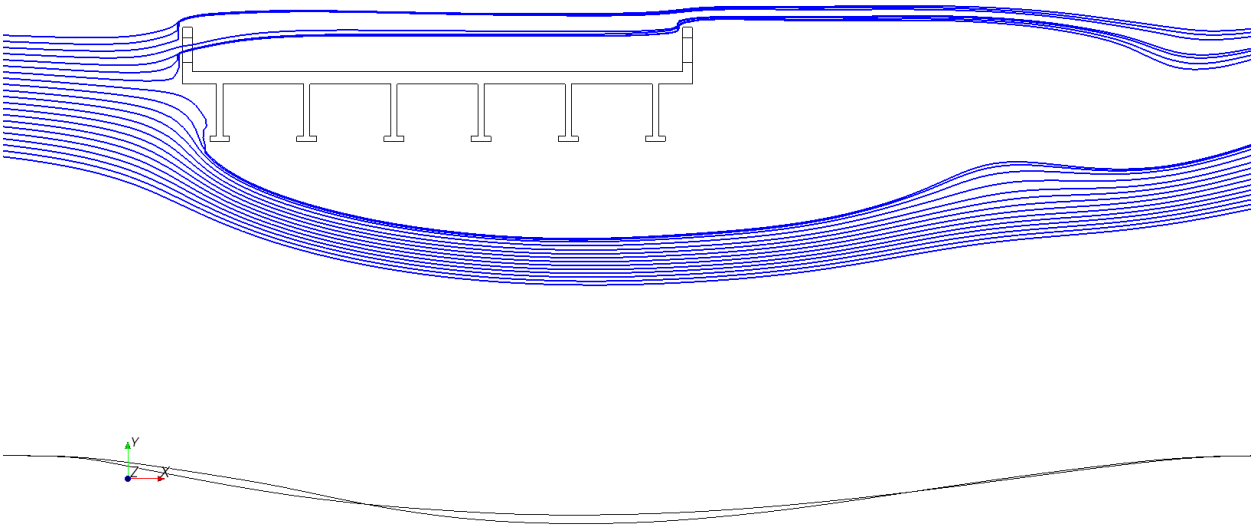

Figure 2.9: Streamlines seeded from the upstream of the deck blockage showing the stagnation point with scour hole present

2.1.2. Relation between Separation Zone Thickness and Bridge Height above Bed

A set of simulations were done to test the relation between the height of the bridge deck above the sediment bed and the maximum thickness of the separation zone. For these cases the water depth was 0.5 m, and inlet flow velocities of 0.6 m/s and 0.4 m/s were used. The set of bridge openings, h_b, and the maximum contraction created by the separation zone, t, under the deck are listed in Table 2.1. The thickness of the separation zone is not affected much by velocity within the range tested.

Table 2.1 Contraction of flow under bridge deck

Bridge Opening h_b (m)	Maximum Contraction V_u = 0.6 m/s (m)	Maximum Contraction V_u = 0.4 m/s (m)
0.05	0.013	0.013
0.10	0.021	0.021
0.15	0.026	0.027
0.30	0.036	0.036
0.42	0.052	0.051
0.47	0.048	0.046

Figure 2.10 and Figure 2.11 show the bounding streamlines for fully submerged cases where the deck is close to the bed, h_b = 5 cm and where the deck is at the highest point tested that still has significant overtopping, h_b = 30 cm. The separation zone is relatively thin and short for the case with the deck near the bed, and it grows in thickness with the thickest point moving to the downstream edge of the deck at a deck height of h_b = 30 cm.

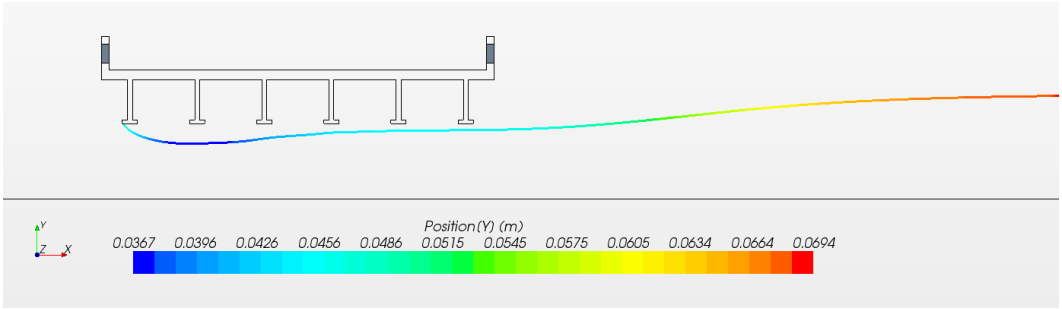

Figure 2.10: Separation zone bounding streamline for h_b = 0.05 m case

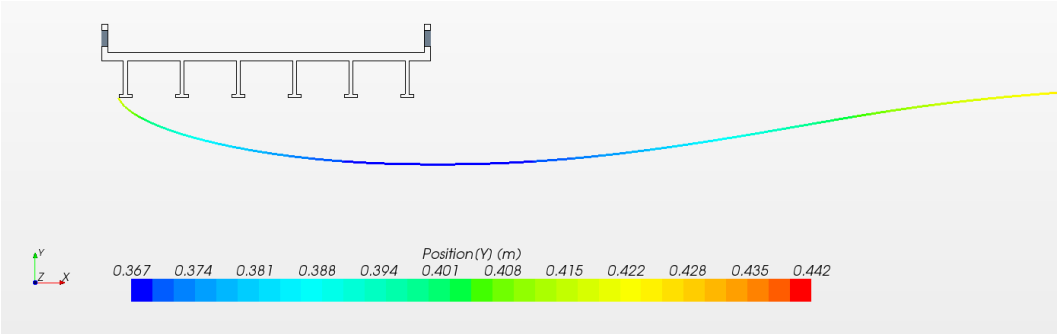

Figure 2.11: Separation zone bounding streamline for h_b = 0.30 case

The relation of deck height above the bed to the vertical contraction created by flow separation at the leading edge of the first I-beam is shown in Figure 2.12. The vertical contraction, which is the same as the thickness of the separation zone, t, increases nearly linearly with the height above the bed until the bridge deck is not fully submerged at h_b = 0.47.

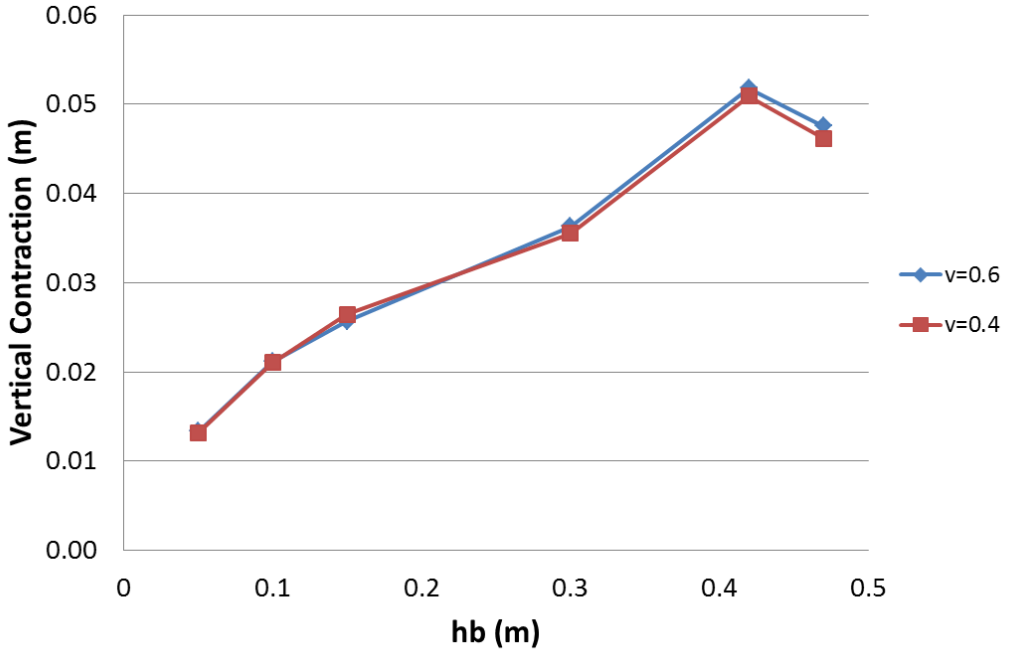

Figure 2.12: Vertical contraction of flow under bridge deck as a function of the height of the deck above the bed showing a dip at 0.47 when the deck is not fully submerged

2.2. Computational Modeling and Analysis of Flow through Large Culverts for Fish Passage

Fish passage through culverts is an important component of road and stream crossing design. As water runoff volume increases, the flow often actively degrades waterways at culverts and may interrupt natural fish migration. Culverts are fixed structures that do not change with changing streams and may instead become barriers to fish movement. The most common physical characteristics that create barriers to fish passage include excessive water velocity, insufficient water depth, large outlet drop heights, turbulence within the culvert, and accumulation of sediment and debris. Major hydraulic criteria influencing fish passage are: flow rates during fish migration periods, fish species, roughness, and the length and slope of the culvert.

The objective of this work is to develop approaches to CFD modeling of culvert flows and to use the models to perform analysis to assess flow regions for fish passage under a variety of flow conditions. The flow conditions to be tested with CFD analysis are defined in the tables of a work plan from TFHRC [6]. The CFD models are being verified by comparing computational results with data from experiments conducted at TFHRC. A primary goal of CFD analysis of culverts for fish passage is to determine the local cross section velocities and flow distributions in corrugated culverts under varying flow conditions. In order to evaluate the ability of fish to traverse corrugated culverts, the local average velocity in vertical strips from the region adjacent to the culvert wall out to the centerline under low flow conditions will be determined.

A primary goal of the CFD analysis during this quarter has been to investigate methods to model gravel in the culvert. The test matrix in the TFHRC work plan [6] includes tests with the bed height at 15% and 30% of the culvert diameter. For these cases, the culvert bed material is coarse gravel with a mean diameter, D_{50} = 12 mm. At this gravel size, the gravel bed boundary cannot be treated as a rough wall using wall functions because the centroid of the near wall computational cell must be at a position that is greater than the roughness height. For 12 mm gravel, the near wall mesh would be far too large for the analysis results to be mesh independent. Two options to model flow parallel to a porous gravel bed are (1) to treat the bed as a porous media, with a flat interface dividing the two flow zones, and (2) to mesh out the rough bed contour created by the top layer of gravel. The methods for generating various velocity averages over a cross section from the work plan [6] that may be applied in improved fish passage analysis are summarized in Section 2.2.1, and example results from a test case are presented.

2.2.1. Velocity Curves for Culverts

2.2.1.1. Local Depth-Averaged Velocity Curve Development

Flow velocity and flow depth are two important factors influencing fish activity in a culvert. Figure 2.13 illustrates the information that was measured in the flume and was calculated by the numerical modeling methods described below. At a given culvert cross-section, flow depth, and flow discharge, the local depth-averaged velocities V_1, V_2, V_3, etc. are measured at regular offsets from the culvert wall. Typically the local depth-averaged velocity will approach zero at the culvert wall and will be at a maximum near the center of the culvert.

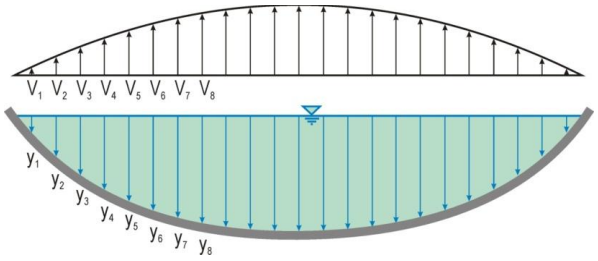

Figure 2.13: Variation of flow velocity and depth in a cross-section of a corrugated metal pipe

In the numerical modeling, the culvert cross-section is divided into evenly spaced strips, and then the grid's discharge and area in each strip are determined by integrating over the strip. The ratio of the integrated discharge and integrated area is the depth-averaged velocity. In this study, a trimmed cell mesh was used to generate an extremely high quality hexahedral-based mesh for the culvert geometry. This kind of mesh model gives a structured mesh across the culvert section that is well suited for computing strip averages because the grid can be built to align cell faces with strip boundaries. When these boundaries are not aligned with cell faces, velocity data in uniform vertical strips in the cross-section are generated by interpolating the original grid velocity data from STAR-CCM+. The exported data is then used to get the depth averaged velocity distribution over the strips by averaging the velocities falling in each strip with MATLAB. The results are shown in Figure 2.14.

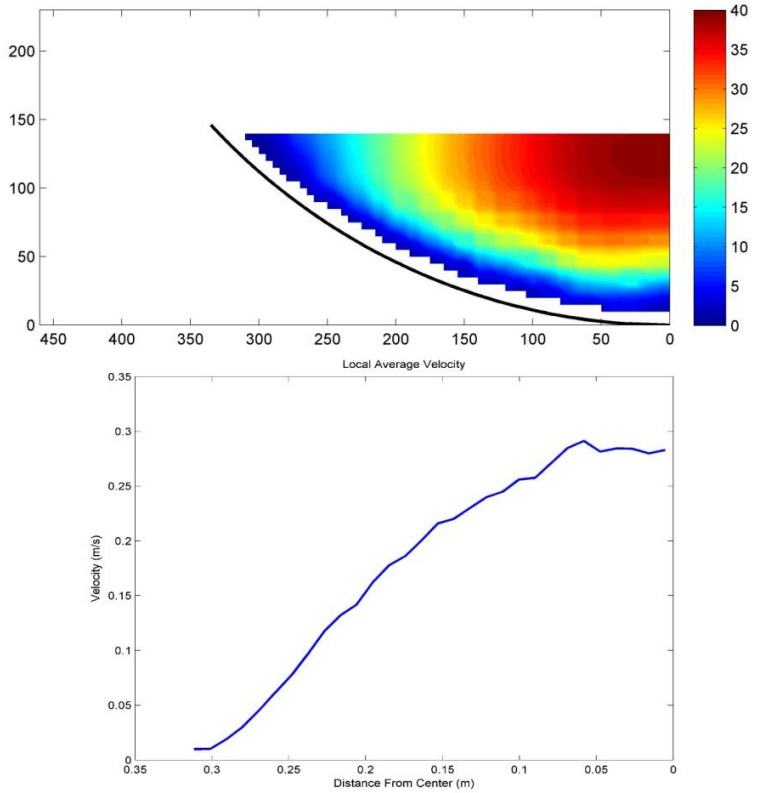

Figure 2.14: Depth-averaged velocity curve development in a cross-section of 6 inch water depth with symmetry boundary

In a similar manner, the local flow depths y1, y2, y3 can be measured at the same offsets from the wall that are used for the velocity readings. These depths can be related to the maximum flow depth y_{max} through the culvert geometry. The relationship between the local depth-averaged velocity V and the local depth y of the flow at any point in the culvert cross-section is the important information needed for the Aquatic Organism Passage design of the culvert. The fish design criteria, can be provided by the appropriate environmental agency as noted in the discussion of Tables 1A and B in the work plan [6]. The next step is to predict velocity distribution and depth variations through culverts under various conditions, including flow depths, inlet velocities, bed elevations, and roughness. A path through a culvert suitable for fish passage can be defined for the given conditions from strip depth average velocities. The fish path in the culvert is shown in Figure 2.15.

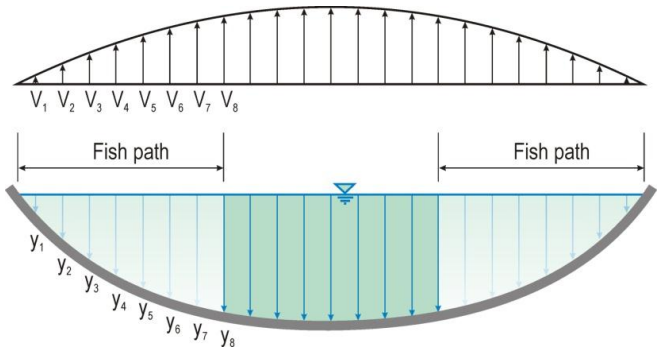

Figure 2.15: Flow path for the selected fish design criteria of velocity and depth

In Figure 2.15, one end of the path is defined by the culvert wall. The other end of the path, towards the center of the culvert, is defined by the point where the local depth-averaged flow velocity V is equal to the maximum fish swimming velocity, V_F , as defined by the appropriate standard. In this illustration example $V_8 = V_F$. Note that another limit to the fish path can be the water depth when the depth in a strip is less than that required for larger species of fish, such as trout or salmon.

2.2.1.2. Average Velocity Curve Development

The area (A) and volume flow rate (Q) of the flow within the limits of the fish path also can be computed, and the average velocity of the flow within the fish path can be computed as illustrated below in Figure 2.16 and Figure 2.17.

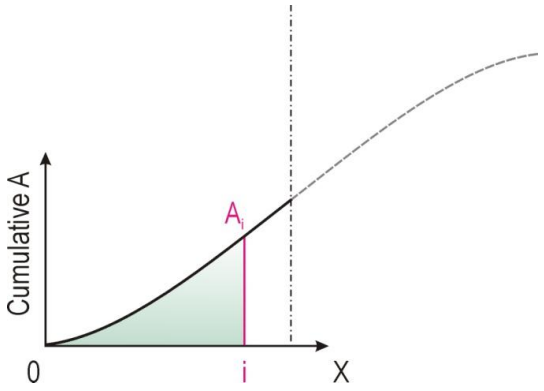

Figure 2.16: Cumulative area from the wall to the centerline

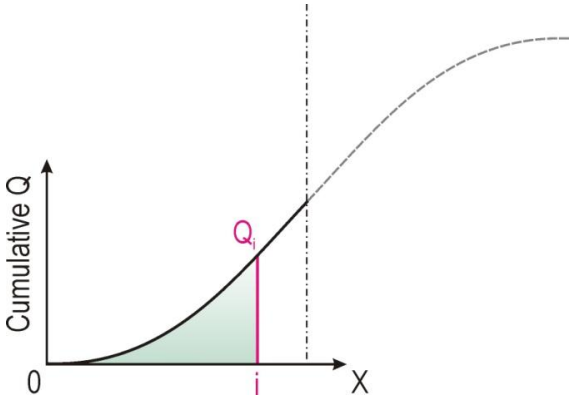

Figure 2.17: Cumulative discharge from the wall to the centerline

Equation 2.1 can be used to compute the average velocity between the outer culvert wall and position i:

$$(V_{AVG})_i = \frac{Q_i}{A_i} \qquad 2.1$$

For the flow condition illustrated in Figure 2.14, the cumulative discharge (Q), cumulative area (A), and the corresponding average velocity can be computed with MATLAB, as shown in Figure 2.18 through Figure 2.20.

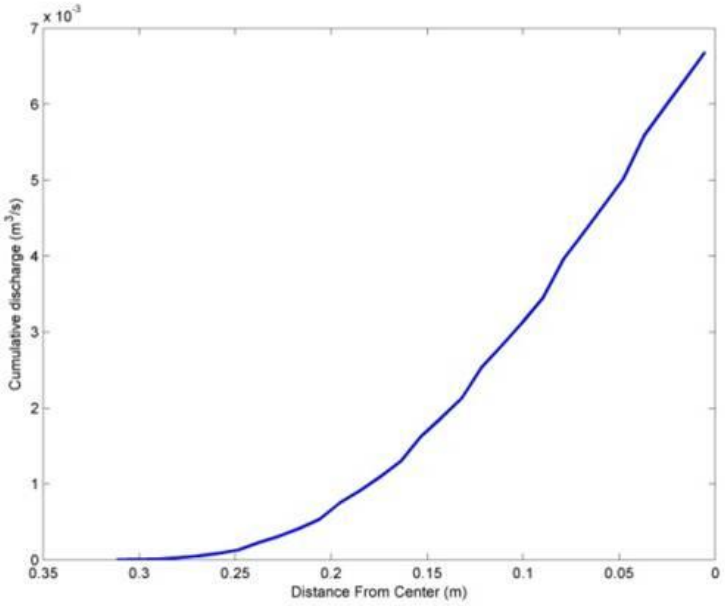

Figure 2.18: Cumulative discharge from the wall to the centerline in a cross-section of 6 inch water depth with symmetry boundary

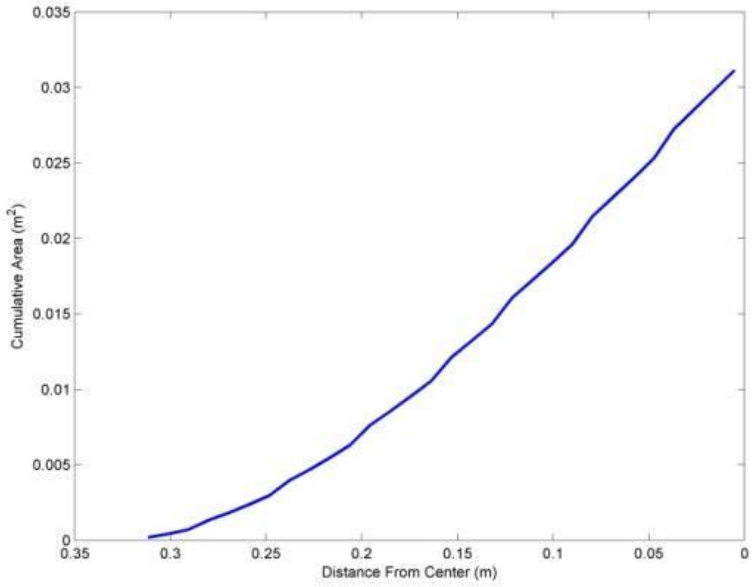

Figure 2.19: Cumulative area from the wall to the centerline in a cross-section of 6 inch water depth with symmetry boundary

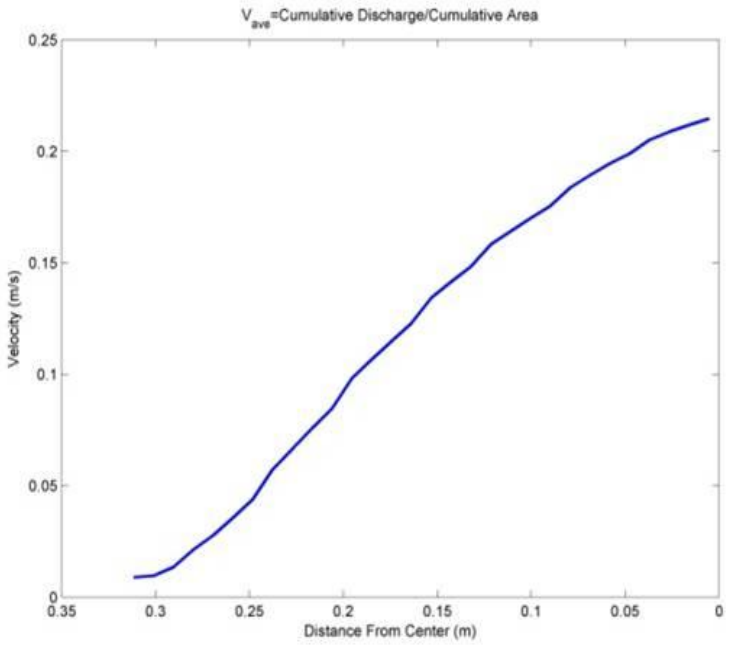

Figure 2.20: average velocity curve in a cross-section of 6 inch water depth with symmetry boundary

2.2.2. Porous Media Modeling

For the larger size gravel beds in culverts, the gravel bed cannot be modeled as a rough wall with wall functions used to determine the wall shear stress because the near wall cell height would be a significant fraction of the water depth, making the grid too coarse to obtain an accurate solution. Two alternatives to modeling the effects of the presence of a gravel bed are (1) to include the large scale roughness in the geometry and mesh the irregular surface of the bed, and (2) to model the bed as a porous media. Porous media models in CFD software usually treat the porous media part of the domain as a distributed volumetric flow resistance. Porous media models capture the overall effects of the presence of the porous region on a flow without resolving the small scale details of the flow in the interstitial spaces of the media. Modeling the effects of a large diameter gravel bed in a culvert on the main flow above the bed appears to be a good fit into the class of problems that can be handled with the porous media model.

Some difficulties arise as a consequence of using short sections of culvert with cyclic boundary conditions to determine the cross section velocity for fully developed flow conditions. When a porous media is present in the bed subdomain, the cyclic boundary conditions cannot be applied to the porous subdomain. This restriction means that a section of culvert modeled with cyclic boundary conditions and porous media for the bed is equivalent to having a gravel bed with plates blocking flow in the porous media between sections. The effect of this limitation is expected to be small. The work to set up the porous media models was completed, initial tests were run, and the results are presented in the following sections. A comparison of the previously used short section and a section five times as long, which allows for more induced flow in the porous media, was also done to see if there is a significant difference.

2.2.2.1. Porous Media Parameters

The TFHRC work plan for the culvert studies [6] has cases with large gravel sizes of 12 mm and 24 mm that will be modeled using a porous media subdomain. The parameters characterizing the porous media in the model are the porosity, permeability, and the beta factor coefficient of the Forchheimer inertial momentum sink term in the porous media momentum equation. In absence of experimental or other material property information for the gravel in the bed, the gravel is taken to be a packed bed of spheres with diameter equal the mean gravel diameter. The porosity of packed beds of spheres can vary depending on how densely they are packed. The porosity was taken to be 0.40. This value corresponds to a midrange packing that would be typical of poured random packing.

For packed beds, the STAR-CCM+ User Guide [7] gives the permeability, k_p, as:

$$\frac{1}{k_p} = \frac{150(1-\chi)^2}{\chi^3 {D_p}^2} \tag{2.2}$$

where D_p is the mean diameter of particles in the porous medium, and χ is the porosity, The inertial term beta factor is given as:

$$\beta = \frac{1.75(1-\chi)}{\chi^3 D_p} \tag{2.3}$$

The coefficients P_v and P_i, of the viscous and inertial momentum sink terms for packed beds in the STAR-CCM+ porous media model are user inputs that define the model parameters and they contain the viscosity, μ, and density, ρ, of the fluid (water):

$$P_v = \frac{150\mu(1-\chi)^2}{\chi^3 {D_p}^2} \tag{2.4}$$

And

$$P_i = \frac{1.75\rho(1-\chi)}{\chi^3 D_p} \tag{2.5}$$

2.2.2.2. Implementation of Porous Media in STAR-CCM+

CD-adapco's STAR-CCM+ software provides a mechanism by which field functions can be used to modify the physics models of the flow or define parameters in physics models. The specification of porous inertial resistance and porous viscous resistance along with the other input conditions and values are enabled for a porous region to specify the coefficients of flow resistance. These coefficients are used to calculate the porous media sink terms in the momentum equation, as detailed in the formulation.

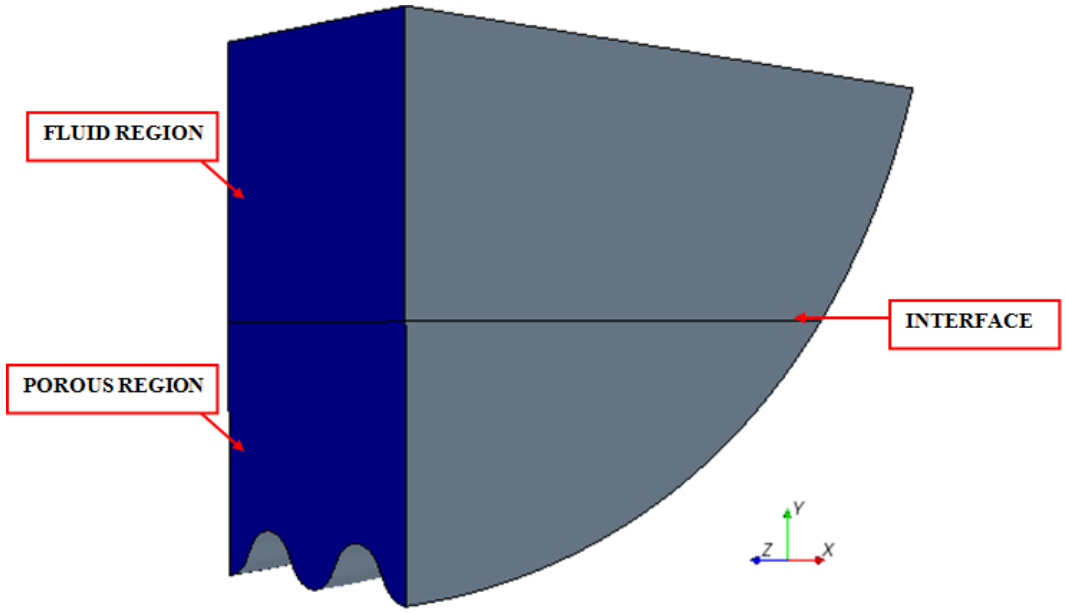

Figure 2.21 CAD model representing the computational domain used for porous media modeling

2.2.2.3. Description of the Physical Model

In this study, a simulation model was developed using the commercial CFD software STAR-CCM+. A small section of the culvert barrel was modeled with cyclic boundaries at the inlet and outlet sections of the computational domain in the fluid region as in the previous studies for flow through a culvert with no gravel. For simulating the flow within the porous region, the ends of the domain with the cyclic boundaries are treated as walls in the lower porous region because the cyclic boundary conditions cannot be applied when there are multiple types of inlet and outlet boundaries to be coupled. A 36 inch diameter culvert with corrugation size 3 inches by 1 inch has been used for this study. A flow depth of 6 and 9 inches for a flow velocity of 0.71 feet/second is considered for this study.

2.2.2.4. Boundary Conditions for the Porous and the Fluid Regions

The physical model consists of two regions namely the fluid region, which is the focus of the study and the porous region (gravel section) which is being simulated using the porous media approach. The following are the boundary conditions used for the fluid region.

Table 2.2 Boundary conditions

Boundary	Name	Type
Face at minimum value	Inlet	Cyclic boundary condition
Face at maximum x value	Outlet	Cyclic boundary condition
Water surface	Top	Symmetry plane
Centerline	Center	Symmetry plane
all other surfaces	Barrel	No-slip wall

For the porous region, the boundary at the centerline is taken to be a symmetry plane and all other surfaces are considered as no-slip wall. In Figure 2.21, the interface between the fluid and the porous region, which is taken to be an in-place boundary, is shown.

2.2.2.5. Meshing Methodology

A strategic meshing technique has been adopted to mesh the model to get good CFD results. It is very important to have an optimum number of cells in the mesh to have a good flow resolution. As a part of the meshing strategy, a volumetric control (annulus ring) has been created along the corrugated section. The mesh is refined along the volumetric control with respect to the other regions of the computational domain. The refinement of the mesh is defined by specifying a reduction of mesh size for volume within an annulus intersecting the model as shown in Figure 2.22. The volumetric control body intersecting the corrugated section provides a means to refine the mesh in the corrugated region of interest. The refined mesh enables better resolution of the flow field with recirculation zones at the troughs between the corrugations. Also a block has been created at the interface of the fluid and the porous regions where the mesh is further refined. The purpose of creating a block for mesh refinement is the same as that of creating an annulus ring around the corrugated section. Meshing also includes a prism layer consisting of orthogonal prismatic cells running parallel to the wall boundaries, which constitutes a boundary mesh that is good for the application of wall functions to compute the shear stress at the wall boundaries.

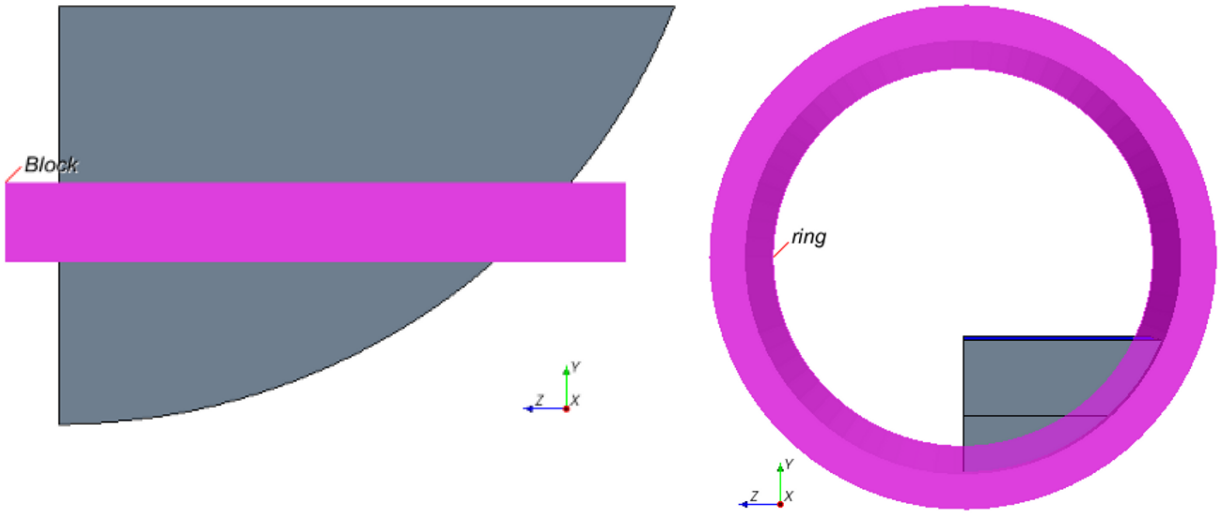

Figure 2.22 Volumetric controls created around regions of major interest for mesh refinement

From the mesh refinement studies, done to find the optimum base size of the mesh for a 36 inch diameter of the culvert with corrugation size 3 inches by 1, for a flow depth of 6 inches and 9 inches, it was found that a base size of 5 mm and 67 % refinement in the volumetric controls is a good size for the mesh which gives mesh independent simulation results with adequately fast run times. The same base size of the mesh and refinement along the volumetric controls has been used for the present study.

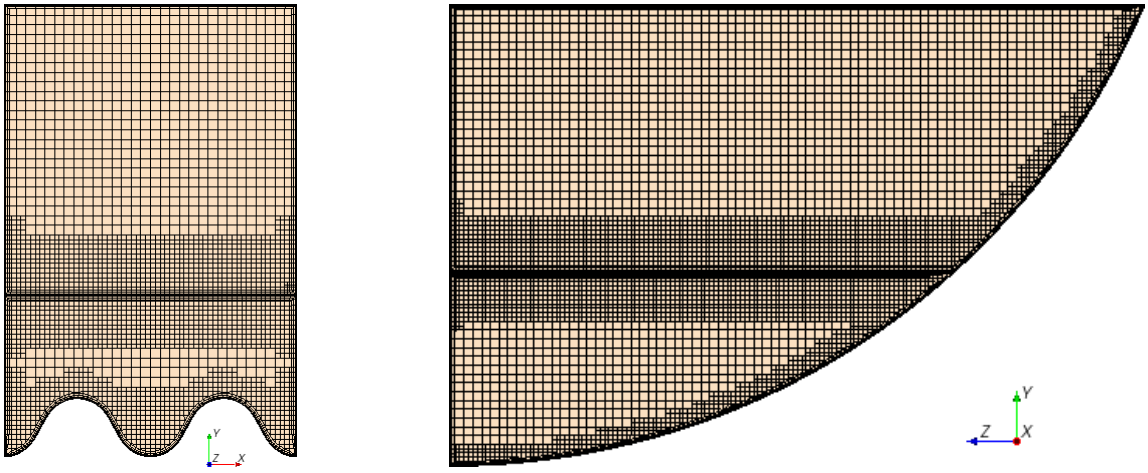

Figure 2.23 Cross sectional view of the mesh scenes

2.2.2.6. Comparison of the Reduced Section of a Culvert with an Increased Section

A reduced section with cyclic boundary conditions has been used for all CFD tests. Working with a reduced section is computationally fast, allowing a couple of tests to be completed in one day. In order to check the reliability of the results with blocking walls in the porous section at the cyclic boundaries of the culvert, a comparison study has been conducted to check for significant differences in both the fluid

and the porous regions when the modeled section length is significantly increased allowing more opportunity for induced flow to develop in the upper part of the porous media when compared to a reduced section of only two corrugation crests.

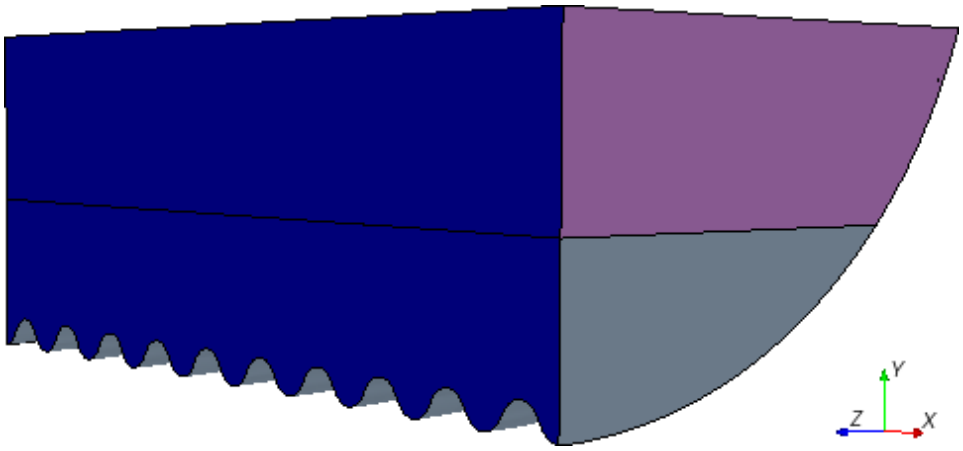

Figure 2.24 Increased section of the culvert (nearly five times bigger than the reduced section) used for porous media modeling

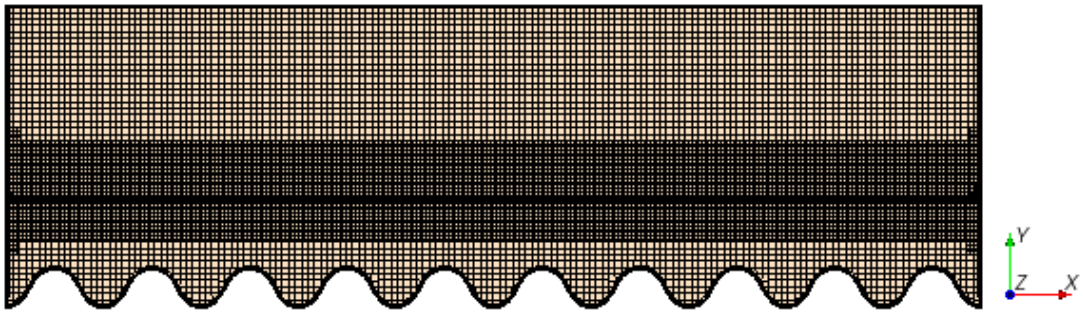

Figure 2.25 Cross sectional view of mesh scene along on a plane taken along the length of the increased section

For this comparison study, an increased section has been created. The increased section is 5 times longer than the reduced section. The CFD run corresponding to the increased section has the same mesh and flow parameters as that of the reduced section. After mesh generation, it was found that the volume mesh for the reduced section contains about 554176 cells and the volume mesh for the increased section contains about 2468562 cells. The results of each of these tests are presented in the following sections.

2.2.2.7. Results and Discussion

Line probes have been created along the flow section in the STAR-CCM+ software. In this particular case line probes have been created at a trough and a crest which are the regions of major interest. Each of the line probes created has 30 points on the line. The value of the velocity magnitude of the flow is extracted at each particular point. Velocity profiles have been plotted using the line probes at a trough

and a crest for both the reduced barrel and the increased sections. By taking a close look at the velocity profiles, it is possible to better analyze the nature of the flow.

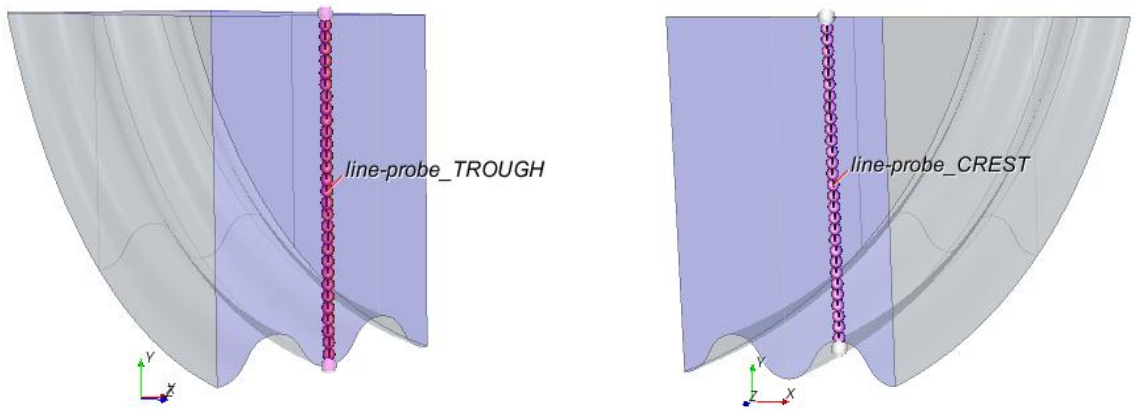

Figure 2.26 Image depicting the line probes created at a trough and a crest for a reduced section

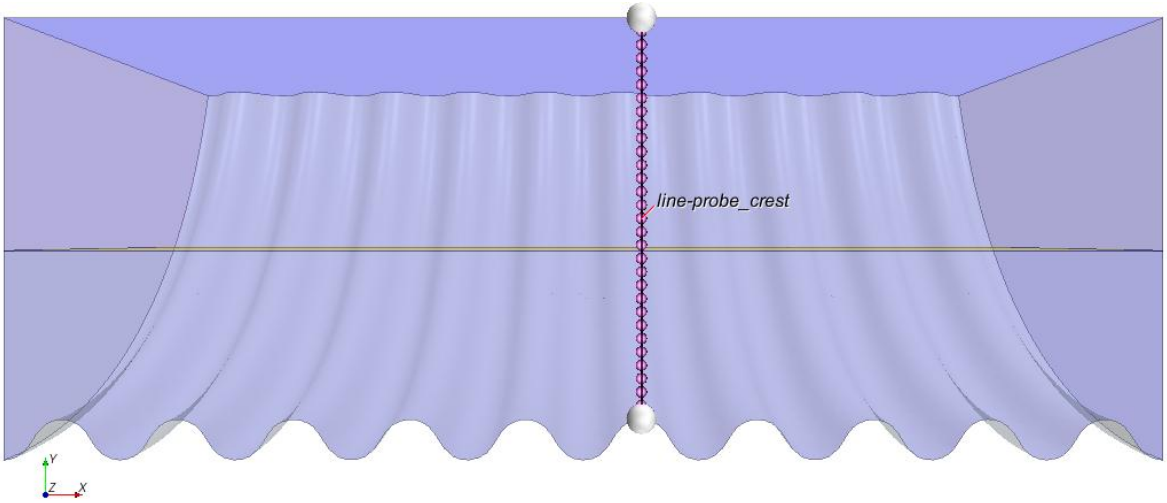

Figure 2.27 Image depicting the line probe created at a crest for an increased section

In Figure 2.28, the x-axis of the plot represents velocity and the y-axis represents the position of the line probe at a trough in the vertical direction. The minimum unit on the y-axis is 0.15 m and the maximum unit is 0.45 m. The y coordinate of the boundary representing the water surface (namely the top of the reduced culvert section in the CFD study) is at 0.17 m and the y coordinate of the boundary representing the bottom of the culvert at the wall is at 0.4572 m. The same CAD model has been used for all the CFD simulations with the co-ordinates of the reduced symmetric barrel section considered from a trough to a trough as mentioned above. The top surface of the culvert is simulated as a symmetry plane as mentioned previously which represents an imaginary plane of symmetry in the simulation. It implicates an infinitely spread region modeled as if in its entirety. The bottom of the culvert is simulated as a wall with a no slip condition. When velocity is plotted against position, the velocity at the wall is zero, the first point plotted is the velocity in the cell next to the wall and increases with distance from the wall.

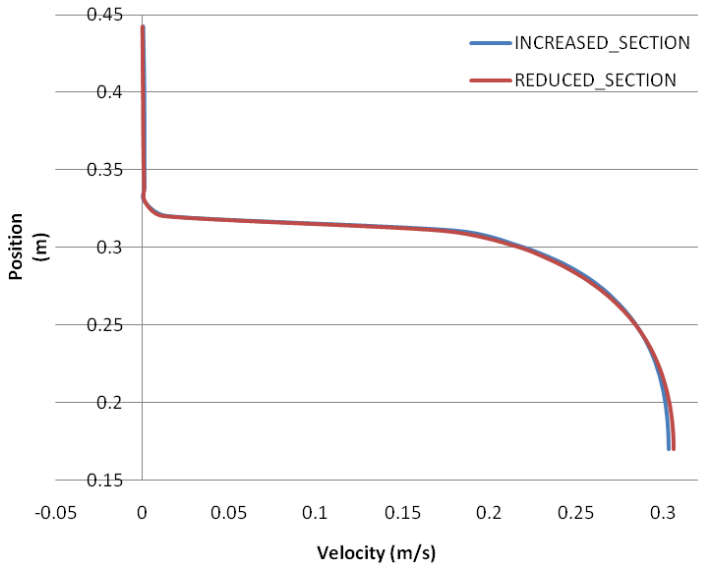

Figure 2.28 Velocity profiles for both reduced and increased sections at a crest

In Figure 2.28, the velocity and the position corresponding to the line probe at a crest are plotted on the x and y axis respectively. Figure 2.29 shows a similar comparison at a trough. The velocity in the porous region is very close to zero. The velocity profile in the fluid region is close to that of one with a wall boundary. The profiles for reduced and long barrel sections are nearly identical, and therefore the shorter section appears to be reasonable to use for determining the cross section velocity distribution above the porous media in parametric tests for different conditions and culvert geometry parameters with a gravel bed.

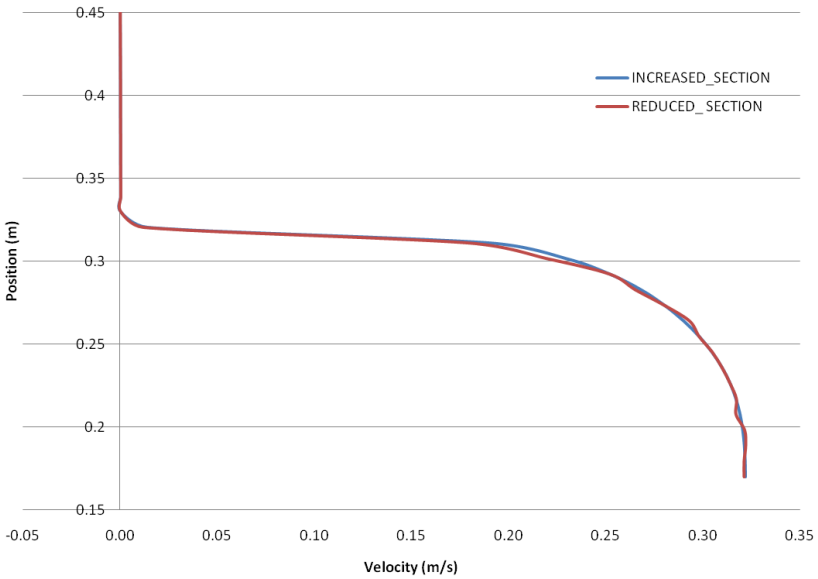

Figure 2.29 Velocity profiles for both reduced and increased sections at a trough

Uniform strips were created on the plane section at a crest in the test case. Figure 2.31 shows the odd numbered strips created on the plane section at a crest in the fluid region. This procedure is carried out

by creating multiple “Thresholds” of 1 cm width along the plane section that align with grid cell faces. They are aligned with cell faces to avoid interpolation error and obtain the mean strip averaged velocity based on cell centroid values. After the thresholds are created, there is a “Report” feature available in STAR-CCM+ which calculates the surface averaged velocity over a vertical strip object.

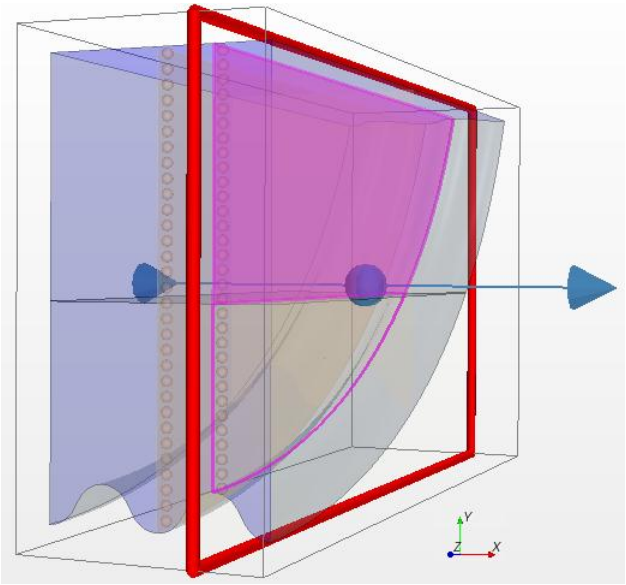

Figure 2.30 Cross sectional plane created at a crest in the porous region for a reduced section

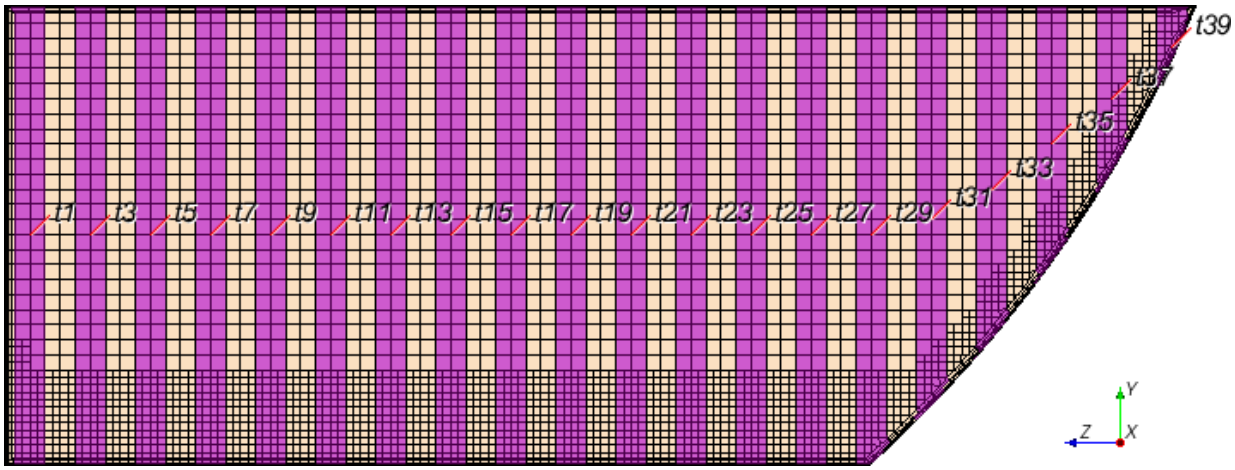

Figure 2.31 Representation of odd numbered Uniform strips of 1 cm width created along the fluid section

In Figure 2.32 a plot of surface-averaged velocities of the strips on the plane section at a crest is plotted across the width of a cross section, where the centerline is at zero. The y axis of the plot indicates the position of a strip and the x axis of the plot indicates the strip-averaged velocity.

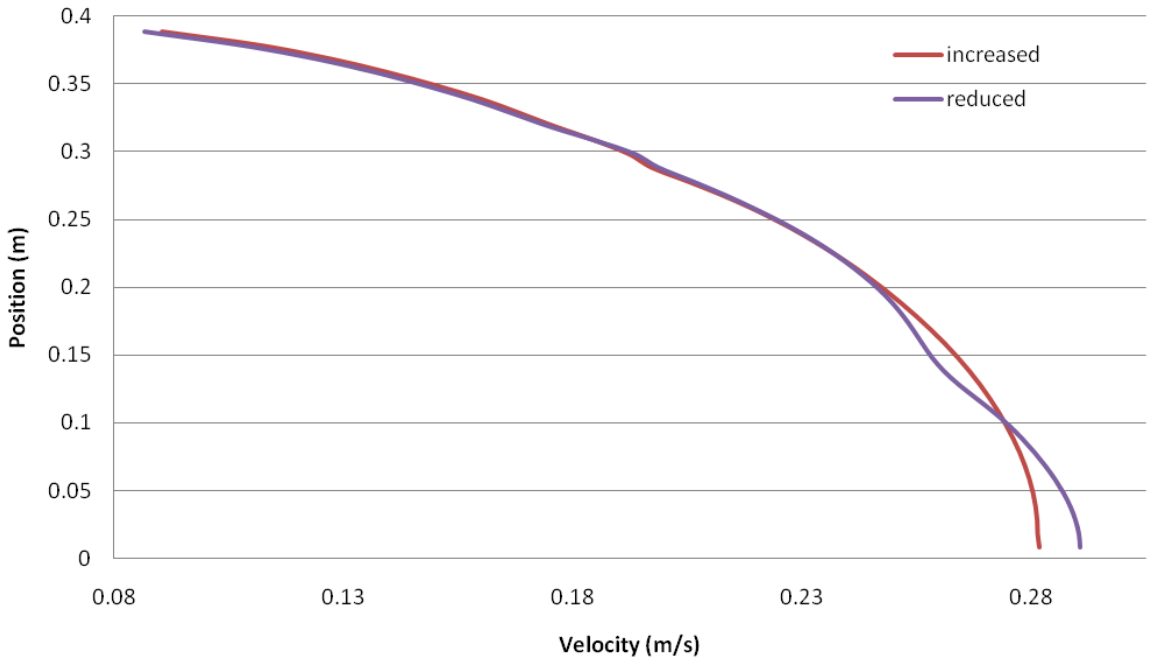

Figure 2.32 Surface-averaged velocity variation along the uniform strips plotted using " Thresholds"

The origin on the y-axis corresponds to the centerline of the barrel section and the maximum point on the y-axis corresponds to the corrugated wall. It can be seen that for both the increased and reduced section the maximum velocities differ only slightly. The percentage difference in the results for the increased section and the reduced section is small, 3.7% and considered to be adequate for engineering analysis.

Figure 2.33 shows the velocity distribution over the culvert cross section with a porous media gravel bed with velocity near zero. The effect of the porous bed on the flow above is as expected: it acts as a wall-like flow resistance bringing the velocity down near zero at the interface between the free flow region and the porous media. There is a small amount of waviness in the contours approximately midway between the centerline and the outer culver wall that may merit some further investigation. A possible fish passage zone pattern is apparent as a lower velocity yellow region away from the centerline.

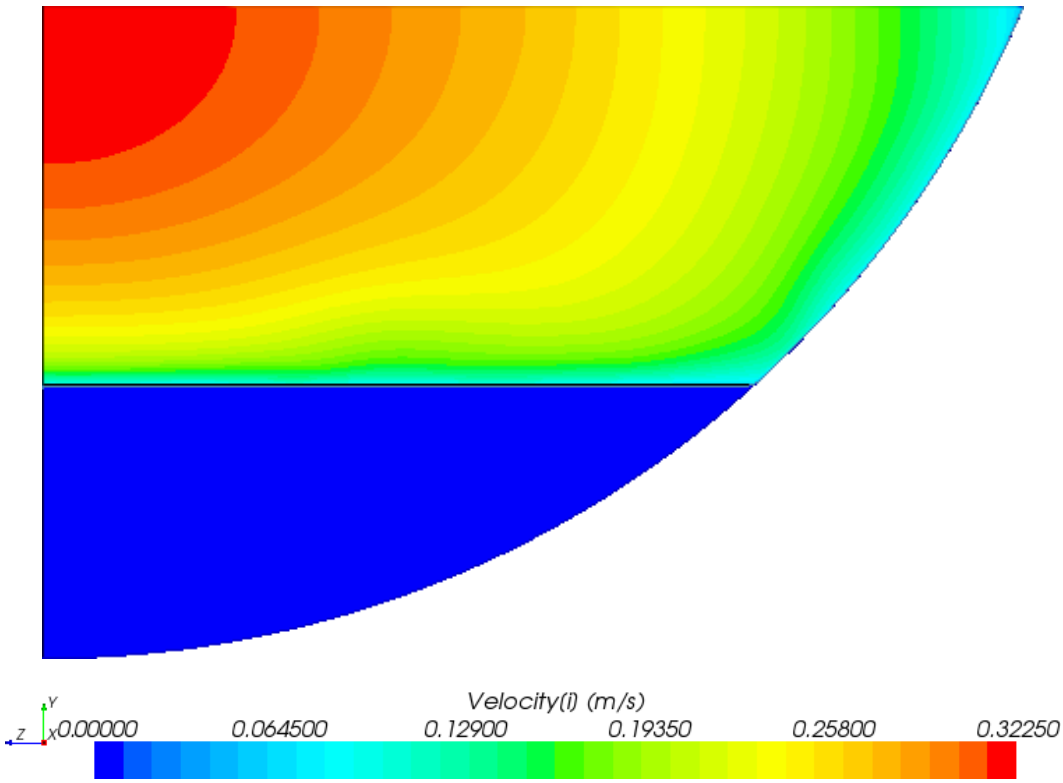

Figure 2.33: Velocity distribution over cross section at a crest showing the variation above the porous media gravel bed

2.2.3. References

1. Matt Blank, Joel Cahoon, Tom McMahon, "Advanced studies of fish passage through culverts: 1-D and 3-D hydraulic modeling of velocity, fish expenditure and a new barrier assesment method," Department of Civil Engineering and Ecology, Montana State University, October, 2008 .
2. Marian Muste, Hao-Che Ho, Daniel Mehl,"Insights into the origin & characteristic of the sedimentation process at multi barrel culverts in Iowa", Final Report, IHRB, TR-596, June, 2010.
3. Liaqat A. Khan, Elizabeth W.Roy, and Mizan Rashid, "CFD modelling of Forebay hydrodyamics created by a floating juvenile fish collection facility at the upper bank river dam", Washington, 2008.
4. Angela Gardner, "Fish Passage Through Road Culverts" MS Thesis, North Carolina State University, 2006.
5. Vishnu Vardhan Reddy Pati, "CFD modeling and analysis of flow through culverts", MS Thesis, Northern Illinois University, 2010.
6. Kornel Kerenyi, "Final Draft, Fish Passage in Large Culverts with Low Flow Proposed Tests" unpublished TFHRC experimental and CFD analysis of culvert flow for fish passage work plan, 2011.

7. CD-adapco, *User Guide STAR-CCM+ Version 6.04.014*, 2011

2.2.3.1. Initial Modeling of the Wind Tunnel Laboratory at TFHRC

2.2.4. Model Development

A study of the TFHRC wind tunnel CFD modeling was initiated in this quarter. It aims to provide TFHRC researchers with the answers to the following questions:

- What is the overall quality of the flow in the testing section of the tunnel?
- What is the influence of the room walls' proximity on the air flow in the room?
- What is the influence of the room setup (including layout of the furniture and the equipment) on the flow quality?

A CAD data file containing the detailed geometry of the wind tunnel was initially provided by TFHRC (see Figure 2.34). It was importable to STAR-CCM+, although the geometry of the fan and fan inlets were overly simplified and required modifications.

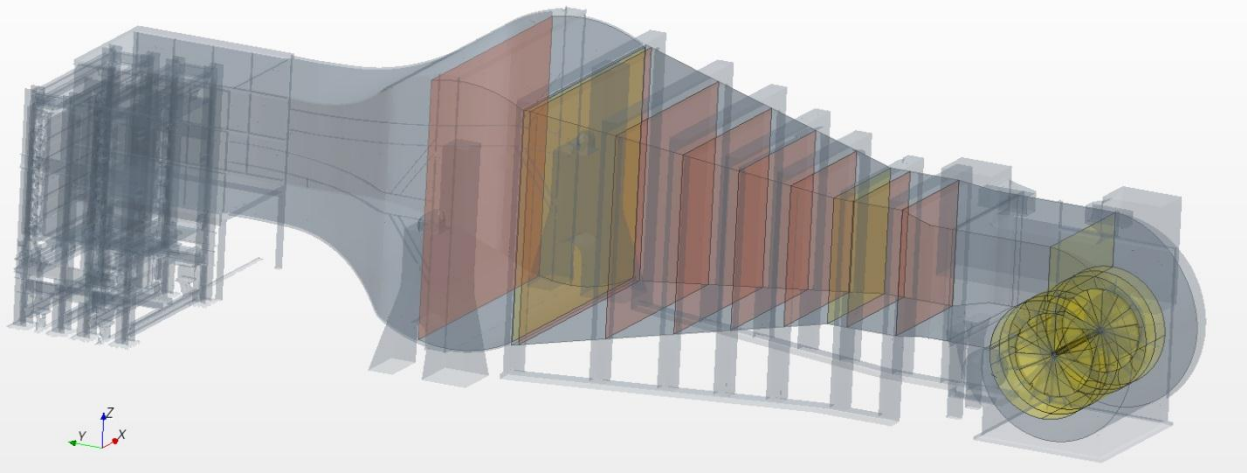

Figure 2.34: CAD model imported to STAR-CCM+

Figure 2.35 and Figure 2.36 show changes that were made to these parts of the model. Although the fan inlets closely resemble the real shape now, the fan is still simplified and in future may need additional improvements. Nevertheless, for the purpose of this study, it is believed that the actual geometry of the fan and inlets should provide reasonably good results for engineering assessment of the effects of room wall and furniture on wind tunnel air flow.

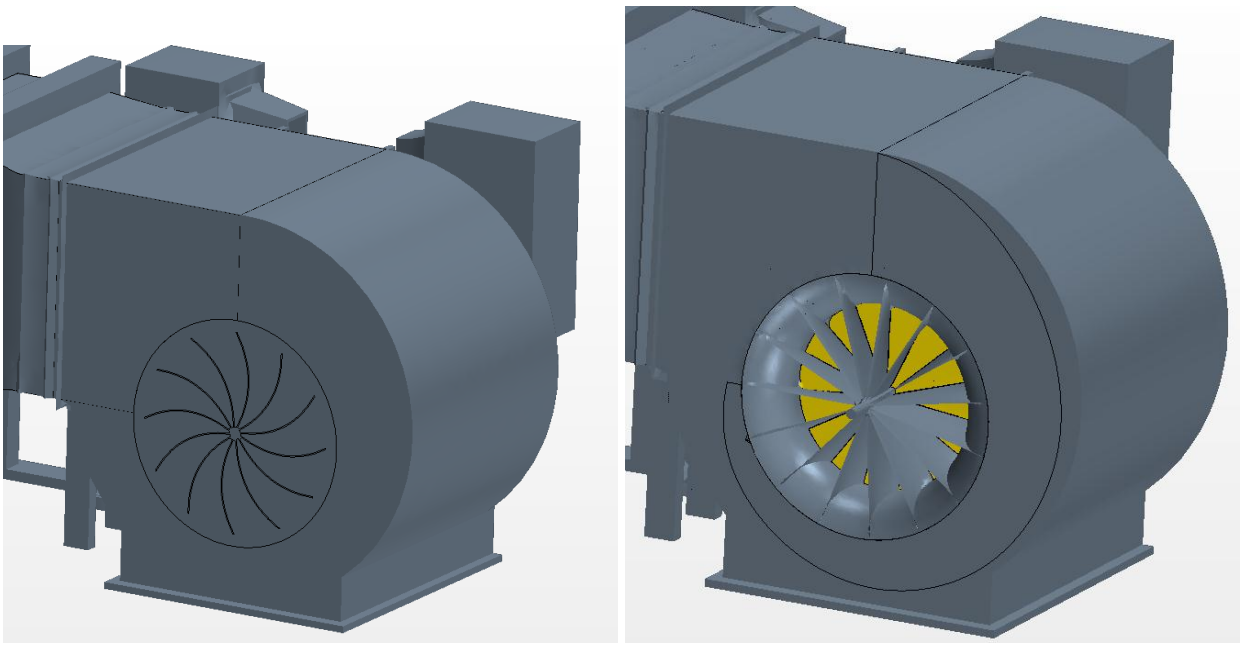

Figure 2.35: Geometry of the fan inlets: initial (left) and updated (right)

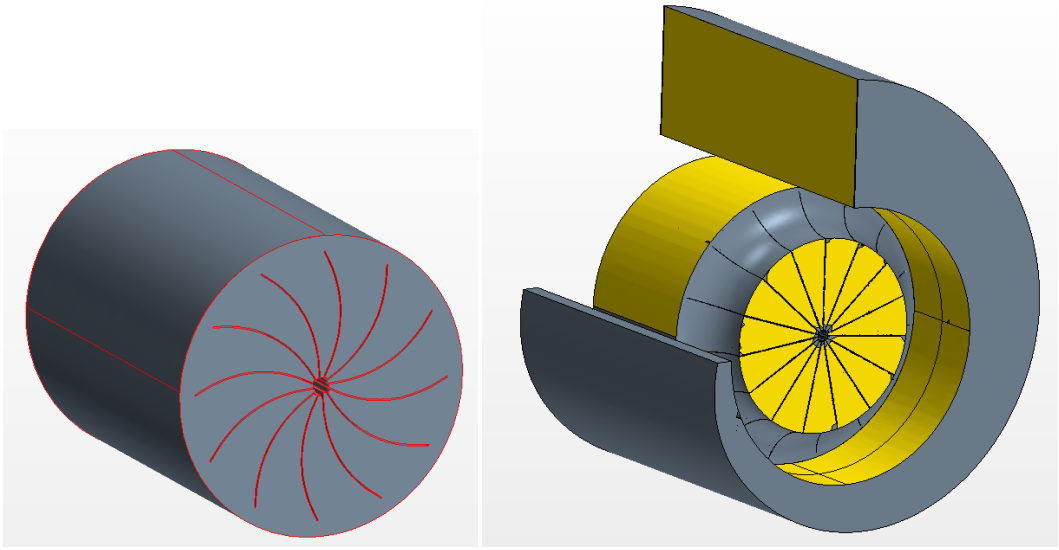

Figure 2.36: Geometry of the fan: initial (left) and updated (right)

The geometry was divided into several regions that have separate meshing settings. Nine regions for the tunnel, two regions for the fan assembly and one for the rest of the model were created. The densest mesh was defined in the fan region due to its geometrical complexity. A fine mesh was needed in order for the surface wrapper to fill the volume entirely. The entire model contained almost 3,500,000 cells. Several cross sections through it showing the mesh are shown in Figure 2.37.

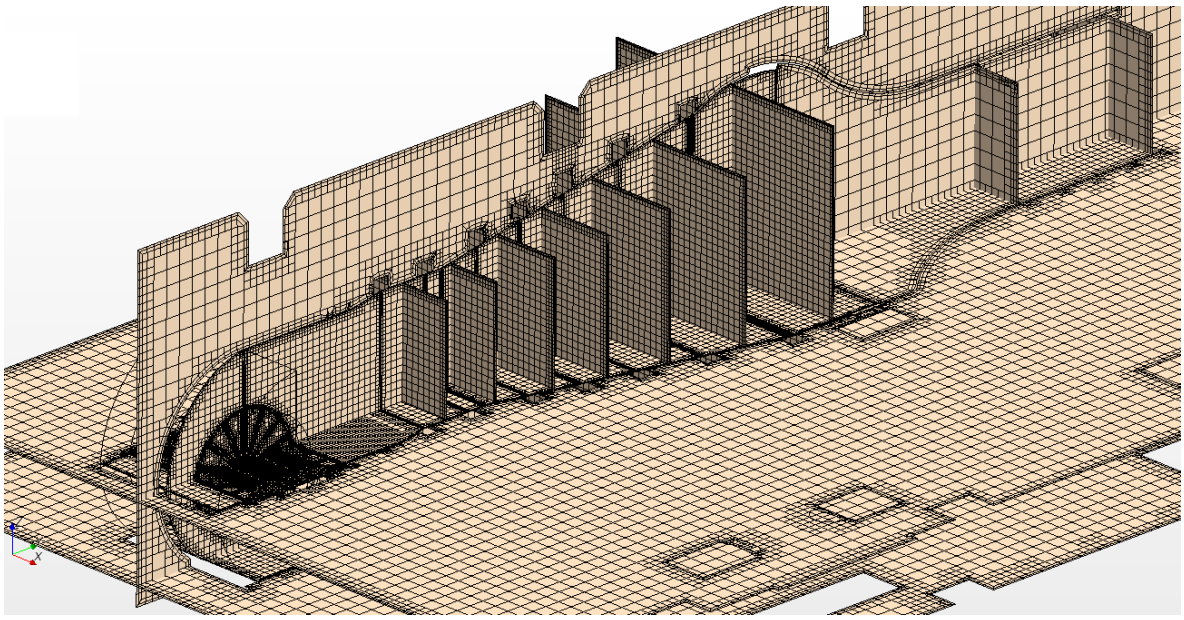

Figure 2.37: cross sections through the model

The interaction between the regions in the model was further defined by interfaces. The interfaces are highlighted in Figure 2.34 by yellow and orange colors. The yellow ones represent continuous in-place interfaces that do not cause any losses in the flow pressure while the orange ones represent porous baffles. The porous baffles were defined at the locations where screens are installed in the real tunnel. The porosity of the screens was determined to be 0.672 based on the specification sheets provided by TFHRC [1]. According to the STAR-CCM+ user guide [2] the pressure drop across a porous baffle can be modeled with the following equation:

$$\Delta p = -\rho(\alpha|v_n| + \beta)v_n \tag{2.6}$$

Where ρ is the density of air and v_n is the normal velocity of air acting on the screen and α and β are parameters that depend on screen geometry and properties.

In [3], this relation is reduced to only the quadratic term with parameter K:

$$\Delta p = -\frac{1}{2}K\rho {v_n}^2 \tag{2.7}$$

Setting parameter β to zero in Equation **2.6** we can now relate α to the K parameter as:

$$K = 2\alpha \tag{2.8}$$

The simplest Borda-Carnot one-dimensional formula for screen pressure-drop coefficient defines K as follows [4]:

$$K = \frac{1-\chi}{\chi^2} \tag{2.9}$$

Where χ is the open area ratio (χ = 0.672).

As a first approximation parameters for the porous baffle were assumed constant for each screen as: α = 0.3632 and β = 0. However, it should be noted that this formula may overestimate K for high Re numbers [4]. A more advanced formula by Weighardt defines *K* as [4]:

$$K = 6.5\left[\frac{1-\chi}{\chi^2}\right]\left[\frac{v_n d}{\chi \nu}\right]^{-0.33} \quad 2.10$$

Where v_n is the air velocity normal to the screens, d is the screen wire diameter and ν is the kinematic viscosity of the air.

Taking the diameter of the screen wire as 0.0075 inch, the kinematic viscosity of air as 15.68e-6 m/s^2 and its constant velocity on all screens to be 20 m/s, this formula yields definition:

$$K = 0.91\frac{1-\chi}{\chi^2} \quad 2.11$$

This simple calculation shows that the constant K may be substantially overestimated depending on the velocity of the air on the screen. Now that the approximate velocities of the air on the screens are known, a second iteration can be conducted with more accurate values for K calculated from Equation 2.10.

Another important feature of the model was the rotating fan. To introduce the rotation effect on the flow, a rotating reference system was defined with one axis going through the axis of the fan. A constant velocity of 500 rotations per minute was assigned to the system and the fan. This is the operating speed of the fan as per TFHRC specifications.

2.2.5. Results

2.2.5.1. The model without the furniture

The first set of simulations model the system without the furniture in the room to determine the characteristics of the flow field in an empty room as a base case. Figure 2.38 shows velocity profiles in the room and the tunnel at a vertical plane through the center of the tunnel. Note that the velocity in the extension of the tunnel and the testing section (just in the front of the tunnel) appears quite uniform. In a horizontal plane about mid-height through the tunnel the flow in the room is asymmetrical (see Figure 2.39). The left side (looking downstream) is blocked by the turbulence generator. In the original model the vanes in the generator were in a closed position. The mass flow through the fan inlet on the left side was 18.713 kg/s (15.54 m^3/s) and 17.058 kg/s (14.17 m^3/s) on the right side. The right side inlet is obstructed with a pulley plate for turning the fan.

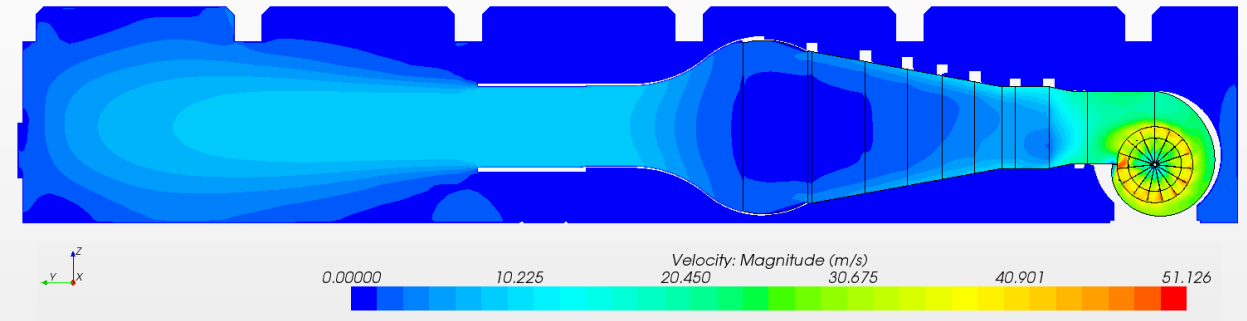

Figure 2.38: Velocity profile in model without the furniture – vertical plane

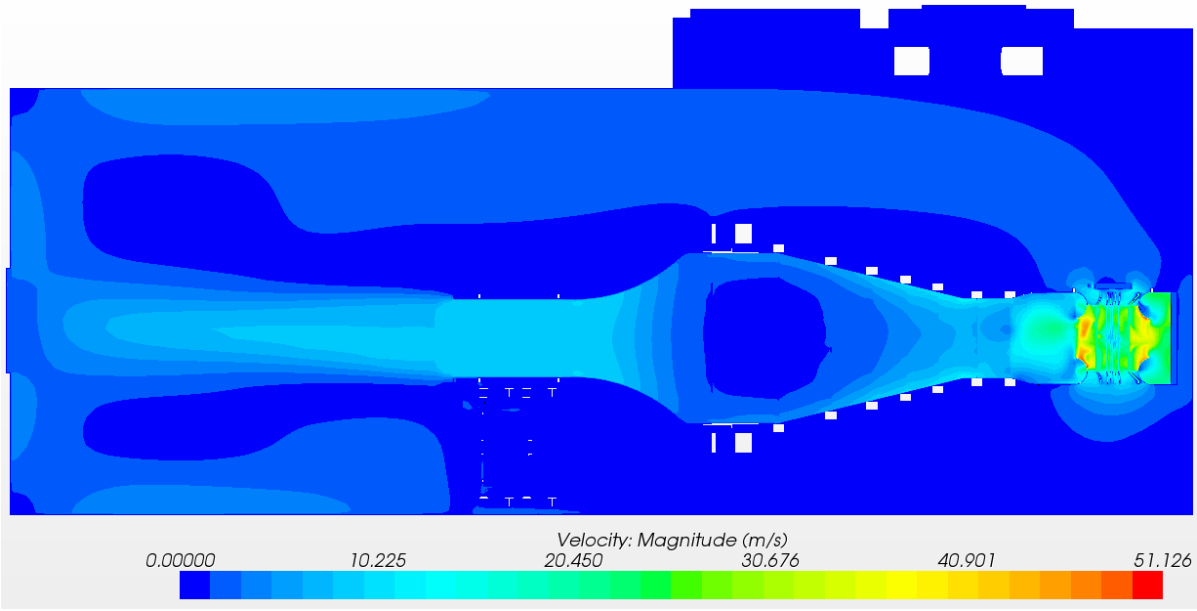

Figure 2.39: Velocity profile in model without the furniture – horizontal plane

Figure 2.40 presents the pressure profile in the wind tunnel. Significant drops of pressure are noted as expected across the screens.

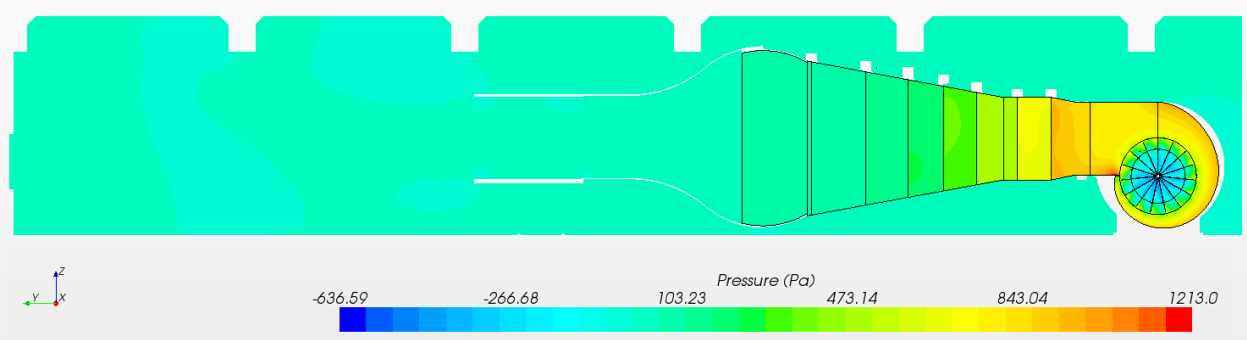

Figure 2.40: Pressure profile in the wind tunnel

To check how the turbulence generator is influencing the flow, the vanes in it were rotated to their neutral position. The generator itself was not moved from its initial position on the left side of the extension part of the tunnel. In this model the mass flow has changed only slightly: from 17.058 kg/s (14.17 m^3/s) to 16.63 kg/s (14.04 m^3/s) on the side blocked with the fan pulley plate and from 18.713 kg/s (15.54 m^3/s) to 19.25 kg/s (16.25 m^3/s) on the open (left) side.

2.2.5.2. The model without the furniture with removed screens in the tunnel

In the initial simulations the velocity of the air was higher in the tunnel in the near downstream of the fan near the boundaries of the tunnel. This appears to be counterintuitive at first and additional simulation was performed where the screens – porous baffles – were replaced with the in-place interfaces to eliminate them as the cause of the flow distribution. With no porous baffles, there is no pressure drop across the interfaces at the tunnel sections in the model. This simplified model was supposed to provide more insight into the flow and help identify if any potential errors were produced by the definitions of the porous baffles. Figure 2.41 and Figure 2.42 show the velocity profile obtained from the simulation with this simplified model. Note that for this case the velocity is still highest on the top of the tunnel. This behavior is attributable to the rotating elements of the fan releasing the air at tangent to the fan's circumference. On the bottom wall of the tunnel the velocity is also high since the air coming off the fan blades is meeting an obstacle. The flow inside of the tunnel and in the testing section is highly non-uniform. This shows the need for the screens inside of the tunnel to produce a near uniform flow in the downstream.

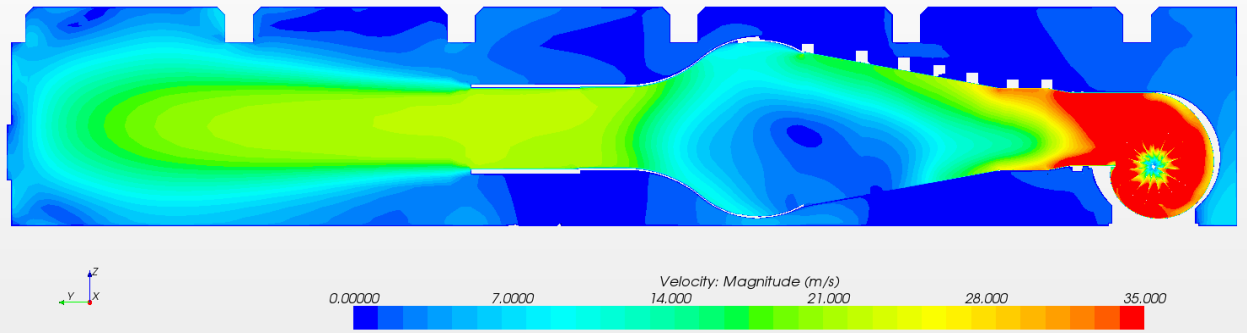

Figure 2.41: Velocity profile in model without the furniture and no screens – vertical plane

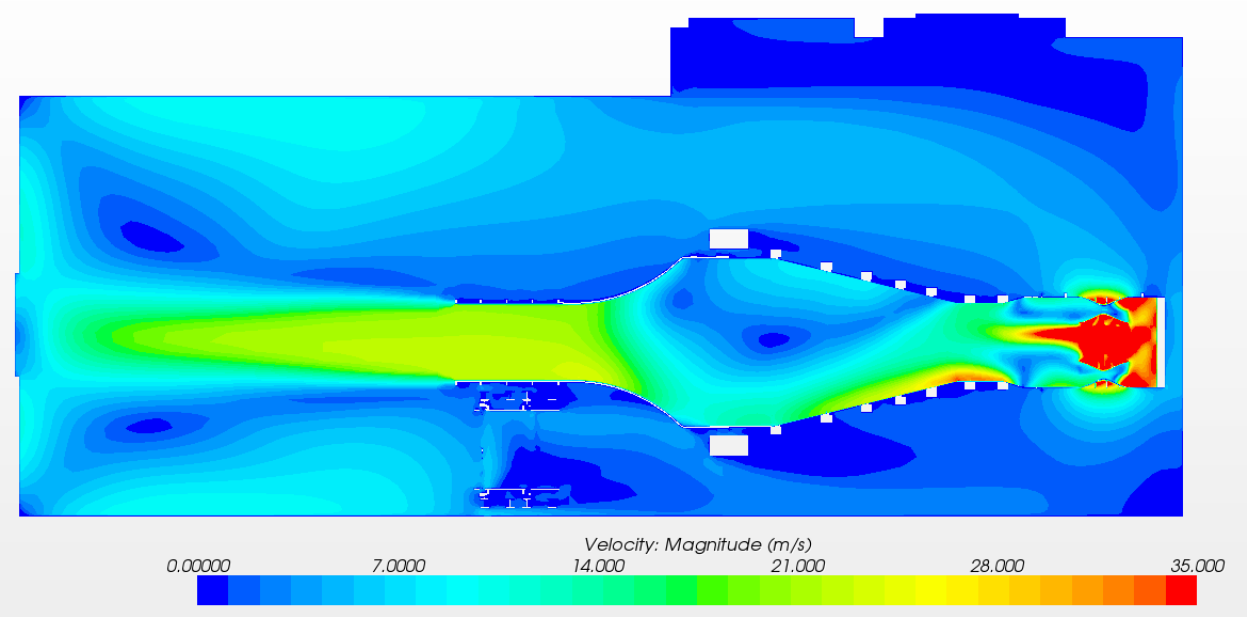

Figure 2.42: Velocity profile in model without the furniture and no screens – horizontal plane

The lack of the screens contributed significantly to the increase of the air mass flow through the fan inlets. The mass flow rate increased to 39.06 kg/s (32.98 m^3/s) and to 47.32 kg/s (39.96 m^3/s) on the right and left sides respectively.

2.2.5.3. The model without the furniture with extended boundaries

The next test conducted on the model was with a symmetric room where the walls were moved away from the tunnel, 10 meters each. Also the roof was raised 5 meters. Additionally the turbulence generator was removed from the model. This test was conducted to see how "ideal" conditions would change the flow pattern. Figure 2.43 shows the horizontal cross section through the model. The velocity profile is more symmetric than in the previous cases. The dark blue spans a velocity range between 0 and a little less than 2 m/s, causing the return flow not to show up in the plot because it is less than 2 m/s.

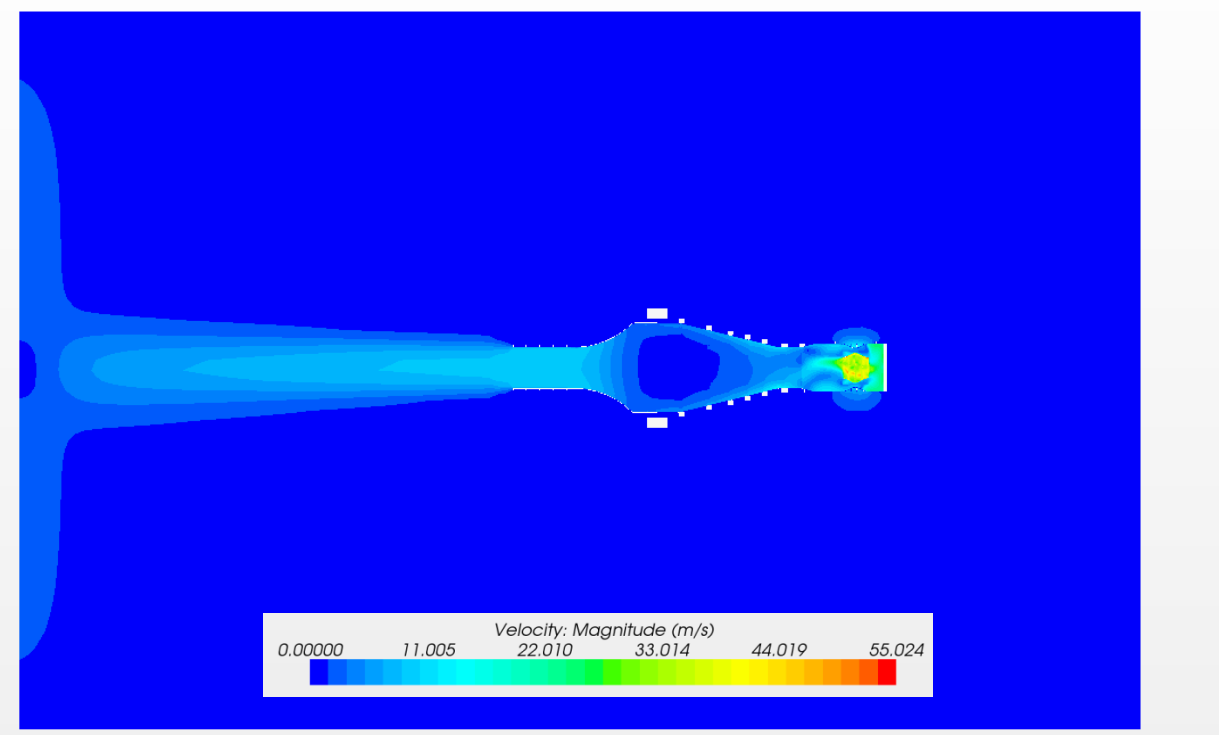

Figure 2.43: Velocity profile in model extended boundaries – horizontal plane

Surprisingly the air mass flow through the fan inlets didn't change much in comparison to the initial models. It has changed from 17.058 kg/s (14.17 m^3/s) to 16.70 kg/s (14.10 m^3/s) on the side blocked with the fan pulley plate (right side) and from 18.713 kg/s (15.54 m^3/s) to 18.87 kg/s (15.94 m^3/s) on the left side.

2.2.5.4. Comparison of the flow characteristics

In order to quantify the changes in the flow through the tunnel area, a standard deviation and coefficient of variation of the velocity at nine cross sections in the tunnel were calculated. The location of nine cross sections of interest is shown in Figure 2.44. Seven of them were located between the screens and additional two in the tunnel extension.

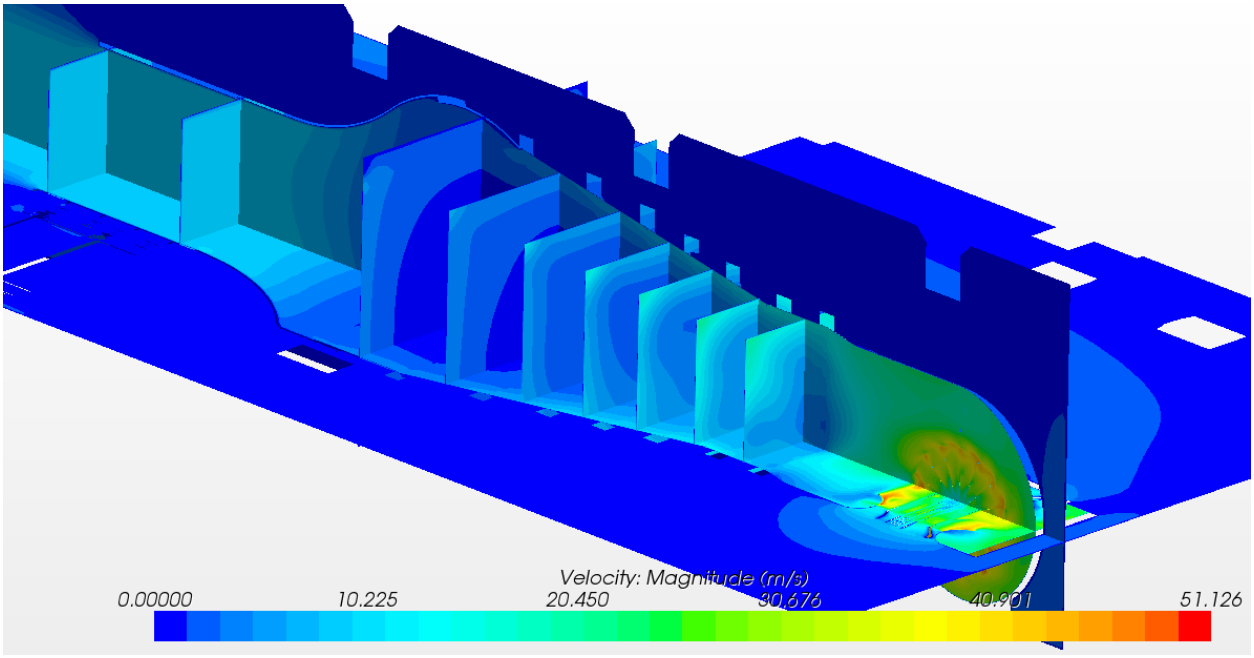

Figure 2.44: Sections of interest in the tunnel

Area averaged standard deviation of the velocity for three models:

- initial, without the furniture, with the turbulence generator vanes closed
- initial, without the furniture, with the turbulence generator vanes in neutral position
- without the furniture with extended boundaries, without the turbulence generator

are plotted in Figure 2.45. It can be noted that a slight difference between the curves can only be noticed at the first two screens. The standard deviation does not take into account the fact that the mean velocity is dropping once we go through the screens and for that reason the coefficient of variation of the velocity was also calculated. In both cases the screens smear out nearly all the non-uniformities of the velocity profile in the tunnel, reducing the measure of variation by about an order of magnitude.

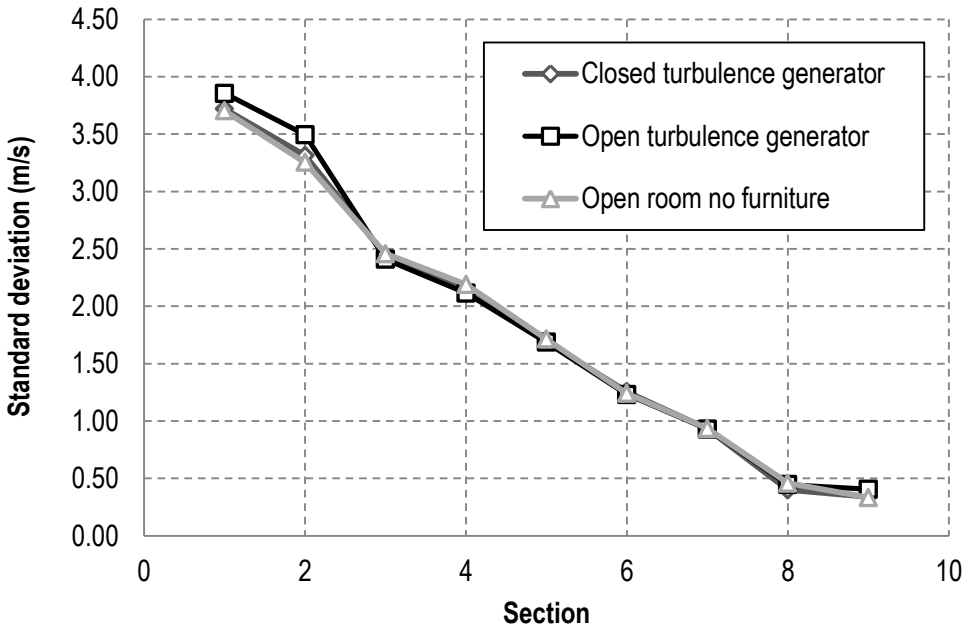

Figure 2.45: Area averaged standard deviation of the air velocity in the tunnel

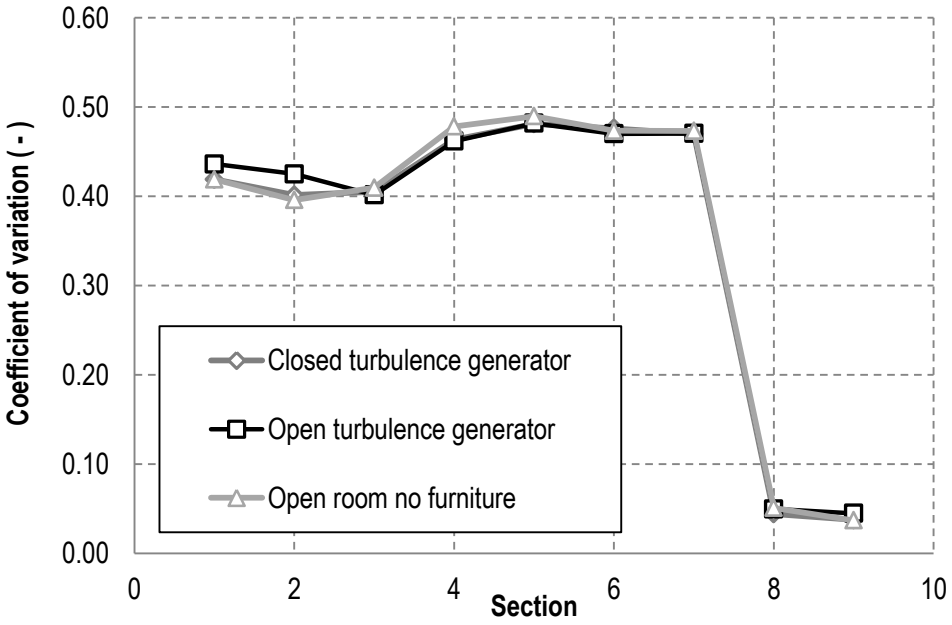

Figure 2.46: Area averaged coefficient of variation of the air velocity in the tunnel

Table 2.3 lists the mass flow rate calculated for the same three models. Again it can be noticed that despite the fact of considerable change in the model – translation of all the walls and removal of the turbulence generator, the amount of the air going through the inlets is not changing significantly.

Table 2.3: Mass flow rate through the fan inlets

Model	Left side	Right side
Closed turbulence generator	18.713 kg/s (15.54 m^3/s)	17.058 kg/s (14.17 m^3/s)
Open turbulence generator	19.250 kg/s (16.25 m^3/s)	16.630 kg/s (14.04 m^3/s)
Open room	18.870 kg/s (15.94 m^3/s)	16.700 kg/s (14.10 m^3/s)

To summarize, the flow through the tunnel appears to be insensitive to the changes in the room geometry that were tested in the current quarter. Yet additional runs for the cases with fully furnished room need to be performed to check the magnitude of the effect of current room furniture on the air flow uniformity. Note that the detailed model of the fan would also influence the results. However, the big picture is expected to remain largely unchanged with minor changes to the fan model geometry.

2.2.6. References

[1] McMaster-Carr, http://www.mcmaster.com/#wire-mesh/=emqkhc

[2] CD-adapco, *User Guide STAR-CCM+ Version 6.02.008*, 2011

[3] R.D. Mehta, *Turbulent Boundary Layer Perturbed by a Screen*, AIAA Journal, Vol. 2, No. 9, pp 1335-1342, September 1985

[4] R.D. Mehta, P. Bradshaw, *Design rules for small low speed wind tunnels*, The Aeronautical Journal of the Royal Aeronautical Society, November 1979

2.3. Modeling of Truck Generated Salt Spray under Bridge with Sliding Mesh

2.3.1. Model development

2.3.1.1. Geometry

In the recent quarter, a CFD approach to the modeling of truck generated salt spray was initiated. The technique of using a sliding mesh was employed to introduce movement of the vehicle. Domains with the truck and the bridge were separately built and meshed. A denser mesh with base size for an edge of 0.1 m was defined for the area surrounding the truck and the bridge beams. The rest of the domain was meshed with the base size of an element equal to 0.5 m. The geometry of the Raleigh - Tamarack Overpass (Bridge No. 4172) was used in the CFD analysis. The model of a truck tractor was based on the Mack CH 613 tractor. The sleeper and the dry freight van type trailer were modeled previously for the LS-DYNA analysis. The biggest allowed - 16.16 m long and 2.89 m wide - trailer was modeled.

From the previous analysis in LS-DYNA it was learned that a large volume behind the truck needs to be modeled in order to capture important behavior of the air behind the truck. For that reason, an air domain of 170 m x 42.8 m x 7.6 m was modeled in the CFD study. The meshing settings and extent of the model resulted in an overall computational cell count of 3,600,000. Figure 2.47 shows the geometry of the model at an intermediate stage of the analysis.

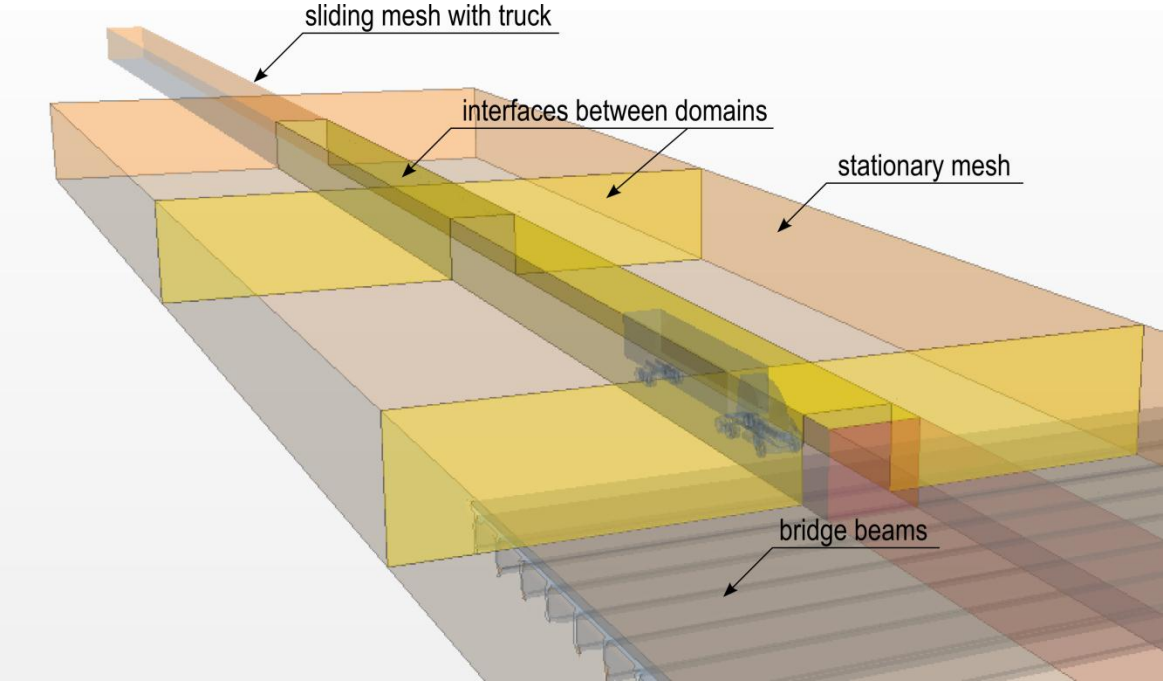

Figure 2.47: Geometry of the STAR-CCM+ model for analysis of truck generated salt spray

Initially the box with the truck was placed about 61.5 m in the front of the bridge. That distance was assumed to be enough for the flow around the vehicle to fully develop. Openings in the air domain with exact size of the truck box were created. The sliding mesh with the vehicle perfectly fills that volume once the vehicle is set in motion. In implicit unsteady analysis a time step of 0.02 sec was used. The

number of inner iterations of the solver was set to 20 to converge each time step. Motion of the box with the vehicle was prescribed in the forward – X direction with a velocity of 26.8 m/s (60 mph). In each time step interfaces between the adjacent domains are recreated and flow between them is allowed.

2.3.1.2. Spray generation

Lagrangian particles were used in the model to represent the liquid particles released from the truck tires. STAR-CCM+ has built in several types of particle injectors that can be attached to the boundaries of the geometry:

- Part injector,
- Point injector,
- Cone injector (particles with mass only),
- Surface injector, and
- Pressure swirl injector.

While the cone injectors are most sophisticated [1] their use in our case would require definition of their locations for each time step of the calculation. These injectors cannot be easily attached to the moving mesh. The surface injectors do not require specification of their location each time the vehicle moves. Contrary to the cone and point injectors the surface injector is always attached to the underlying geometry. Velocity magnitude and direction are specified for particles with mass released by the surface injectors. Massless particles are injected normal to surface and their velocity is not specified.

Probably the most difficult part of this analysis is to determine initial conditions for the generated sprays. Particle size distribution, particle velocity magnitude, its direction, and particle breakup properties are the key factors in the analysis. The literature on this topic is very limited since any experiments determining generation of a spray by rolling tires are difficult to conduct. In [2] tests with an original Tire Spray Simulator are presented as a source of information on the creation of a spray from tires. In the experiments an apparatus like the one shown in Figure 2.48 was used. Two tires were pressed against each other - one of them had a greatly simplified tread in the form of a single circumferential groove, and the other one had no tread to simulate a smooth road surface. Water was injected between the rolling tires and spray generated behind them was analyzed using digital particle imaging velocimetry technique (DPIV). Particle size distribution, the mean diameter and the breakup length were shown to depend on the Weber number. Measurements for the breakup length of the liquid sheet showed a dependence on Weber number proportional to $We^{-1/6}$. The range of droplet sizes and the mean diameter were found to decrease with Weber number by approximately $We^{-1/2}$ [2].

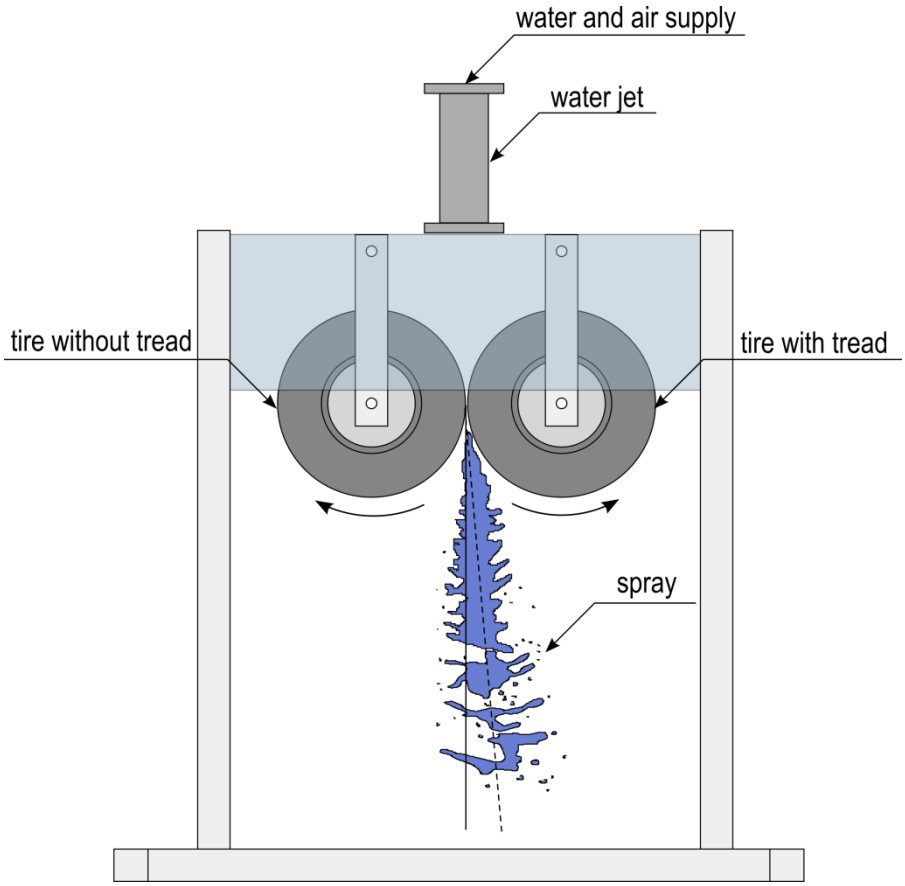

Figure 2.48: Schematic drawing of the Tire Spray Generator (based on [2])

Weber number in the test depends on properties of the water, tire speed and the tire groove width. For different Weber numbers different particle distributions were obtained at several locations behind the tires. In all tested cases the distribution of particles can be described by a log-normal distribution. One of such distributions is shown in Figure 2.49. The following approximate mean particle sizes were observed in the spray coming off the tire at a distance of 1.5 tire diameters from the end of the contact patch:

- For the lowest *We* = 2,700 distributions had a mean particle size of approximately 750 µ.
- For *We* = 10,900 distributions had a mean particle size of approximately 400 µ.
- For the highest *We* = 24,400 distributions had a mean particle size of approximately 300 µ.

We = 24,400 was associated with the tire surface velocity of 18 m/s. In our case the velocity of the tire surface is 26.8 m/s. Also the tire geometry is substantially different since commercial tires have multiple, circumferential and non-circumferential groves in a variety of tread patterns and larger diameter than the tested tire. Thus, the results listed here cannot be directly used as an input for the analysis of spray distribution coming from large trucks. Nevertheless, the mean values of the particle diameters were used as a basis for the further study.

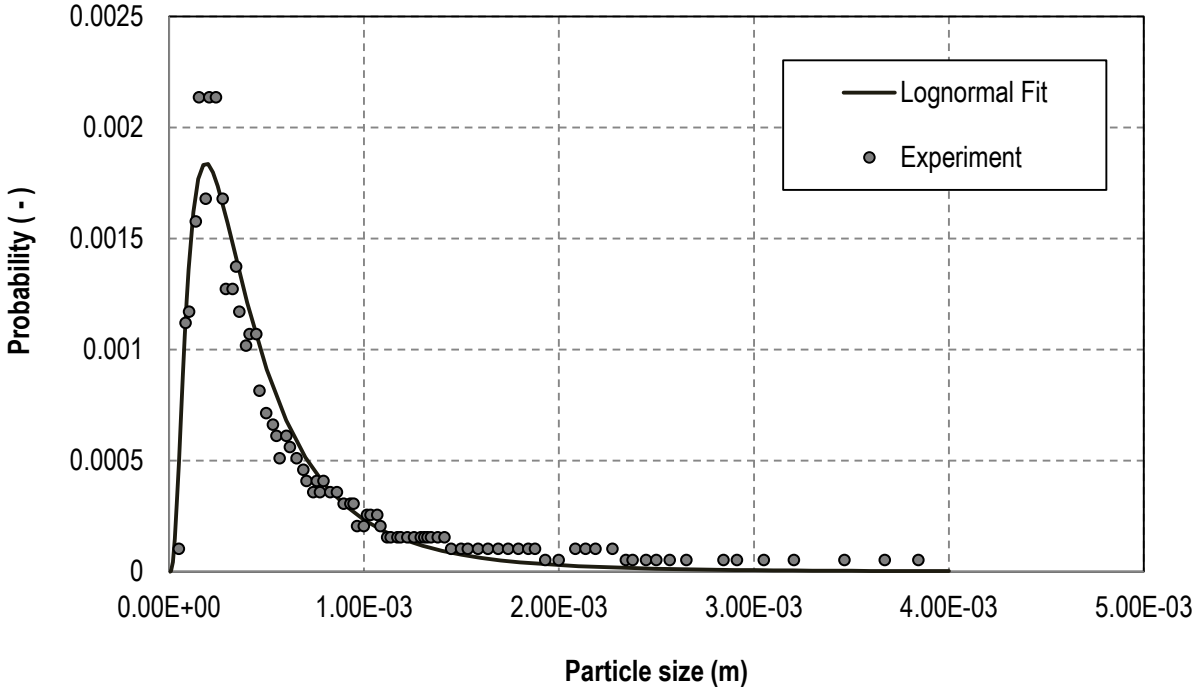

Figure 2.49: Particle size distribution in Tire Spray Generator test [2]

One set of simulations were conducted on a stationary vehicle ("sliding mesh with truck" from Figure 2.47) without the air domain and the bridge model. Of interest in this run was just the breakup of the particles due to their impact with the wheel well. A goal of this simulation was to find what size particles can be expected to leave the wheel well zone after the breakup. This size range is then used as a droplet injection boundary condition in the simulations of a moving vehicle, where it is too computationally expensive to use the breakup model.

The Bai-Gosman wall impingement model was activated in these simulations. Depending on the Weber and Laplace numbers for the droplets, the Bai-Gosman model is simulating a wide range of behaviors of wall impacting particles like: sticking, rebound, or break-up upon rebound (see Figure 2.50) [3].

The Weber number characterizes the ratio of inertial to surface tension forces and is defined as:

$$We = \frac{\rho V^2 D}{\sigma} \qquad 2.12$$

Where ρ is the carrier fluid density, V the slip velocity between the droplet and the carrier fluid, D is the drop diameter and σ is the droplet surface tension.

The Laplace number is a dimensionless number used in the characterization of free surface fluid dynamics. It relates the inertial and surface tension forces of the droplet to the viscous forces. It is also described as a ratio of surface tension to the momentum-transport inside a fluid.

It is defined as:

$$La = \frac{\rho \sigma D}{\mu^2} \qquad 2.13$$

Where μ is viscosity of the droplet liquid.

The boundaries between different regimes are defined in the updated Bai-Gosman model [3] and listed in Table 2.4. Implementation of this model in STAR-CCM+ includes temperature dependency of these boundary values. The user also specifies number of child particles upon break-up of particle and angle range for possible rebound. The default values of two child particles and angle range of 5 to 55 deg was used for the current analysis.

Table 2.4: Regime transition criteria [3]

Wall status	Regime transition state	Critical Weber number
Dry	Adhesion to Splash	$We = 2630La^{-0.183}$
Wet	Stick to Rebound	$We = 2$
Wet	Rebound to Spread	$We = 20$
Wet	Spread to Splash	$We = 1320La^{-0.183}$

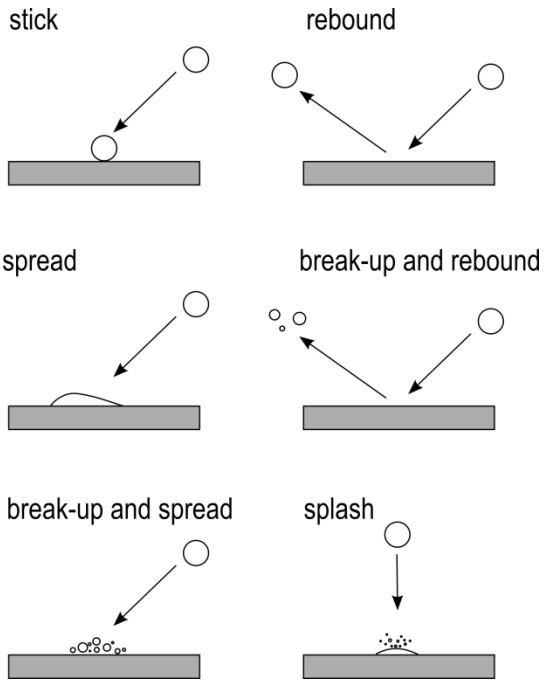

Figure 2.50: Possible particle behavior in Bai-Gosman model of wall impingement

In the simulation, droplets with a constant diameter were injected to the system from the tire tread surface. Three different sizes of particles were investigated, chosen based on the study presented in [2]: 0.3 mm, 0.5 mm, 0.7 mm. The particles were injected with velocity of 26.8 m/s (60 mph) at an angle of 15 degrees to the ground in the plane perpendicular to the wheel axles. The vehicle was considered

stationary but the rotation of the tire, movement of the bottom boundary (ground) and movement of the air was defined to represent motion of the vehicle with a velocity of 26.8 m/s (60 mph).

Currently the simulations for the 0.3 mm and 0.7 mm initial particle size are being run and these results will be shown in the next quarter. Only results for the size of 0.5 mm particles are reported. Figure 2.51 shows an intermediate state for this simulation. Droplets with injected size of 0.5 mm (red color) don't undergo breakup because they do not hit the wall of the wheel well. Droplets leaving the tire within the wheel well collide with the walls and breakup into a much smaller size before they are transported out via drag forces with the air flow. The droplets with smaller diameter (blue in figure) have a diameter around 100 microns.

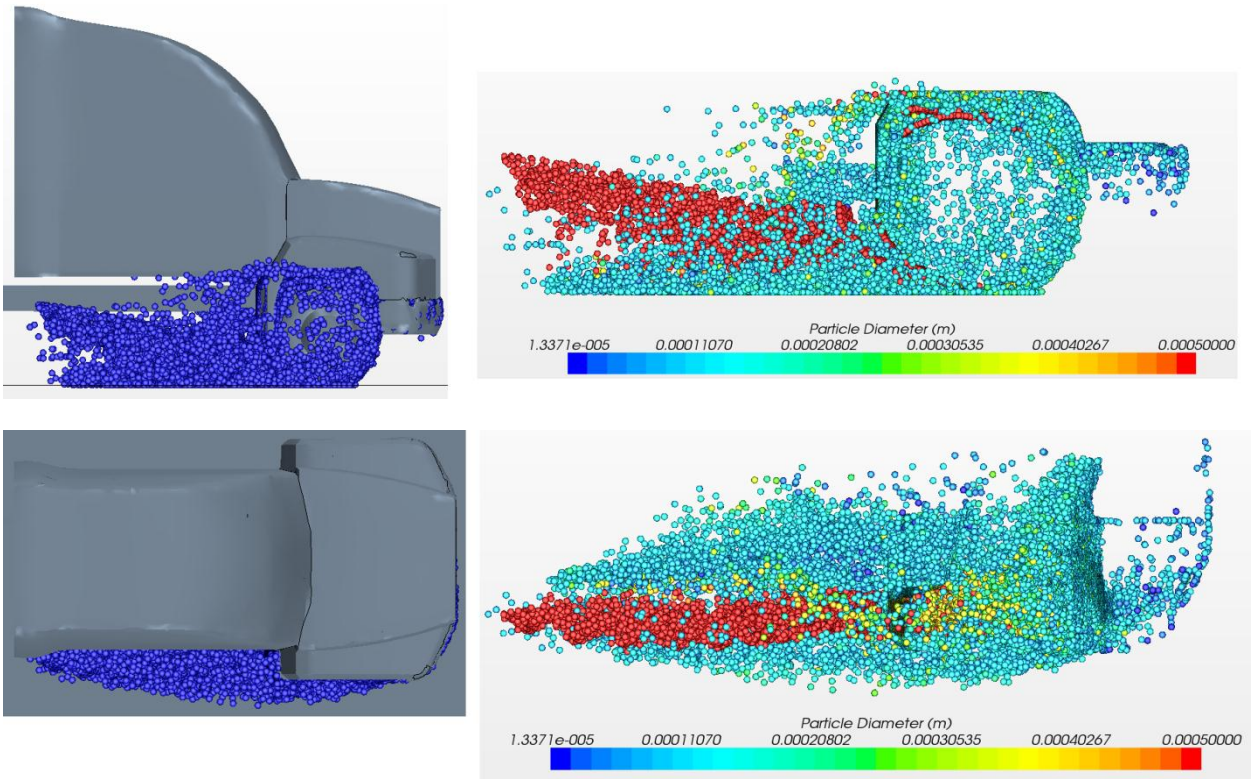

Figure 2.51: Particle breakup in the wheel well

Figure 2.52 shows the distribution of the particles after 0.5 sec of simulation. A substantial number of droplets have the original size because they did not experience any collisions. However, the peak of the droplet diameter is now around the size of 90 microns. As can be seen in Figure 2.51 (top view) only droplets with size around 100 microns (blue color) are leaving the wheel well to the side. Bigger droplets will not leave this area unless there are no obstacles in their way. Usually mud flaps and sometimes other devices are installed around the truck wheels to prevent this from happening. Thus, for further analysis it is safe to assume that only droplets that have undergone breakup need to be considered. This conclusion is in agreement with the findings from the research conducted at Lawrence Livermore National Laboratory reported in [4].

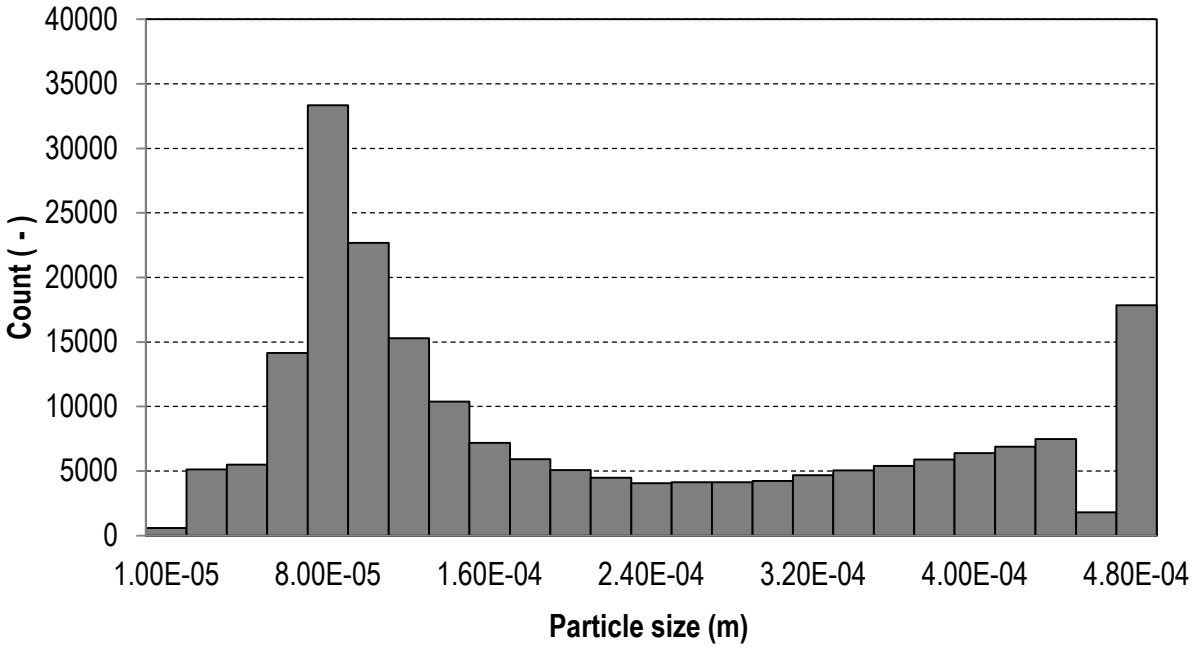

Figure 2.52: Particle distribution after break-up in the wheel well

2.3.1.3. Simulations of the moving truck

While the most important locations of the injectors are the wheel treads, a few cases have been run with the injectors attached to the cabin's edges. Figure 2.53 shows the location of the injector surfaces with surfaces at the rear side of the cabin. In Figure 2.54 droplets generated on these surfaces are displayed.

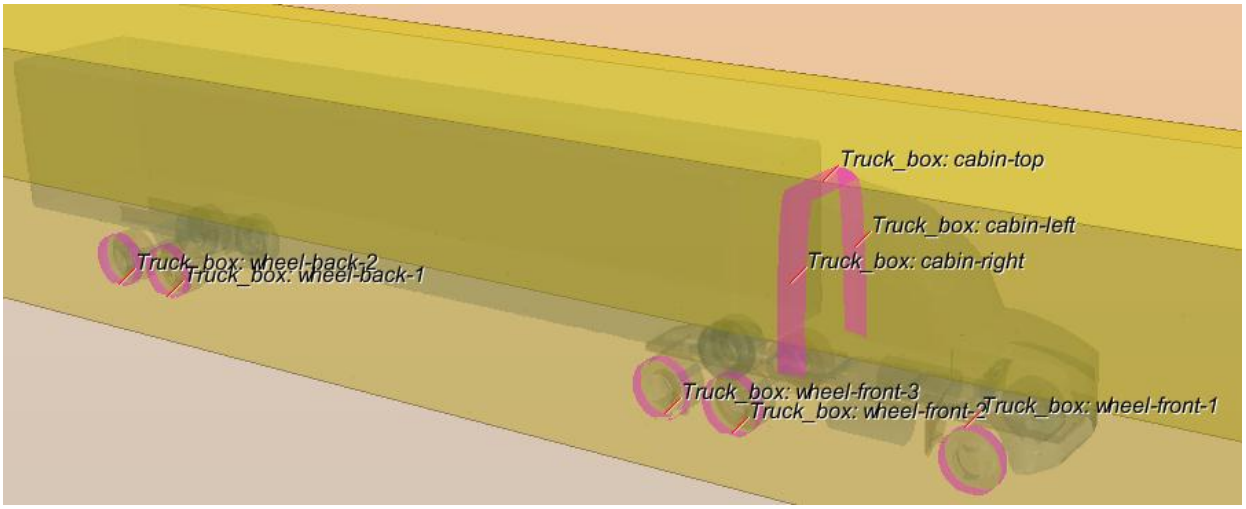

Figure 2.53: Location of surfaces used as surface injectors

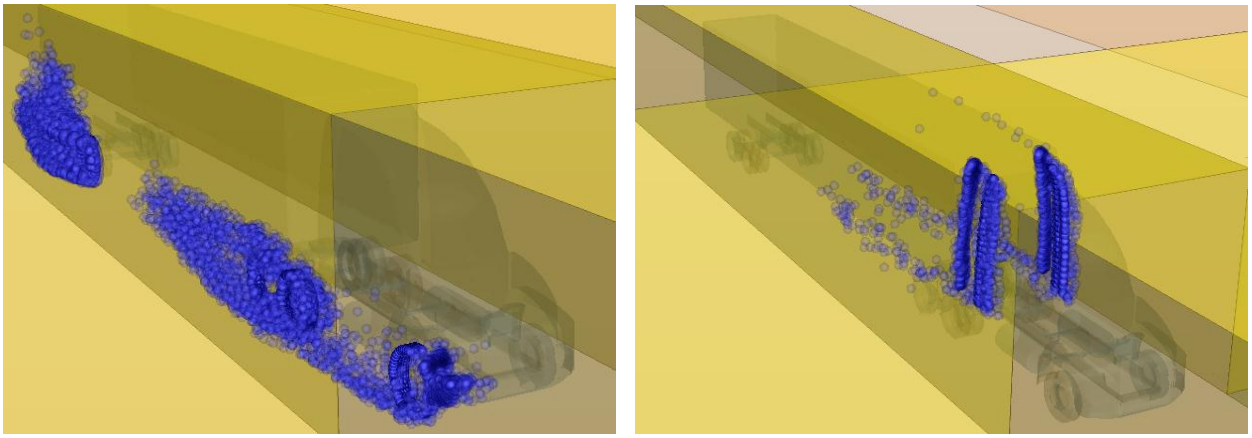

Figure 2.54: Particle generated on the injector surfaces

As the main goal of this study is to provide an assessment of possible travel paths of a salt spray generated by the tires to the bridge beams, several cases were analyzed. Table 2.5 lists completed cases and others, planned for analysis in the next quarter.

Table 2.5: List of analyzed cases

case	particle size	injector angle	injector location	boundary type under the bridge	number of vehicles
completed runs					
1	massless	-	top surface of the cabin	open	one
2	massless	-	side surfaces of the cabin	open	one
3	50 microns	(-1.0, -1.0, 0)	rear tire	open	one
4	100 microns	(-1.0, -1.0, 0)	rear tire	open	one
5	50 microns	(-1.0, -0.1, 1.0)	rear tire	open	one
6	100 microns	(-1.0, -0.1, 1.0)	rear tire	open	one
7	100 microns	(-1.0, 0.0, 0.268)	all tires	open	one
8	100 microns	(-1.0, 0.0, 0.268)	all tires	closed	one
in progress or planned runs					
9	100 microns	(-1.0, 0.0, 0.268)	all tires	open	two
10	100 microns	(-1.0, 0.0, 0.268)	all tires	closed	two
11	100 microns	(-1.0, 0.0, 0.268)	all tires	sloped	two

Massless particles released on the edges of cabin

In the first set of simulations massless particles were injected at the edges of the cabin. As shown in Figure 2.55, the droplets did not reach the level of bridge beams in any of the two analyzed cases of injectors on the top and sides of the cabin. Massless droplets strictly follow the streamlines of the flow and without additional flow disturbances i.e. another vehicle or wind, do not reach the bridge beams.

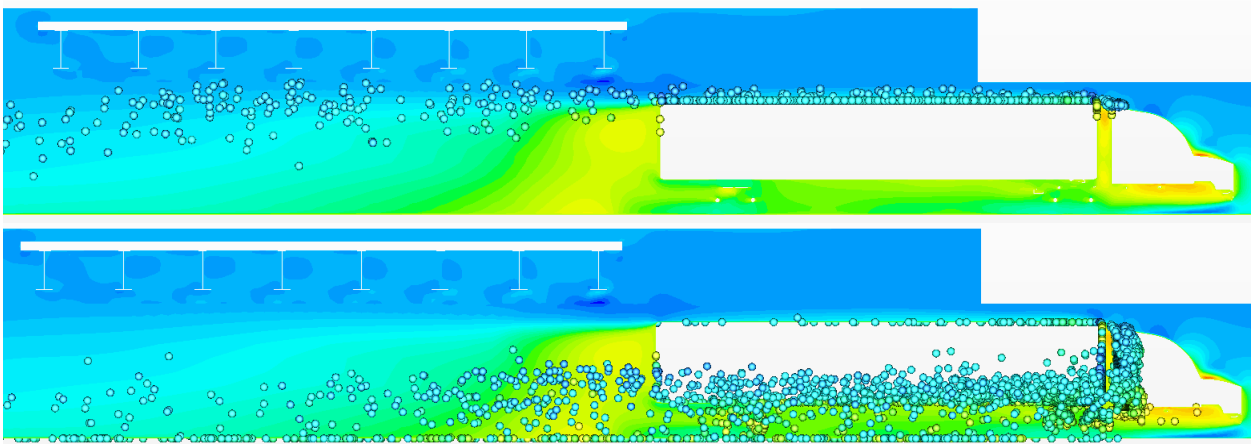

Figure 2.55: Velocity field around the truck and distribution of massless droplets injected at the cabin's edges

Droplets with mass released at the rear tires to the side of the truck

Droplet tracking is computationally expensive and requires very long run times (many days) when the number of droplets is large. For this reason, the simulations reported here have injection droplets from the rear wheel and all of the wheels on one side of the truck. This approach to studying droplet transport is reasonable because the number of droplet-droplet interactions is negligible and droplet number densities in the sprays from truck tires are not high enough to substantially alter the air flow. The initial models do not have mud flaps installed since the break-up of the droplets was not included here. First an angle of 45 degrees in the horizontal plane was assumed for injected droplets – vector (-1.0, -1.0, 0). Droplets with a diameter of 50 microns were injected at velocity of 26.8 m/s (60 mph). Figure 2.56 shows the tire spray droplet distribution of this simulation when the truck is already passed the bridge. Droplets thrown to the side are raised by the moving air to about half of height of the truck. The presence of the bridge does not change behavior of the droplets to a significant extent in this case.

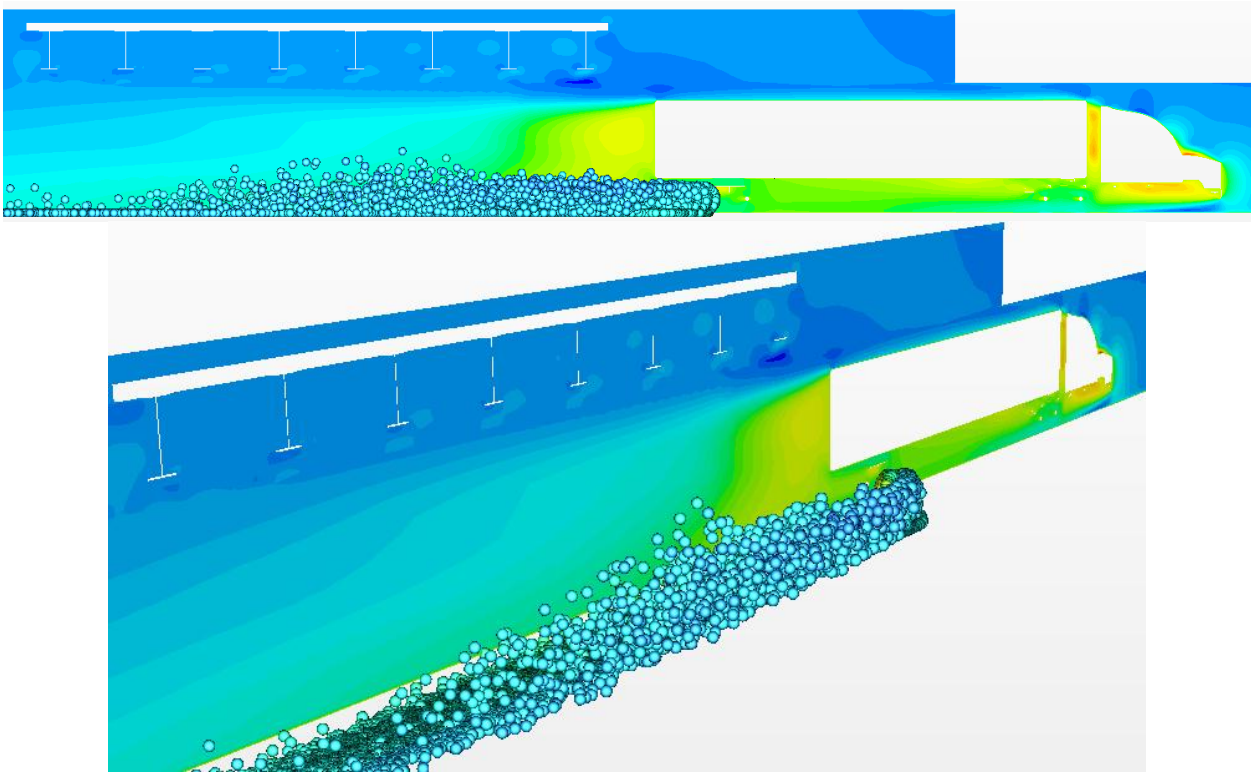

Figure 2.56: Velocity field around the truck and distribution of 50 micron droplets injected at the rear tire tread

Also to the side at the angle of 45 degrees, droplets with a diameter of 100 microns were injected. Figure 2.57 shows results of this simulation. Here the effect of air moving in the wake of the truck on droplets is negligible. Once the droplets leave the boundary layer of air moving with the truck, they decelerate quickly to the zero ambient wind speed in the simulation and settle to the ground under the influence of gravity.

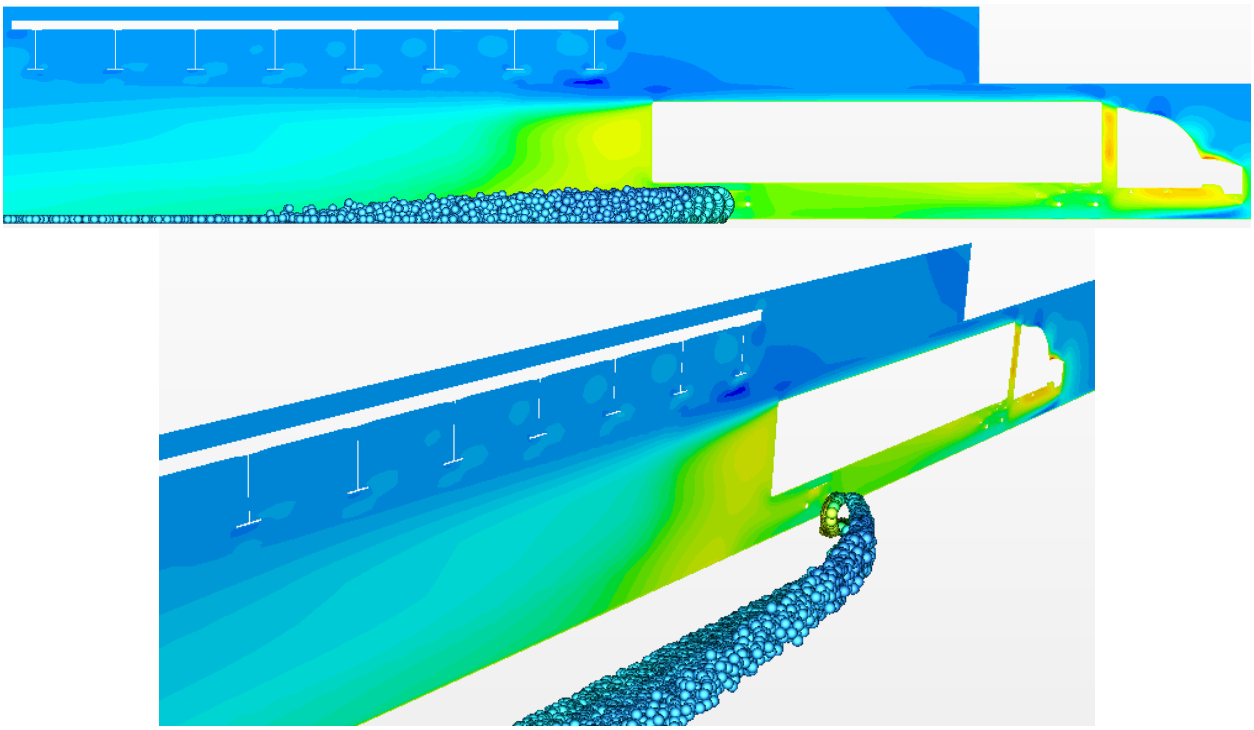

Figure 2.57: Velocity field around the truck and distribution of 100 micron droplets injected at the rear tire tread

Droplets with mass released on from the tires at the angle of 45 deg

The behavior of 50 micron droplets was also tested in a case where they were injected from the rear tire at the angle of 45 degrees in respect to the ground, determined by vector (-1.0, -0.1, 1.0). In this case the droplets were entering the air behind the vehicle with no mud flaps (a worst case scenario) that was traveling with the speed close to the vehicle velocity. Figure 2.58 shows the trajectories of these droplets. The droplets reach a maximum of about 2/3 of the trailer's height. Even in this worst case without the mud flaps, the droplets were not reaching the height of the beams in the bridge.

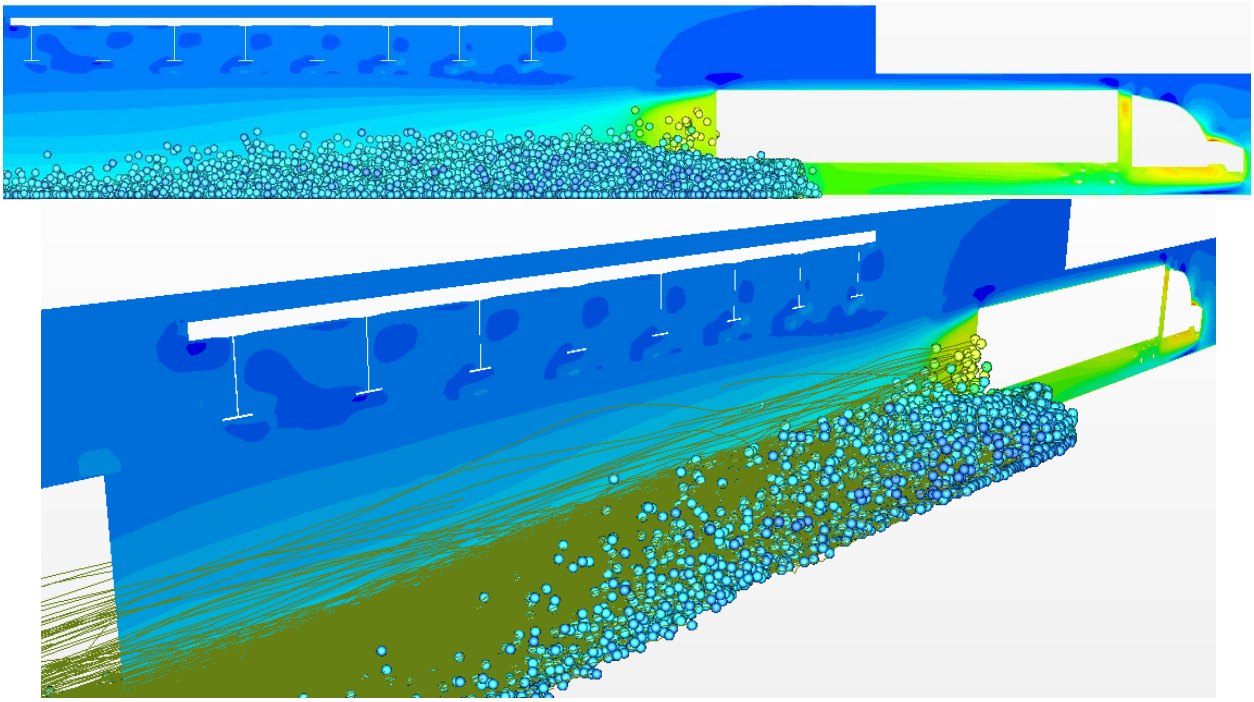

Figure 2.58: Velocity field around the truck and distribution of 50 micron droplets injected at the rear tire tread

A similar test was conducted for droplets with the diameter of 100 microns. Figure 2.59 shows the droplet distribution when the vehicle is leaving the bridge area. A nearly ballistic trajectory of droplets that reach maximum height can be seen. This case is also a worst case trial and not representative of normal conditions because the angle of injection is high and mud flaps are not present in the model. However, even in this extreme case, virtually no droplets are reaching the bridge beams.

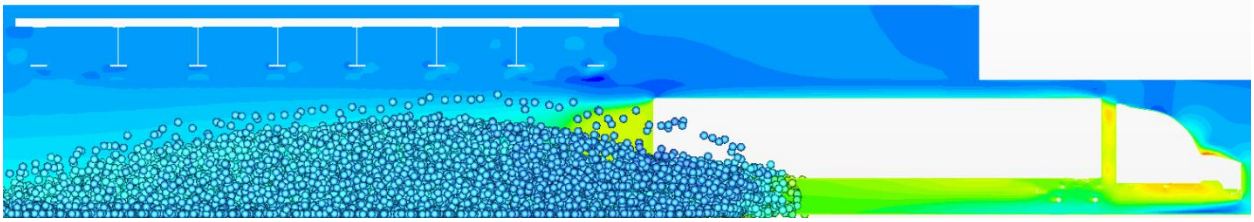

Figure 2.59: Velocity field around the truck and distribution of 100 micron droplets injected at the rear tire tread

Mass droplets released on from the tires at the angle of 15 deg

Based on the analysis conducted in [2] and observations of real trucks during rain storms, the angle of injection of droplets from underneath the wheel well and mud flaps is most realistic at angles less than about 15 degrees. Droplets with the diameter of 100 microns were selected for this analysis. Although this is a fairly large uncertainty in injection rates, size distribution, and injection angle, this case is closest to reality based on current knowledge and available data. Treads on all the tires on one side of the truck were selected as the injectors. As seen in Figure 2.60, droplets from the front tire are leaving the wheel well through the side although the initial angle of injection was in the vertical plane of vehicle travel (X-Y plane). This behavior has been noted in several observations of the production of spray from trucks on

the road during rains. Many droplets are lifted behind the truck and traveling with it. However, none of them reaches the level of the bridge beams.

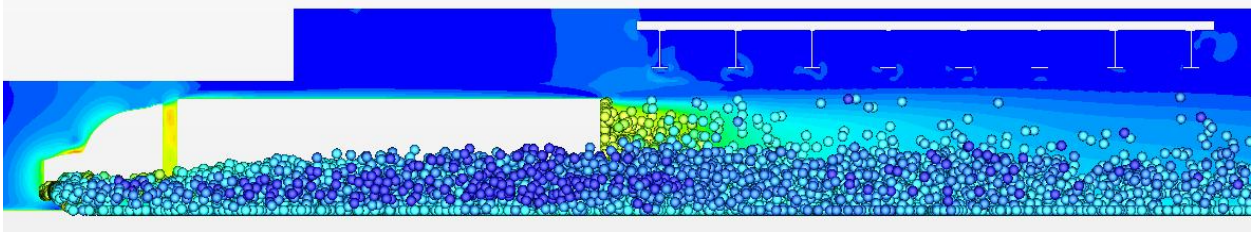

Figure 2.60: Velocity field around the truck and distribution of 100 micron droplets injected at all tire treads on one side of the vehicle

Figure 2.61 shows a picture of a truck traveling on a wet road. The spray around trailer tires and in the wake appears to be a fine mist qualitatively consistent with the droplet breakup modeling in Section 2.3.1.2. The visible part of the spray does not reach more than 2/3 of the trailer's height, which resembles the results presented in Figure 2.60.

Figure 2.61: Spray behind the truck driving on a wet road

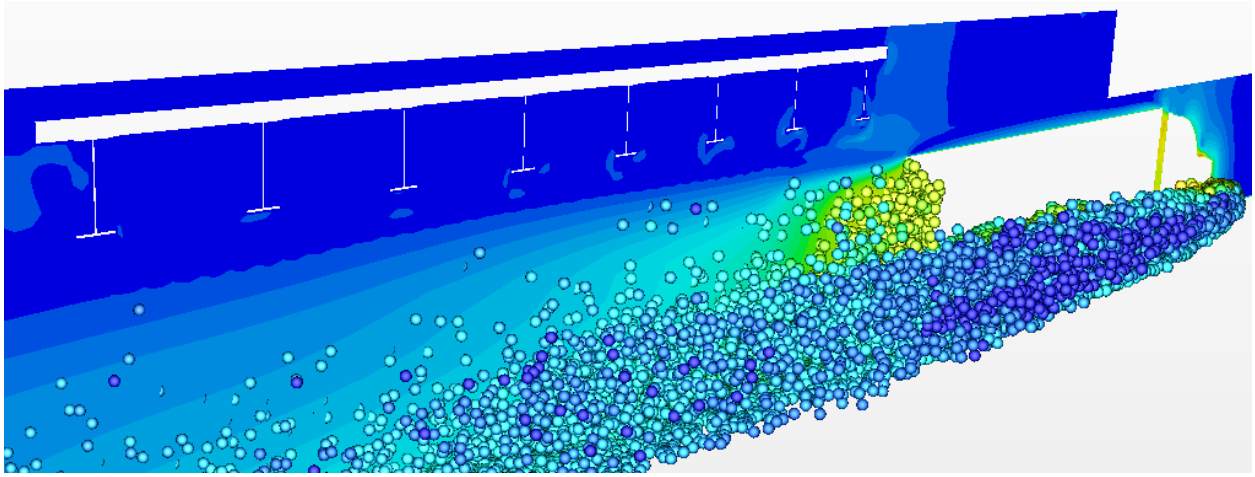

Figure 2.62: Velocity field around the truck and distribution of 100 micron droplets injected at all tire treads on one side of the vehicle

As shown in Figure 2.62 the droplets are leaving the wheel well area to the side of it (although the injection vector does not have a Y component (-1.0, 0.0, 0.268)). Similar behavior can also be observed in the real world. The pictures in Figure 2.63 show water droplet spray leaving the partially closed cavity around the wheels created by the mud flaps, the bottom of the trailer, and the back of the cab as a fine mist. The portion leaving from under the mud flaps moves primarily rearward, but the portion leaving

from the top of the tires has rearward flow blocked by the mud flaps and must move out to the side of the truck.

Figure 2.63: Generation of the fine spray mist on the side of the truck

From the simulations conducted so far it appears that the presence of the bridge deck and beams has little influence on the behavior of the droplets in the water spray generated by a truck moving at 26.8 m/s (60 mph). Another, possibly more important factor is the presence of obstacles on the side of the traveling vehicle. Although the bridges listed by TFHRC as affected by excessive corrosion have open space on the sides, the presence of walls on the sides is expected to influence the air flow pattern on the side and in the wake of trucks, which can affect droplet transport through drag. To test the effect of vertical bridge walls near the roadway, wall boundary conditions were applied on the interface between the truck box and the bridge domain. Figure 2.64 on the top shows the droplet distribution just as the truck is leaving the zone under the bridge with a vertical wall. Comparing to the case without a vertical wall shown in Figure 2.64, there are more droplets up near the bridge beams at about 5 seconds into the simulation. However, the simulation needs to be continued after the truck exits the zone under the bridge to determine if significant numbers of droplets hit the beams of the bridge. Figure 2.64 on the bottom shows droplets hitting the beams after 10 seconds of simulation. Figure 2.65 shows the history of particle hits per time step (0.02 s). There are 20 iterations per time step. The first droplet hit occurred at about 6.7 seconds and the last ones at about 9 seconds. Cumulatively no more than 50 droplets hit the beams of the bridge. This is a very small number considering the fact that each time step (0.02 sec) about 1300 droplets is injected to the system. A total of 650,000 droplets were injected into the system and only 50 hit the beams for a case where the truck had no mud flaps. The percentage of droplets in the drop wake spray that hit beams when a single truck passes under a bridge with no traffic appears to be negligibly small for the case with a vertical wall.

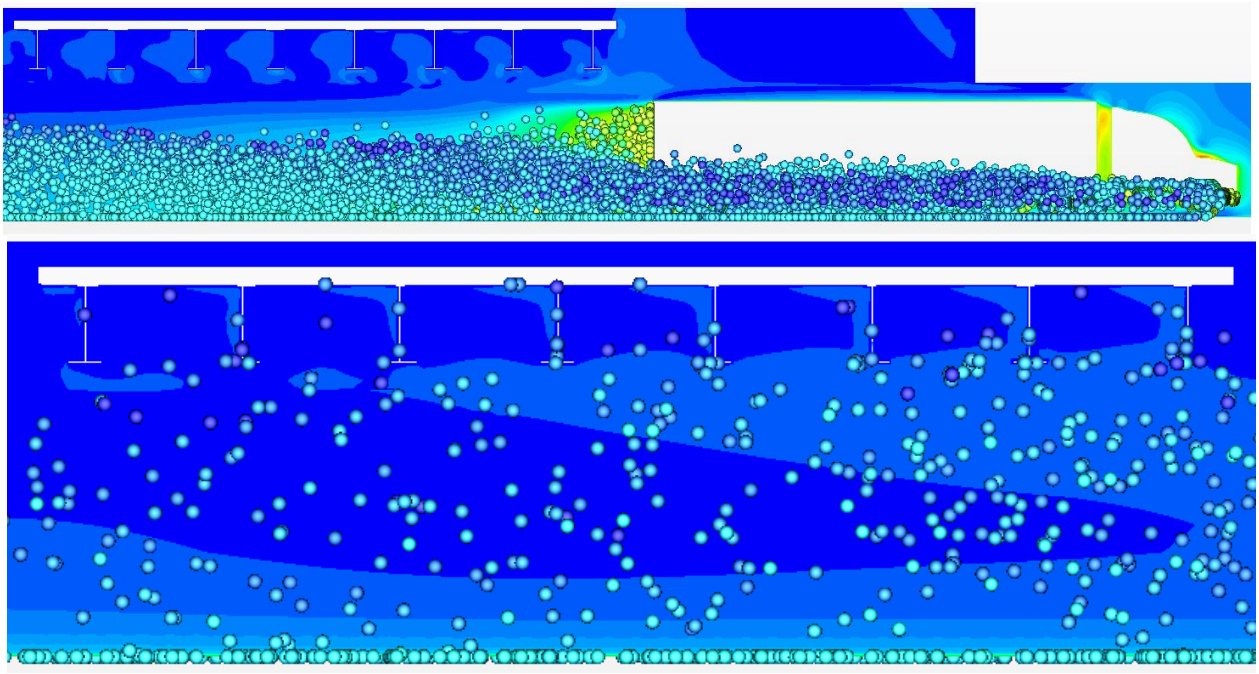

Figure 2.64: Velocity field around the truck and distribution of 100 micron droplets injected at all tire treads on one side of the vehicle

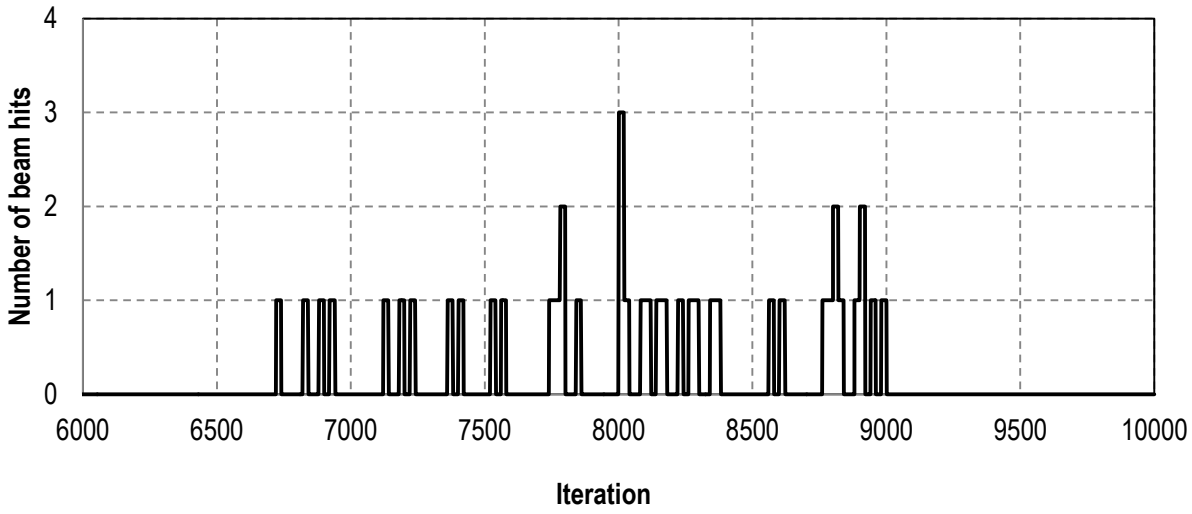

Figure 2.65: Count of droplets hitting the bridge beams during the simulation time

2.3.1.4. Planned simulations

As the initial runs did not indicate significant transport of droplets to the level of the bridge beams it was decided that subsequent runs should involve other factors that may influence the behavior of the droplets. Three major factors are:

1) presence of other vehicles on the road

2) additional wind gusts moving the droplets up higher
3) resuspension of droplets and dry road salt as an aerosol by traffic hours to days after salting the road.

Figure 2.66 shows the geometry of the model with two trucks that is being currently analyzed. The results from this simulation and others will be presented in the next report.

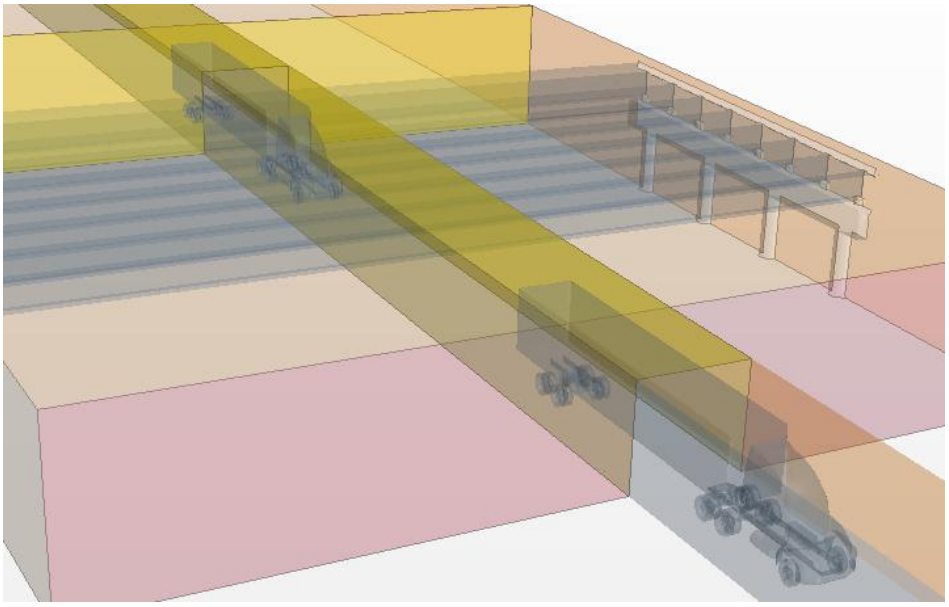

Figure 2.66: Geometry of the model with two trucks

2.3.2. References

[1] CD-adapco, User Guide STAR-CCM+ Version 6.02.008, 2011

[2] Ch.A. Radovich, *Experiments of spray from a rolling tire*, PhD Thesis, University of Southern California, August, 2010

[3] C.X. Bai, H. Rusche, A.D. Gosman, *Modeling of Gasoline Spray Impingement*, Department of Mechanical Engineering Imperial College of Science, Technology and Medicine, Atomization and Sprays (2002), Vol 12, Issue 1-3, pp 1-28

[4] J.S. Paschkewitz, *Simulation of spray dispersion in a simplified heavy vehicle wake*, Lawrence Livermore National Lab report No. UCRL-TR-218207, January 17, 2006

3. Computational Multiphysics Mechanics Applications

3.1. Multiphysics Simulation of Salt Spray Transport

Effort during the quarter focused on CFD modeling using the sliding mesh capabilities of STAR-CCM+. The progress is reported in Section 2.3.

3.2. Wind Engineering

3.2.1. Vehicle Stability under High Wind Loading

Ground vehicles, such as automobiles, trucks and trains, are often subjected to crosswinds that can lead to vehicle instability and, in the worst case, vehicle rollover. The current state-of-the-art for performing nonlinear transient analysis of vehicles opens the door to investigate this important and complex phenomenon of wind-structure interaction. At TRACC current capabilities exist to perform coupled wind-structure interaction on a high performance computer, and this should be a long range goal for this project. However, before embarking on that path, it is always prudent to approach the problem in an incremental fashion, i.e., with a series of increasing more complex models. By doing this, a greater understanding of the relative importance of the effect of different physics and a high confidence in the final results will be achieved. This reporting period describes a simplified approach in which the wind is treated as a pressure load on the side of the vehicle. Future work will move toward doing a multi-physics approach, i.e., coupled fluid-structure interaction.

For the first group of numerical simulations, a fairly complex model for an 8000S vehicle class truck was used. The following vehicles satisfy the requirements of the 8000S vehicle class: Ford, GMC, Chevrolet, Freightliner, and International. Instead of doing a coupled Computational Structural Mechanics-Computational Fluid Dynamics analysis, the wind was modeled as a constant pressure load on the windward side of the truck. The following sections provide details and some preliminary results.

3.2.1.1. Cargo Loading, Wind Loading, Road Condition and Vehicle Velocity :

Cargo Loading

A complex finite element model for the 8000S vehicle was downloaded from the model repository at the National Crash Analysis Center (NCAC) [1]. The model was for a Ford F-800 Single Unit Truck (SUT). This SUT is designed with two-axels, a rear wheel drive and a van type cargo body. It should be noted that this model was developed for simulating SUT crashes into roadside barriers, and thus, modeling features related to that type of analysis were included in great detail. Specifically, the truck model was developed to be used in simulations of Test Level 4 impacts and was to represent an 8000S test vehicle. Unfortunately, some of the features needed for crosswind loading were not properly accounted for and, thus, were added for wind loading analysis. In addition, because the physical SUT used in the barrier crash tests is not a Ford F-800, ballast mass was added in the cargo body of the model to make up the difference.

The recommended properties for 8000S test vehicles are as follows (Table 3.1): curb mass equal to 5.45 tonnes; ballast mass as needed; test inertia (gross vehicle mass equal to 8.00 tonnes. A complete description of the finite element model is given in [2]. The modeled mass of the truck was 5.270 tonne and the ballast mass was 2.872 tonne giving a total mass of 8.142 tonne. It is seen that the model for the Ford F800 truck meets the recommended properties of for an 8000S test vehicle.

However, it is important to note that a quick check on the internet [3] reveals differences between a typical Ford F800 and the Ford F800 finite element model used to represent the 8000S test vehicle. For example, for a typical F800 truck the following data (Table 3.1) was found: curb mass equal to 3.62 tonne (66% of the model); gross vehicle mass equal to 11.8 tonne (48% larger than the model); and payload equal to 8.174 tonne, (3.2 times larger than the ballast).

Table 3.1: Comparison of finite element model for a SUT to a Ford F800 truck.

	Curb Mass	**Curb Weight**	**Ballast Mass or Payload**	**Ballast Weight or Payload**	**Gross Vehicle Mass**	**Gross Vehicle Weight**
NCAC Finite Element Model [1]	5.45 tonne	53,000 N (12,000 lb)	2.55 tonne	25,000 N (5,620 lb)	8 tonne	78,000 N (17,630 lb)
Ford F800 Truck [3]	3.62 tonne	35,490 N (7,979 lb)	8.174 tonne	80,160 N (18,021 lb)	11.8 tonne	115,700 N (26,000 lb)

In the following work, the NCAC model had to be used because of the lack of a finite element model for the heavier F800. For this initial study, the cargo was represented by a fixed (in size and location) rectilinear mass inside the cargo body (Figure 3.1). This mass was rightfully referred to as ballast in [2], but in this study it represents cargo and will be referred to as such. To study the effect of different cargo weights, the density of the cargo material was varied as shown in Table 3.2 . The cargo mass affects the position of the center of gravity (COG), which is a crucial factor to estimate rollover. However for this initial study, the COG for the cargo mass is fixed because the cargo is fixed in size and location, but the COG for the combined truck and cargo will vary as the density of the cargo changes.

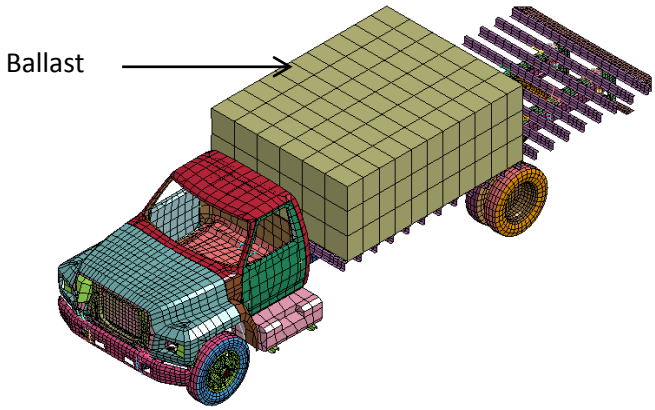

Figure 3.1: Ballast portion [1]

Table 3.2: Cargo loads

Cargo	Load Condition		
	100% Mass	**50% Mass**	**10% Mass**
Density (tonne/mm^3)	3.136×10^{-10}	1.568×10^{-10}	3.136×10^{-11}
Mass (tonne)	2.80938	1.40469	0.280938

Wind Loading

As a truck travels down a highway under no wind conditions, it is subjected to aerodynamic loading along the length of the truck because of vehicle speed – a sort of pseudo wind. In addition, the truck can be subjected to aerodynamic loading because of crosswinds. Records show that horizontal wind speed varies with time. Within intervals of about 300 seconds, wind speed history records [4] show that wind gusts occur about a mean wind speed. For this preliminary analysis, it is assumed that aerodynamic loading across the SUT is considered to be equal to a horizontal crosswind with a constant speed. Most of the simulations reported here are for about 5 seconds; so this assumption is reasonable. It is further assumed that the crosswind speed does not vary with the height of the vehicle, which is not exactly true since the wind speed at ground level is zero. The across-the-truck aerodynamic loading is applied to the driver side of the truck. As described in the last Quarterly Report [5], the pressure applied to the side of the truck was obtained by multiplying the stagnation pressure, which is a function of the wind speed, by the drag coefficient. The value for the drag coefficient was taken to be 1.0. It is noted that a drag coefficient specific to the F-800 could not be located.

The Beaufort Wind Scale (Table 3.3) provides a correlation of wind speed with quantitative and qualitative descriptions that are identified by their Beaufort Number (BN). Table 3.3 shows that gale winds begin at 32 mph (BN = 7) and end at 54 mph (BN = 9). The storm category is defined by BN = 10

and BN = 11, and the wind range is from 55 mph to 72 mph. The hurricane category is BN =12 and the winds are 73 mph and higher.

Table 3.3: Beaufort Wind

Beaufort Number	Wind speed (MPH)	Description
0	<1	Still, calm air
1	1-3	Light Air
2	4-7	Light Breeze
3	8-12	Gentle Breeze
4	13-18	Moderate Breeze
5	19-24	Fresh Breeze
6	25-31	Strong Breeze
7	32-38	Moderate or Near Gale
8	39-46	Gale or Fresh Gale
9	47-54	Strong Gale
10	55-63	Whole Gale or Storm
11	64-72	Violent Storm
12	73+	Hurricane

Road Condition

The road was assumed to be a flat surface. The traction between the tires and road surface affects the response of the truck to wind loading. For this initial analysis, the surface condition of the road was specified by the coefficient of friction (COF) between the tire and road surface. The value of the COF varies between its static and dynamic value. Prior to sliding, the static value governs. During sliding, however, the COF varies as a function of the sliding velocity. In this first analysis, the COF is taken to be constant and equal to the static value as given in Table 3.4 for each road condition. This assumption will be removed in subsequent analyses.

Table 3.4: Coefficient of friction for dry, wet and ice road conditions.

Condition	Dry	Wet	Ice
COF	0.9	0.5	0.2

Vehicle Velocity

The Ford F800 is a rear wheel drive truck; thus, the velocity of the truck is determined by the rotational speed of the rear wheels and the traction between the wheels and road. The rear wheels move the truck in the direction normal to the rear axle; the front steering wheels determine the direction of

travel. Because the downloaded Ford F800 SUT truck model was developed for crash analysis, the velocity at all the nodes within the model are the same, which for crash analysis is the correct initial condition.

The condition for wind loading, however, is more complicated. First, whenever a rear wheel lifts off, the traction from that wheel reduces to zero, and the truck is driven only by the opposite wheel. Second, when the horizontal wind rotates the truck relative to the original direction, the drive wheels will still tend to drive the truck in the direction normal to the rear axle, and the truck driver will try to compensate by steering the truck. Because this work represents a first look at this problem, the crash analysis assumption was retained. This assumption will be removed in subsequent, more complex analyses.

3.2.1.2. Simulation results

The results from the numerical simulations for the transient dynamic response of a SUT loaded by wind on the driver's side are described here. The general rotational transient behavior of the SUT is that the wind-load causes the vehicle to pitch, roll and yaw about the center of mass. Under the right set of conditions, a wheel will lose contact with the ground and liftoff. The time at which a wheel lifts off the pavement can be determined as the time at which the contact force between the wheel and ground becomes zero.

To measure the forces generated by the wheels on the ground surface, each wheel is in contact with a separate rigid wall. A rigid wall is a LS-DYNA feature that can be used to measure contact forces, which for our study is the force between a wheel and the pavement. Studying the contact forces helps understand the weight transfer of the model as it is being influenced by the wind. The wind load is applied to right side of the model, which would cause the right side of the truck to lift off the road surface. Note in Figure 3.2, it appears that the loading is also applied to the cargo, but this is not the case. Simulations show that the driver side rear wheel is the first to liftoff. Eventually, the truck may rollover. The driver side rear wheel (right rear tire) is in contact with rigid wall number 3 of the model, and thus, analyzing the force on this rigid wall would let us know the exact time of liftoff.

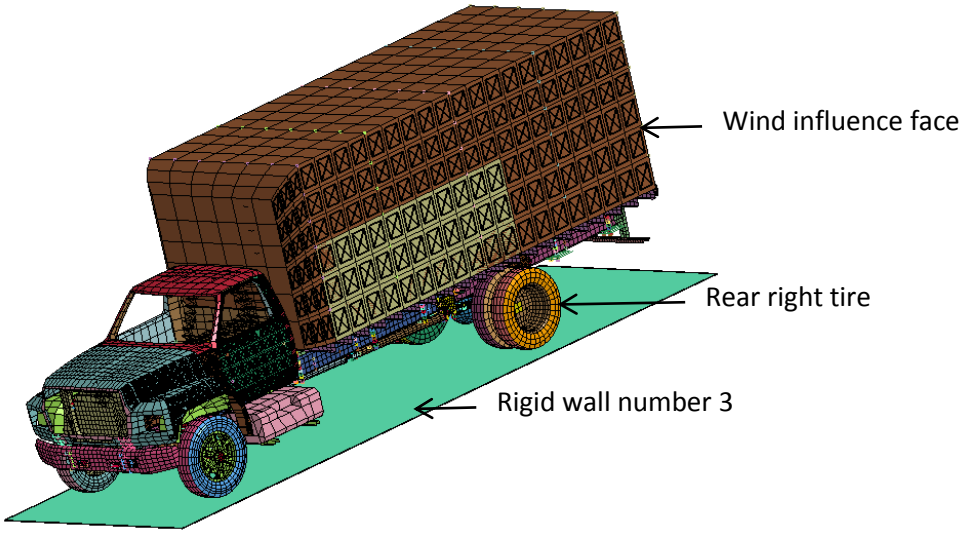

Figure 3.2: Wind influence face and rigid-wall attached with right wheel [1]

Figure 3.3 shows the driver-side rear wheel just after liftoff. In the extreme case, the SUT will rollover as shown in Figure 3.4. The remainder of this section describes preliminary results obtained using the SUT model described above.

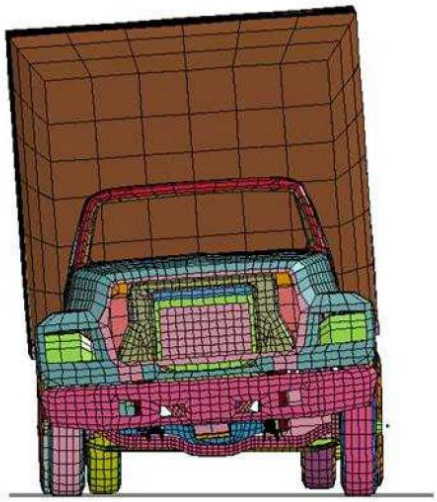

Figure 3.3: Configuration of SUT with driver side rear wheel liftoff.

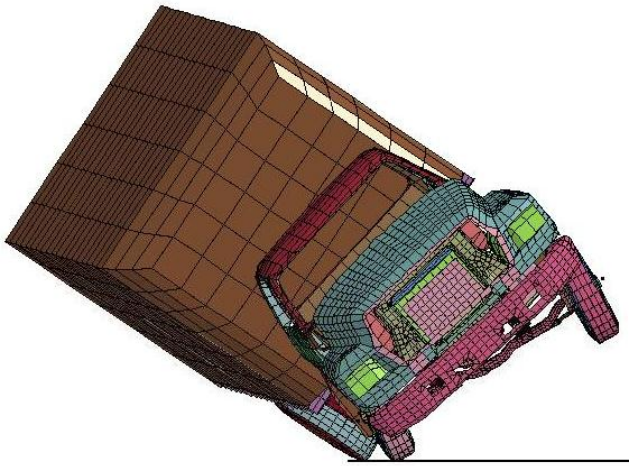

Figure 3.4: Configuration of SUT in the process of rolling over.

Critical driving speeds for vehicle rollover and side slip

The rollover response of the model with different cargo loading conditions and different coefficients of friction (COF) between the tires and road surface is shown in Figure 3.5 (dry surface, COF = 0.9) and Figure 3.6 (wet surface, COF = 0.5). The vehicle with a 10% cargo load will roll over at lower speeds than the fully loaded (100% cargo) for all speeds and both the dry and wet road conditions.

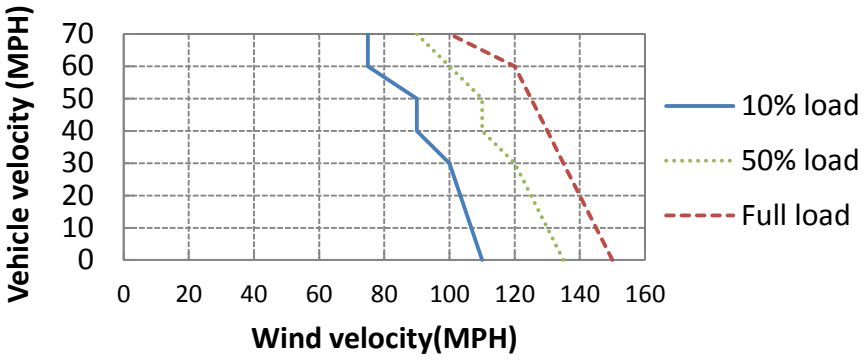

Figure 3.5: Critical driving speed for rollover on dry pavement (μ=0.9)

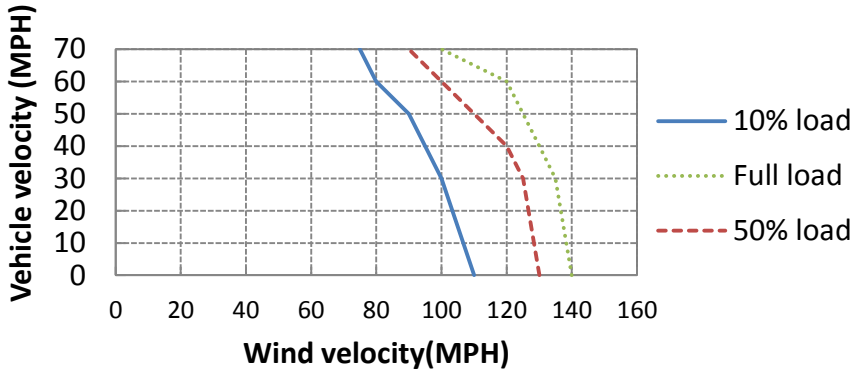

Figure 3.6: Critical driving speed for rollover on wet pavement (μ=0.5)

The graphs of critical driving speeds for sideslip and rollover under different road conditions (i.e., coefficients of friction) and cargo loading are shown from Figure 3.7 to Figure 3.14. Figure 3.7 to Figure 3.9 illustrates the rollover and sideslip behavior of vehicle travelling on dry road surface (COF = 0.9) for full, 50%, and 10% cargo loading condition.

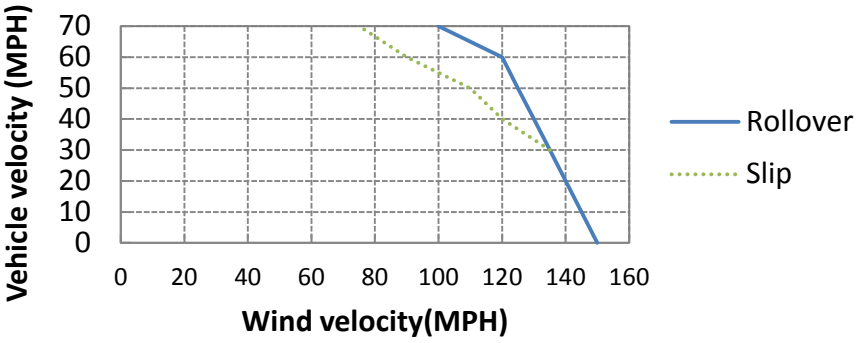

Figure 3.7: Critical driving speed for sideslip and rollover on dry pavement (μ=0.9) for a truck with a full cargo load.

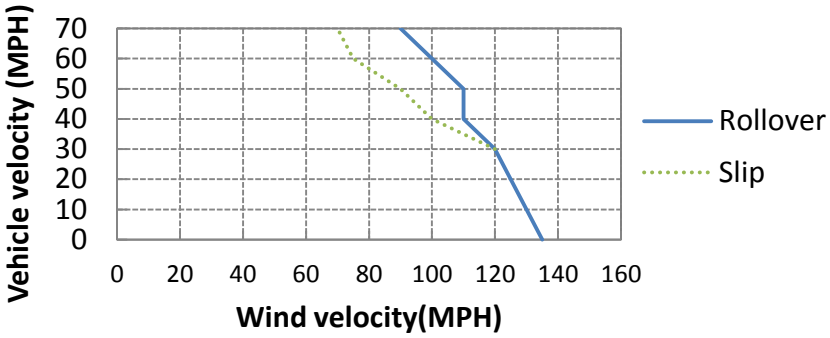

Figure 3.8: Critical driving speed for sideslip and rollover on dry pavement (μ=0.9) for a truck with a 50% cargo load

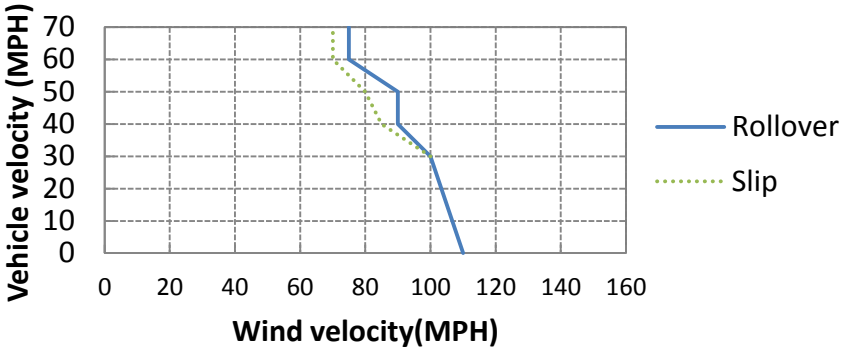

Figure 3.9: Critical driving speed for sideslip and rollover on dry pavement (μ=0.9) for a truck with 10% cargo load.

Figure 3.10 to Figure 3.12 shows the onset of sideslip and rollover of a truck travelling on a wet road surface (COF = 0.5) with 100 percent, 50 percent and 10 percent cargo loading conditions.

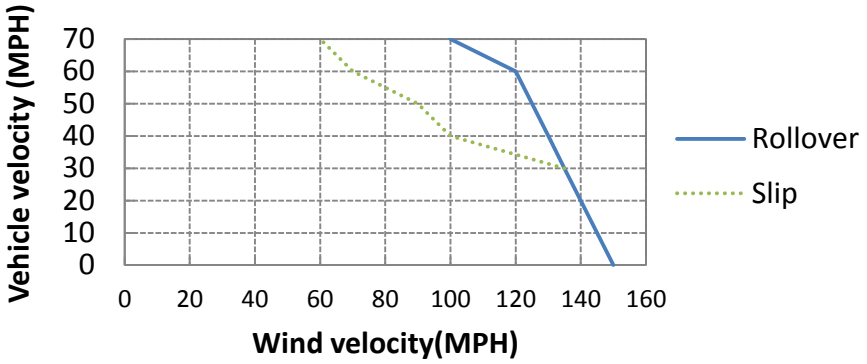

Figure 3.10: Critical driving speed for sideslip and rollover on wet pavement (μ=0.5) full cargo load.

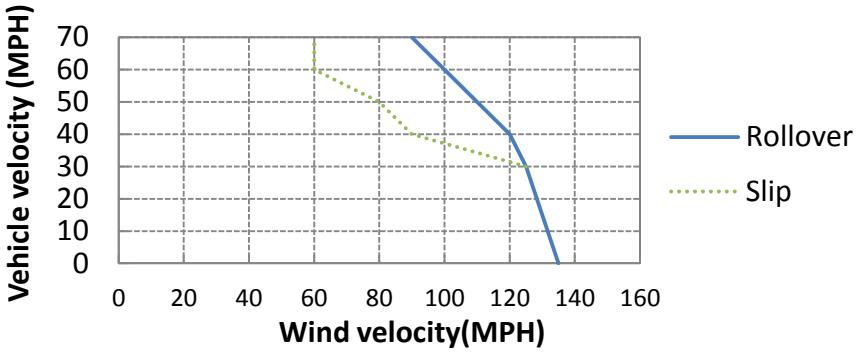

Figure 3.11: Critical driving speed for sideslip and rollover on wet pavement (μ=0.5) with 50% cargo load.

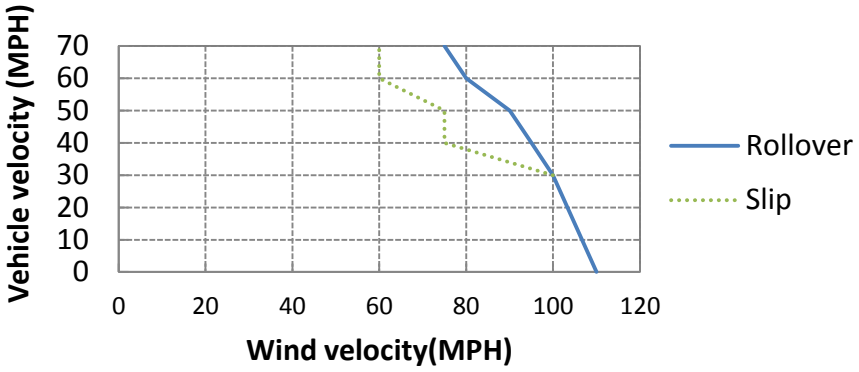

Figure 3.12: Critical driving speed for sideslip and rollover on wet pavement (μ=0.5) with 10% cargo load.

The onset of sideslip and rollover for a truck travelling over an ice covered road surface (COF = 0.1) with full, 50% and 10% cargo loading is shown in Figure 3.13 to Figure 3.15. The simulation results indicate that no rollover will occur for this low value of the COF. However, considering the situation in which the truck reaches the shoulder – which may be a gravel shoulder – the COF could jump from 0.1 to 0.5, and this could initiate rollover. However, this condition was not simulated here.

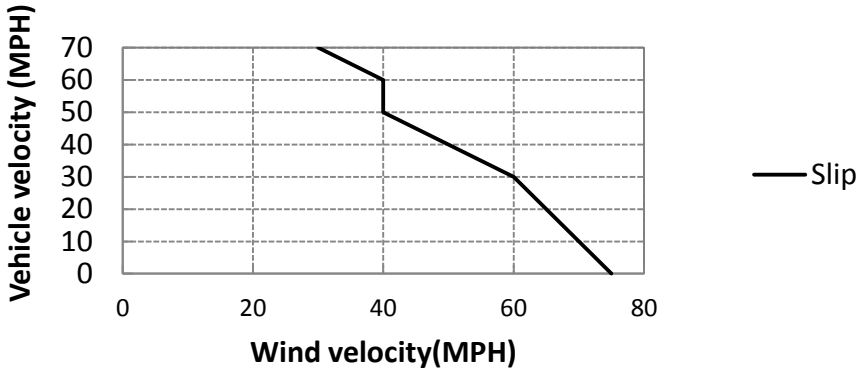

Figure 3.13: Critical driving speed for sideslip on icy pavement (μ=0.1) with full cargo load)

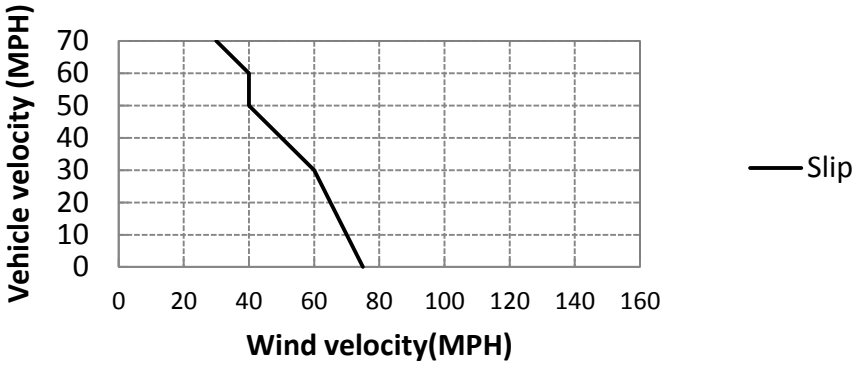

Figure 3.14: Critical driving speed for sideslip on icy pavement (μ=0.1) with 50% cargo load

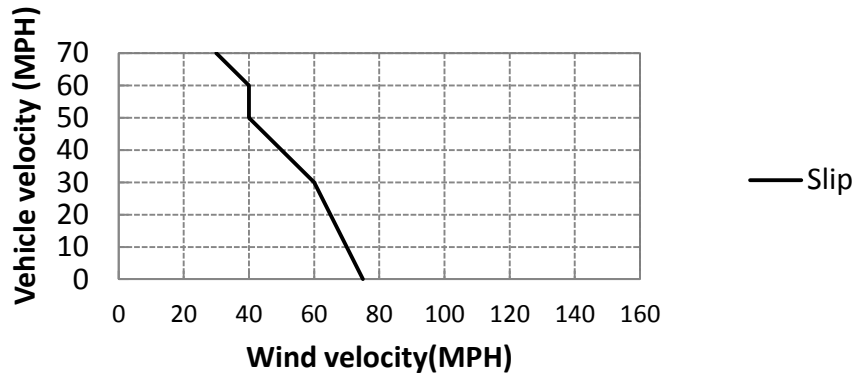

Figure 3.15: Critical driving speed for sideslip on icy payment (μ=0.1) with 10% cargo load

Critical *sustained* time *for initial wheel liftoff and vehicle* rollover

Since the wind loading was considered to be constant during each simulation, it is interesting to study the length of time that the wind would have to act for a wheel to lose contact with the ground, i.e., the critical sustained time for initial lift-off. Similarly, the critical sustained time for rollover is of interest. Figure 3.16 shows the time history of the contact force for the driver's side rear wheel, which is the first wheel to lift off, when the SUT is subjected to a crosswind of 75 mph. First gravity is applied to the vehicle, and static equilibrium is reached at 0.5 seconds with the contact force between the wheel and pavement being 33 kN. Next the constant magnitude wind loading is applied to the driver's side of the SUT. It is seen that under the constant wind force, the truck rocks back and forth several times with the wheel lifting off the road until at about 5 sec the wheel lifts off the road and the truck rolls over – recall the wind loading is applied at 0.5 sec.

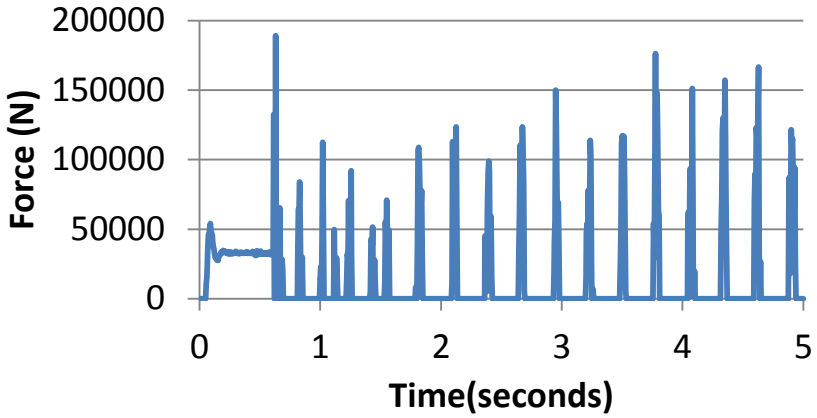

Figure 3.16: **Temporal contact force history for driver side rear tire under a 75 mph crosswind**

The graphs of critical sustained time – i.e., the minimum length of time under constant wind loading – for liftoff and rollover for different coefficients of friction and cargo loading combinations are shown in Figure 3.17 to Figure 3.28 .For the full-load case, Figure 3.17 to Figure 3.18 show the critical sustained times for initial liftoff and the onset of a rollover, respectively. The 0.9 value for the COF represented a dry surface. It is seen that at a vehicle speed of 40 MPH, it would take a 75 MPH wind 4.6 sec to cause a liftoff. However, at this vehicle speed and wind speed, no rollover would occur.

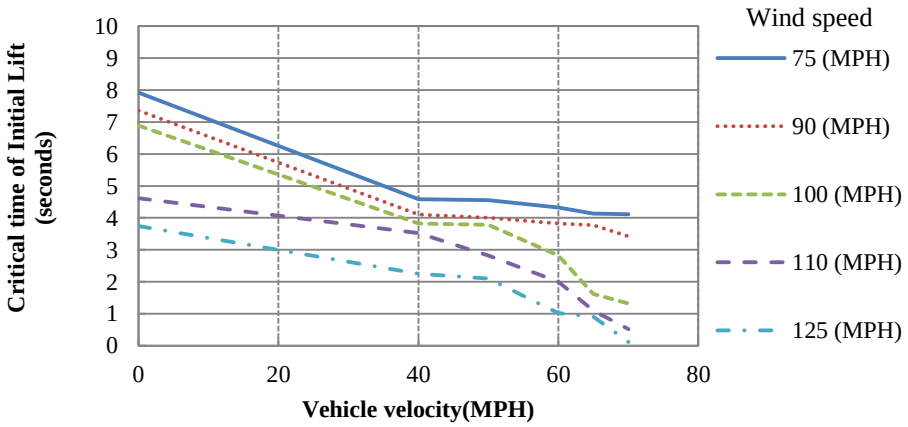

Figure 3.17: Critical sustained time for initial liftoff on dry pavement (μ=0.9) with full cargo load

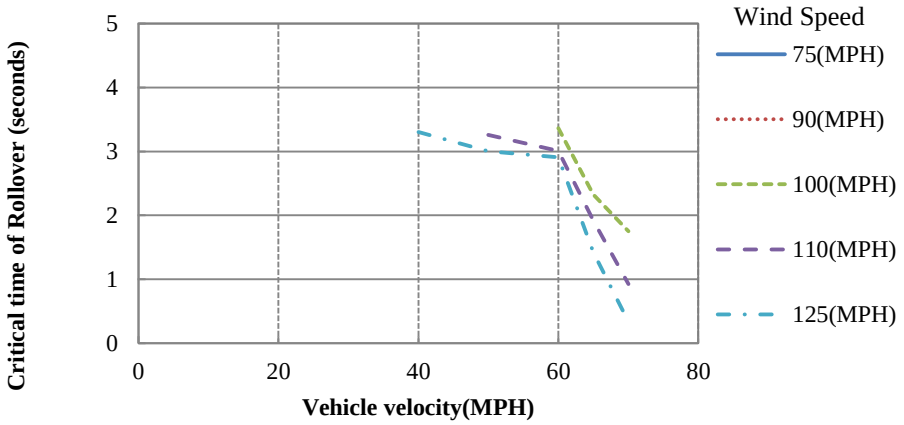

Figure 3.18: Critical sustained time for rollover on dry pavement (μ=0.9) with full cargo load

Figure 3.19 and Figure 3.20 show the results for a truck with 50% cargo load traveling at 40 MPH on dry pavement. A steady wind of 75 MPH lasting for 3.5 sec would be sufficient for liftoff. Similar to the above results, no rollover would occur.

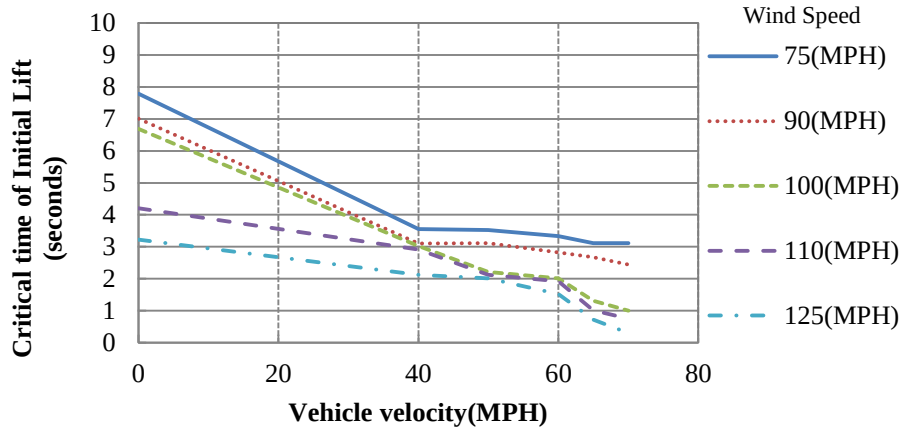

Figure 3.19: Critical sustained time for initial liftoff on dry pavement (μ=0.9) with 50% cargo load

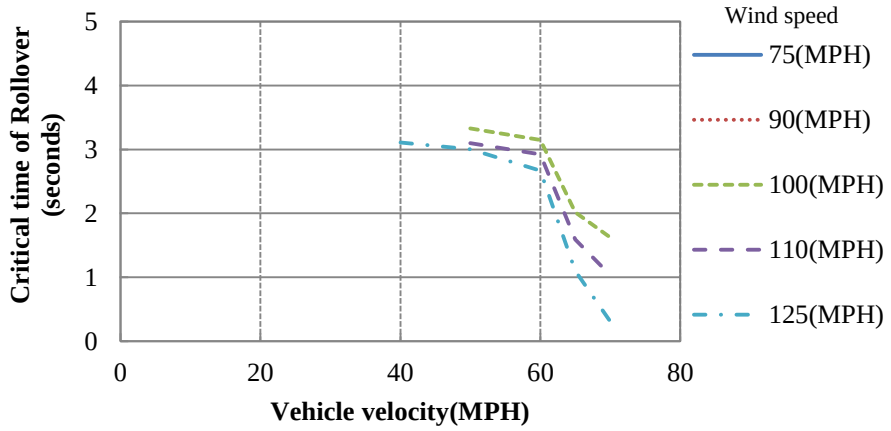

Figure 3.20: Critical sustained time for rollover on dry pavement (μ=0.9) with 50% cargo load

For the case with a 10% cargo load, Figure 3.21 and Figure 3.22 show that a vehicle traveling on dry pavement at 40 MPH will have a wheel lift off at 3.2 sec, but rollover will not occur. Unlike the previous cases, rollover will occur, however, at a vehicle speed of 60 MPH.

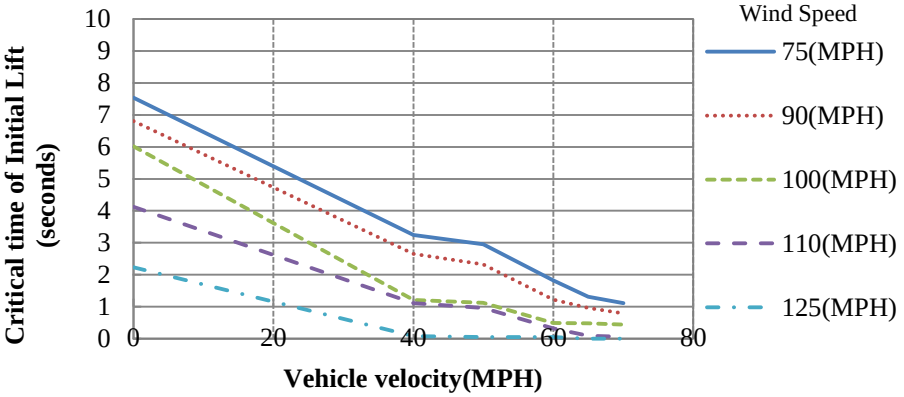

Figure 3.21: Critical sustained time for initial liftoff on dry pavement (μ=0.9) with 10% cargo load.

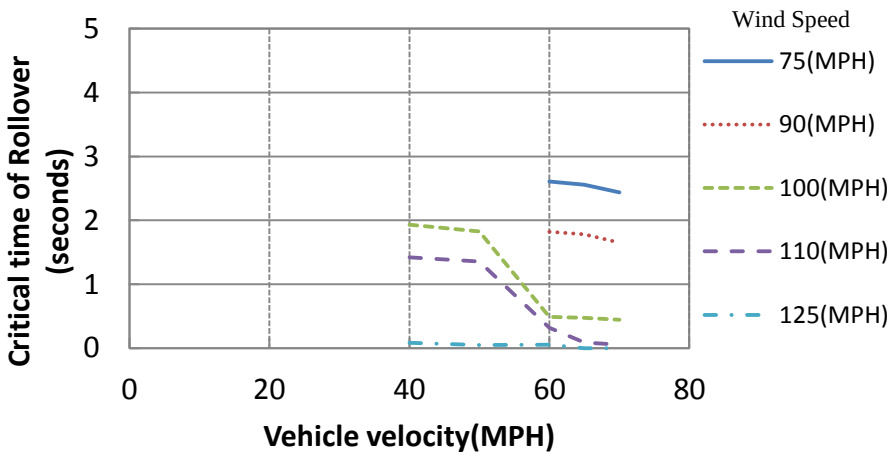

Figure 3.22: Critical sustained time for rollover on dry pavement (μ=0.9) with 10% cargo load.

Figure 3.23 to Figure 3.28 describe the response of a vehicle travelling on a wet road surface (COF = 0.5) with full, partial and no cargo loading condition. For the full load case, Figure 3.23 and Figure 3.24 show the critical sustained times for initial liftoff and the onset of a rollover, respectively. The 0.5 value for the COF represented a wet surface. It is seen that at a vehicle speed of 40 MPH, it would take a 75 MPH wind 4.6 sec to cause a liftoff. However, at this vehicle speed and wind speed, no rollover would occur. This is similar to the case of a dry surface.

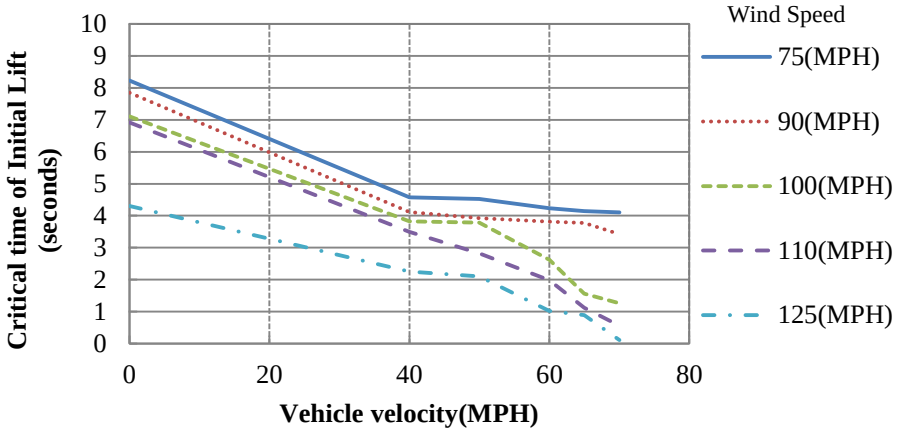

Figure 3.23: Critical sustained time for initial liftoff on wet pavement (μ=0.5) with full cargo load.

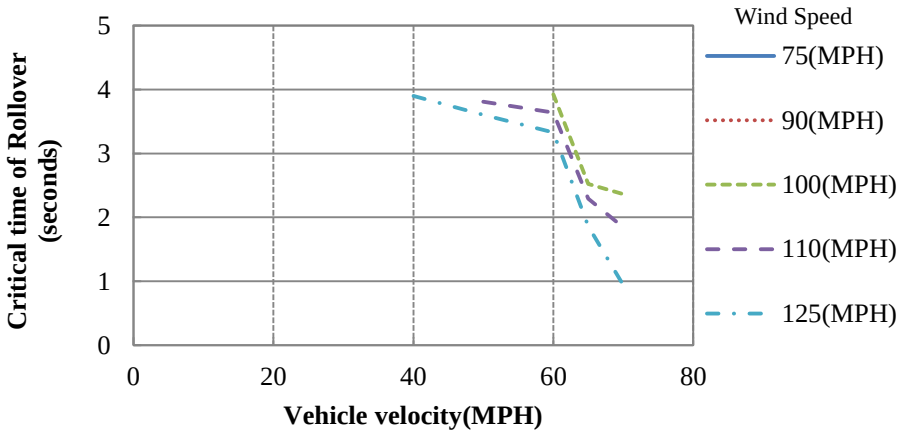

Figure 3.24: Critical sustained time for rollover on wet pavement (μ=0.5) with full load.

Figure 3.25 and Figure 3.26 show the results for a truck with 50% cargo loading traveling on wet pavement. At 40 MPH a steady wind of 75 MPH lasting for 3.5 sec would be sufficient for liftoff. Similar to the above results, no rollover would occur.

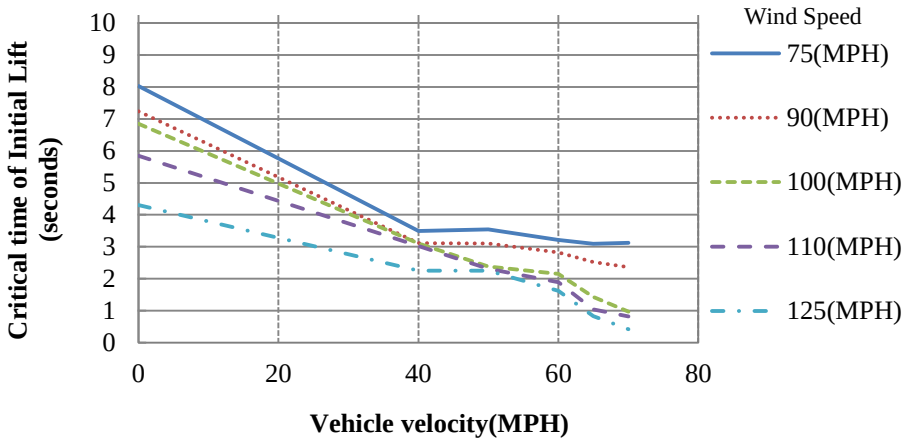

Figure 3.25: Critical sustained time for initial liftoff on wet pavement (μ=0.5) with 50% cargo load.

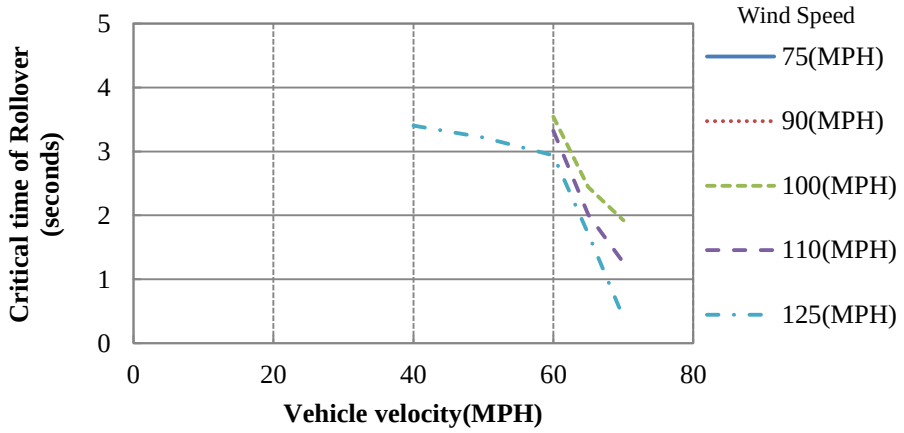

Figure 3.26: Critical sustained time for rollover on wet pavement (μ=0.5) with 50% cargo load.

For the case with a 10% cargo load, Figure 3.27 and Figure 3.28 show that a vehicle traveling on wet pavement at 40 MPH will have a wheel lift off at 3.2 sec, but rollover will not occur. Unlike the previous cases, rollover will occur, however, at a vehicle speed of 60 MPH.

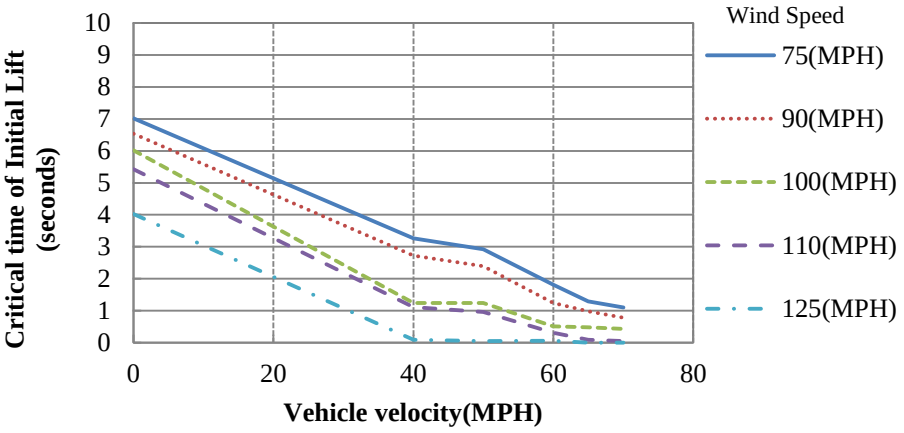

Figure 3.27: Critical sustained time for initial liftoff on wet pavement (μ=0.5) with 10% cargo load).

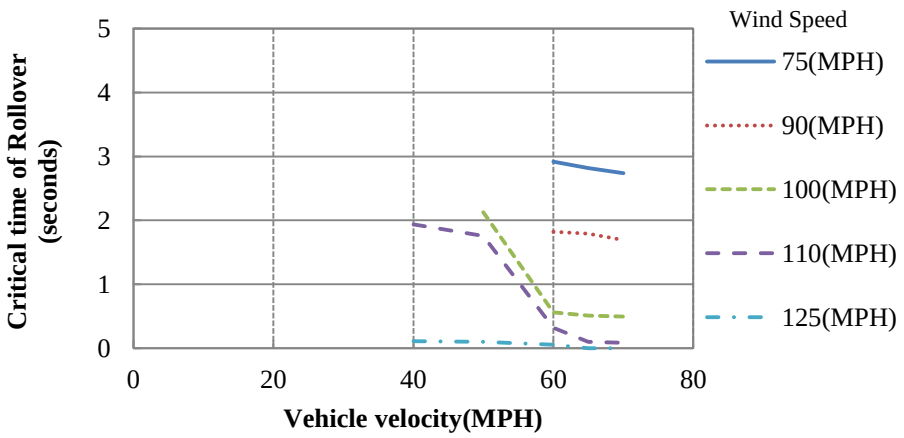

Figure 3.28: Critical sustained time for rollover on wet pavement (μ=0.5) with 10% cargo load.

As far as critical sustained times go, there does not seem to be any significant difference between the results for dry (COF = 0.9) and wet pavement (COF = 0.5).

3.2.1.3. Sensitivity Analysis

In addition to the deterministic LS-DYNA simulations described above, a sensitivity study using LS-OPT was performed for further identification of the correlation between the input parameters and the response of the vehicle. The sensitivity study was conducted for four variables: velocity of the wind (converted to the pressure exerted on the vehicle), velocity of the vehicle, friction coefficient between the tires and the ground and the mass of the cargo. The response variables were the lateral displacement of the center of gravity of the truck with cargo and the rotations about the longitudinal (x) and vertical (z) axes. The D-optimal point sampling method was used to choose 40 input vectors. D-optimal design is a method using an optimized subset of Factorial designs to minimize the approximation error. Bounds on the selected input parameters are listed in Table 3.5.

Table 3.5: Parameter screening variables

Parameter	Description	Lower bound	Upper Bound
rho	scaling factor for density of cargo	0.1 (0.28 tonne)	1.0 (2.8 tonne)
fric	friction coefficient between the ground and tires	0.1	0.9
velf	scaling factor for the prescribed velocity	1 (40 mph)	1.75 (70 mph)
presf	scaling factor for the lateral wind pressure	1 (206.61Pa – 40 mph)	14.062 (2905.4 Pa – 150 mpa)

The Radial Basis Function Network (RBFN) was chosen for building the Response Surface (RS). The sensitivity analysis was performed using the Sobol Indices technique (see LS-OPT manual for reference). Figure 3.29 shows the results of this study. The most important variable for the rotation of the vehicle turned out to be the wind pressure. Variations in values of the pressure scaling factor were responsible for over 70 % of the variations in the response of the vehicle. The friction coefficient was responsible for

about 20 % of them. The density of the cargo was responsible for about 6 % of changes in the vehicle response.

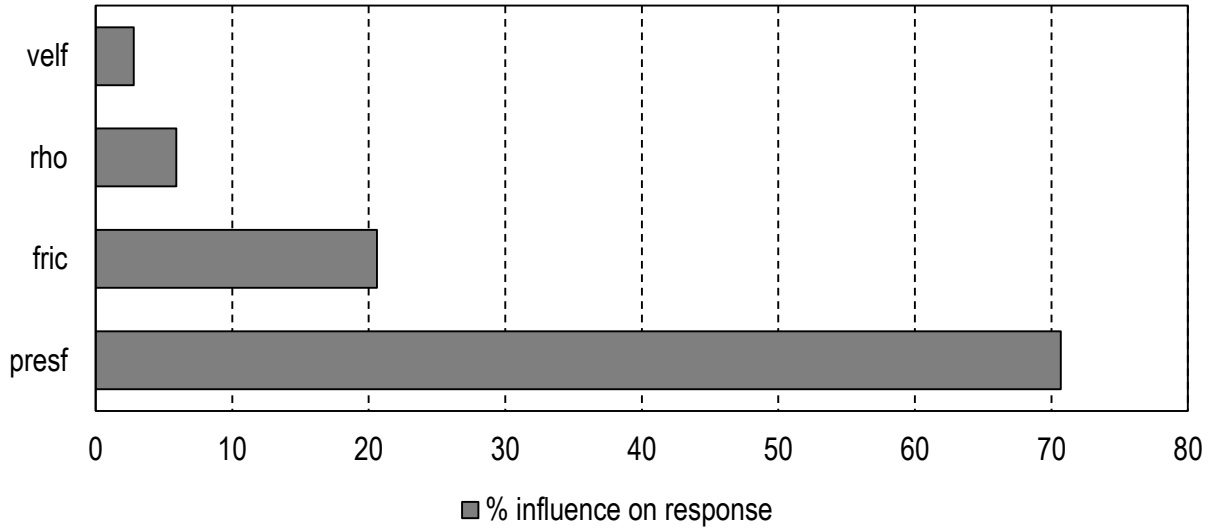

Figure 3.29: Sensitivity analysis results for the initial model

The response of the vehicle as a function of mentioned parameters is highly nonlinear and 40 simulation points used to create RBFN are not enough to provide enough accuracy for the results – the fitted surface is not capturing well the real response in the simulation points. For very nonlinear responses more simulations need to be performed to cover more precisely the design space and to build more accurate RS. The above results should be used for initial variable screening purposes only.

In the second set of runs velocity of the vehicle was eliminated from the list of input variables. Its influence on the response is minimal and keeping it in this sensitivity study only introduces large number of simulations. It was set as a constant at the level of 40 mph as the drivers would naturally slow down at the adverse weather conditions. With the three parameters left (see Table 3.6) Full Factorial point sampling was used to select points for consecutive simulations. In factorial method the points are equidistant, what makes the space evenly covered with a grid of 5^3 = 125 simulation points with 5 being the number of points in one dimension of that space. For the initial set of four parameters that number would have to be 5^4 = 625 in order to keep the same level of accuracy.

Table 3.6: Parameter screening variables

Parameter	Description	Lower bound	Upper Bound
rho	scaling factor for density of cargo	0.1	1.0
fric	friction coefficient between the ground and tires	0.1	0.9
presf	scaling factor for the lateral wind pressure	1	14.062

Tripled number of the simulation runs for lower number of variables increases significantly the accuracy of the results in comparison to the first analysis. Figure 3.30 displays the results of sensitivity study analysis for it. The order of the significance of the variables did not change but their percentage contribution to the response did. The pressure scaling factor is responsible for about 61 % of the changes in the response, the friction coefficient for about 23 % and the remaining 17 % can be attributable to the scaling factor for the density of the cargo.

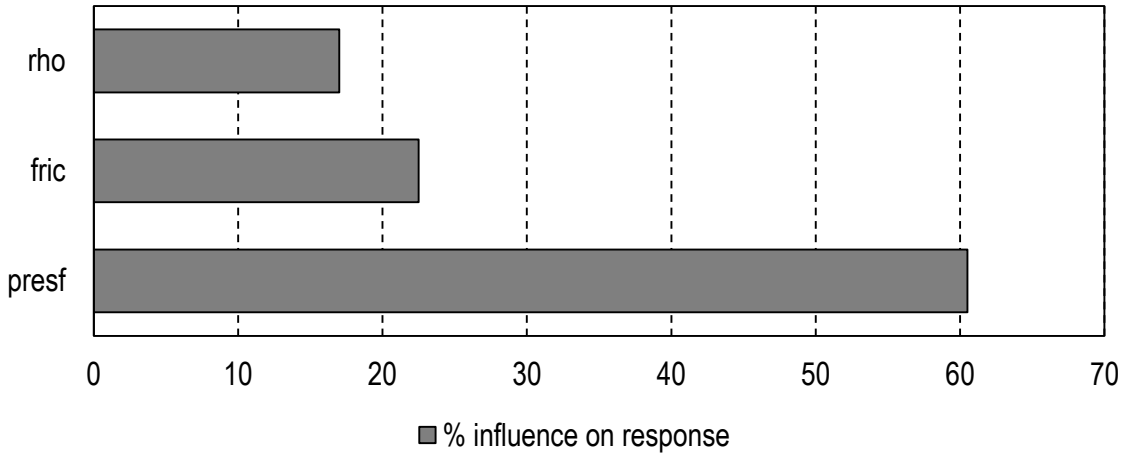

Figure 3.30: Sensitivity analysis results for the updated model

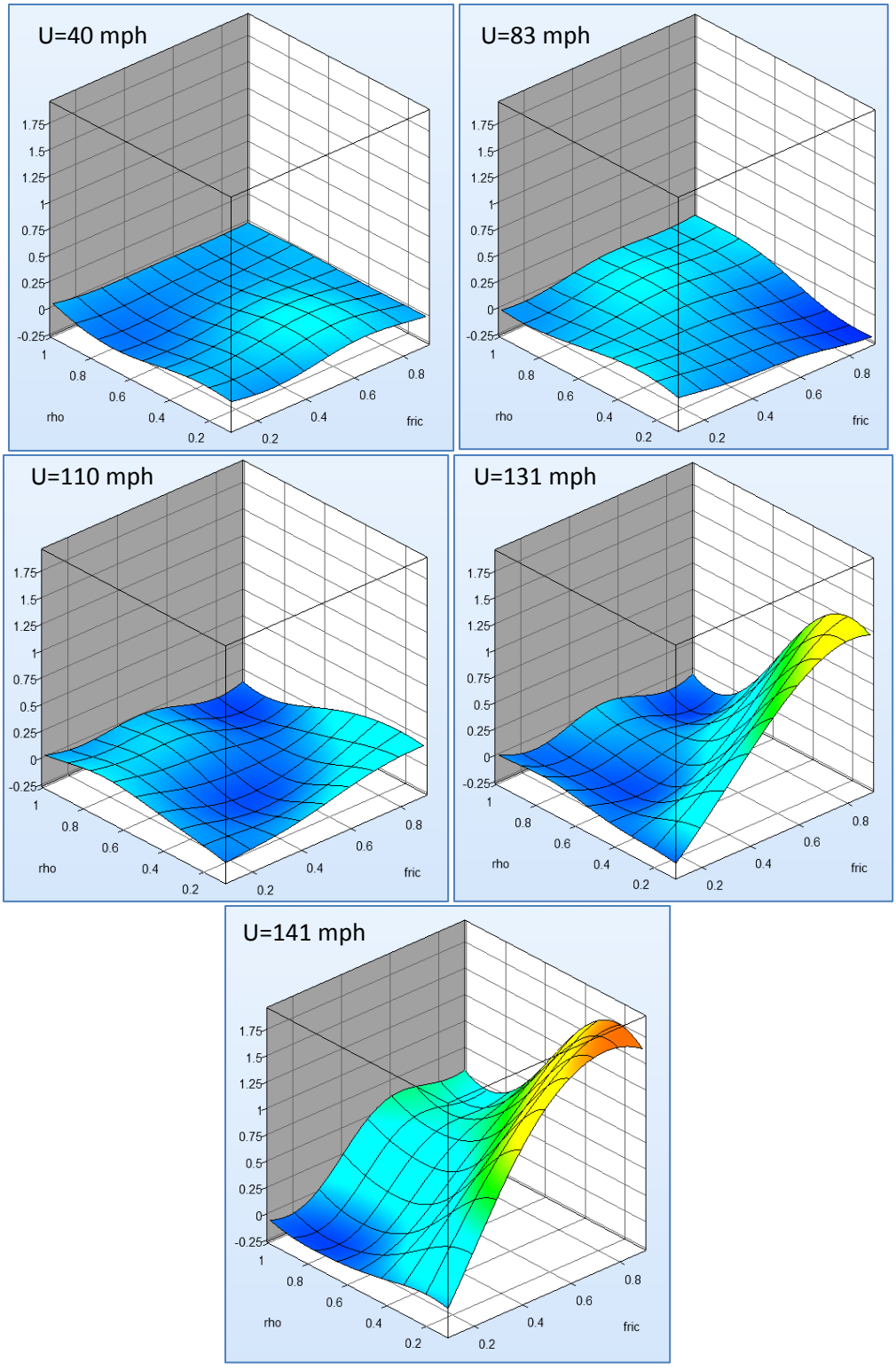

Figure 3.31: Approximate response surfaces for different values of pressure scaling factor

Figure 3.31 presents a set of plots for the fitted response surface as a function of friction coefficient and the scaling factor of the cargo's density. Six plots were prepared assuming different value of the third variable - the wind pressure scaling factor: 1, 4, 7, 10, 12, 14, which is equivalent to the wind speed of 40, 82.6, 109.8, 131.4, 141 and 150 mph. It can be noted that the non-zero rotation is only present in the plots for higher velocities of the wind.

The Parallel coordinate plot is shown in Figure 3.32. It displays all the entities studied (i.e. input variables) and responses on separate parallel axes. Also it connects with a line the input values that were used in one simulation with the responses obtained in that simulation. Each path can be separately highlighted in the LS-OPT GUI. Following the axis with the rotation about the x axis (response called *x_rot_cg_resp*) one can see that there were only two sets of values for that response – either close to zero, meaning no rotation of the vehicle or close to 1.6 radian, meaning 90 degree of rotation or full rollover. Also one can see that the paths to the 1.6 rad for the rotation only lead through the highest values of the pressure scaling factor. Note that the response is defined as a final value of the time history. Thus, for zero value of the rotation (*x_rot_cg_resp*) the vehicle could lift up at the initial stage of the simulation but at the end of it all the wheels would be on the ground again. The defined response does not make any distinction between normal driving, side slip or lift up without rollover cases. For that different function would have to be defined as the response.

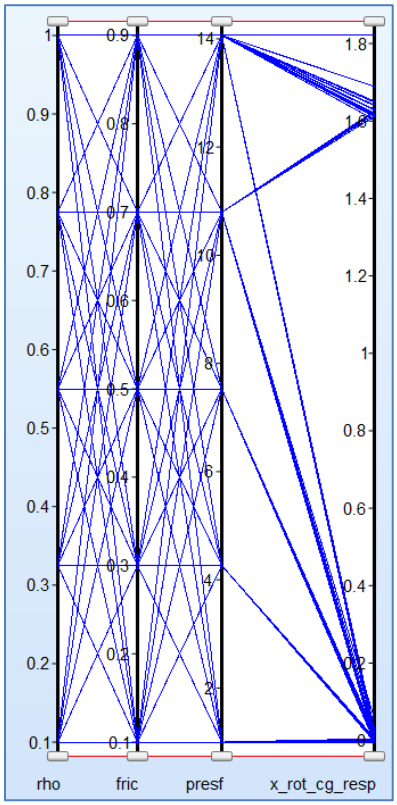

Figure 3.32: Parallel Coordinate plot

3.2.1.4. Reference:

1. Ford Single Unit Truck, Reduced model (35,353 elements), 11/3/2008.[online] Available at: < http://www.ncac.gwu.edu/vml/models.html> [Accessed 01 June 2011].
2. F800 Single Unit Truck Model: User Manual, National Transportation Research Center, Inc., November 2005.
3. http://www.vehix.com/car-reviews/1999/ford/f-800/vehicle-specifications
4. Park, S. and Bosch, H., "Influence of Cross-Tie Geometry and Details on Mitigation of Wind-Induced Vibrations, "Wind Induced Vibrations of Cable Stayed Bridges Workshop, St. Louis, MO, April 25-27, 2006.
5. Ley, H. Transportation Research and Analysis Computing Center (TRACC) Year 5 Quarter 3 Progress Report, ANL-11/TRACC-USDOT-Y5Q2, August 2011.

3.2.2. Electromagnetic Shock Absorber for Vehicle Stability under High Wind Conditions

The work done during the fourth quarter involved FEM simulations of the Ford F800 truck model to obtain stiffness and damping properties of the suspension system. All of the properties of the F800 truck have been found and suitable gain values have been found for each location. The evaluation of the EMSA quarter-car control model in Matlab-Simulink for each location of the truck has been completed. The results indicate an improvement for reduction of the suspended mass acceleration, while maintaining road holding ability and satisfying other requirements such as deflection limit of the suspension.

3.2.2.1. Simulation of theF800 Truck Model

The simulation to obtain the effective stiffness of the leaf springs in the suspension of the F800 truck was performed in a similar manner than the simulation to obtain the tire stiffness values. Almost every component/part was removed from the F800 model except for the wheel/tire assembly, the suspension assembly and a nearly rigid beam that is attached directly to the suspension as shown in Figure 3.33.

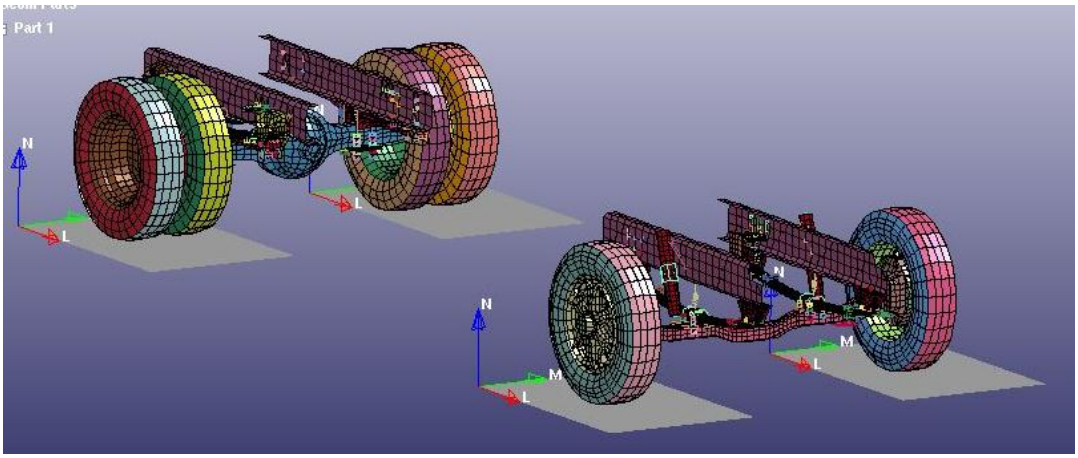

Figure 3.33: Screenshot of the suspension simulation

The nearly rigid beams density was increased to mimic the actual load of the full F800 truck model. After allowing the F800 to initialize, the movement of the wheel/tire assembly in Z-direction (vertical) was constrained to not move. A vertical displacement (prescribed motion) to the beam was then applied downward and the resulting reaction force from the wheel/tire assembly was recorded. Figure 3.34 is a plot of the reaction force from the wheel/tire assembly versus the deformation of the front passenger suspension. Notice in the very beginning the model is initializing.

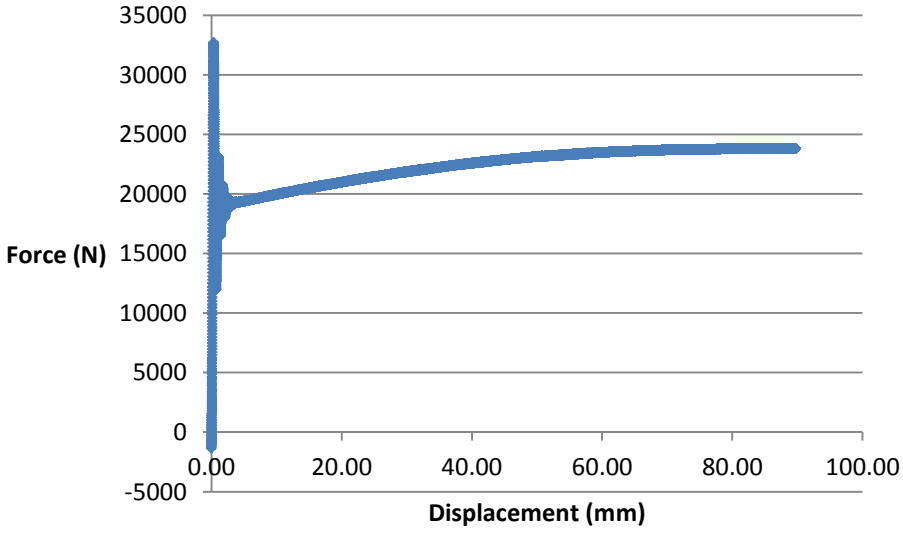

Figure 3.34: Force response vs. displacement of beam for front passenger location

Knowing that the maximum deformation for the suspension is around 40mm, Figure 3.35 shows the range of interest and a linear regression line. Note that the slope of line in Figure 3.35 is the effective stiffness of the suspension for the given location. The results for the front driver location are omitted for brevity given that they are nearly identical to what is shown in Figure 3.34 and Figure 3.35.

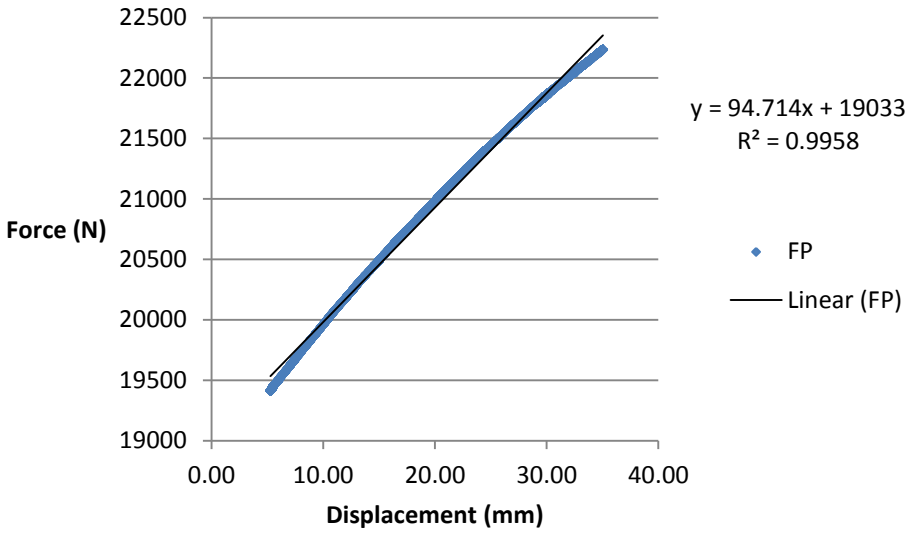

Figure 3.35: Force response vs. displacement for the range of interest

Figure 3.36 is a plot of the reaction force from the wheel/tire assembly verse the deformation of the rear driver suspension. Knowing that the maximum deformation for the suspension is around 40mm, Figure 3.37 shows the range of interest and a linear regression line. Note that the slope of the line in Figure 3.37 is the effective stiffness of the suspension for the given location. The results for the rear passenger location are omitted for brevity given that they are nearly identical to what is shown in Figure 3.36 and Figure 3.37.

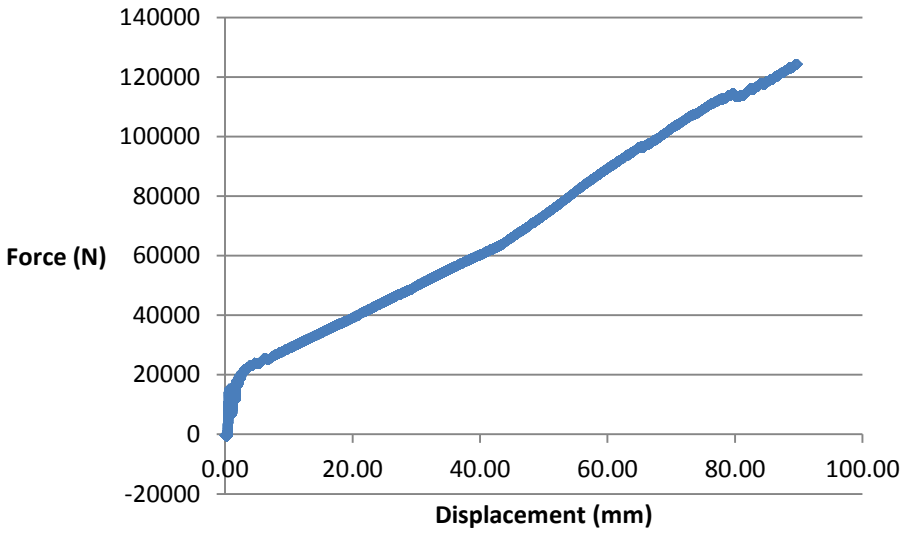

Figure 3.36: Force response vs. displacement of beam for rear driver location

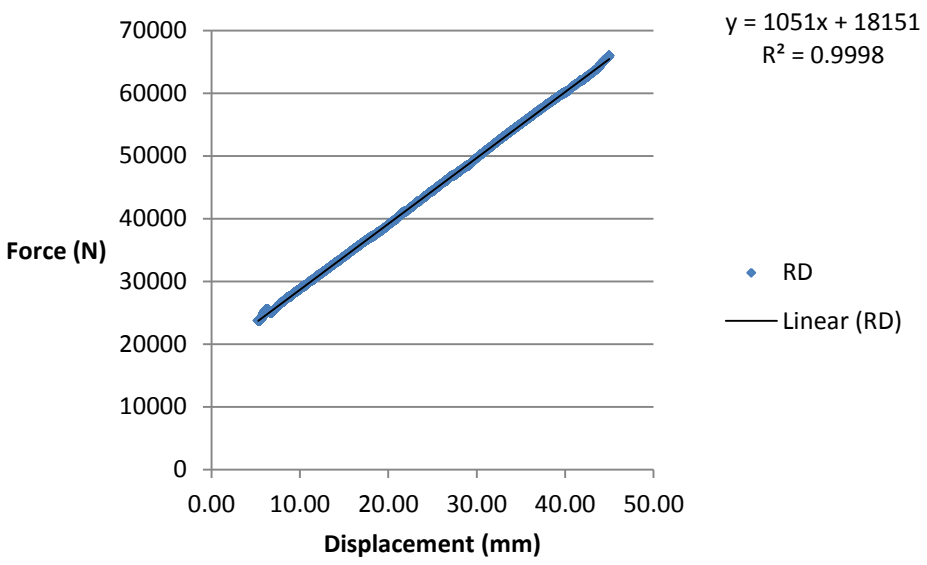

Figure 3.37: Force response vs. displacement for the range of interest

The stiffness values of the suspension for each location are shown in Table 3.7:. The percent difference for the front stiffness values is 0.19% and the percent difference for the rear stiffness values is 3.39%.

Table 3.7: Suspension stiffness values for each location

K_{RP}	1087300	N/m
K_{RD}	1051000	N/m
K_{FD}	94893	N/m
K_{FP}	94714	N/m

In order to obtain the damping coefficients for the suspension a vertical displacement (prescribed motion) was applied to the beam and then the beam was released, effectively allowing the system to vibrate freely. Figure 3.38 shows the free damped response of the beam for the front driver side.

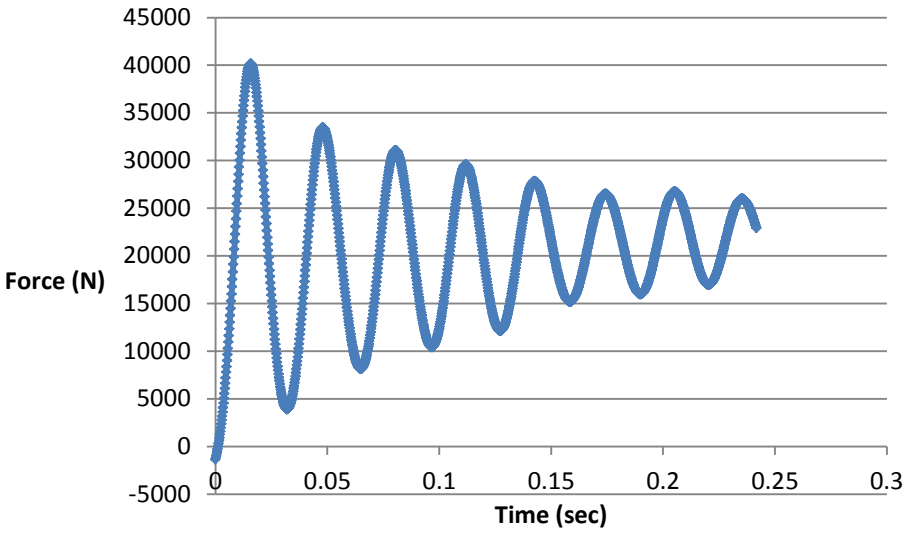

Figure 3.38: Front response vs. time for front driver location

The other locations had similar results and are omitted for brevity. The log-decrement method was applied to Figure 3.38 and after some calculations the damping coefficients were then determined. The damping values for the various locations of the suspension are shown in Table 3.8:.

Table 3.8: Damping coefficients of the suspension for each location

Rear Driver [Ns/m]	Rear Passenger [Ns/m]	Front Driver [Ns/m]	Front Passenger [Ns/m]
447.702	321.130	6407.560	6918.625

3.2.2.2. Controller Formulation

In order to find suitable gain values for the controller, the performance index needs to be defined. The performance index is user defined criteria based upon dynamics of the model and the states of interest [1]. The performance index is typically given in the form of an integral of a cost function, which is to be minimized. Shown in equation 3.1 is the general form of the performance index, where $L(X(t), u(t))$ is the cost function to be minimized. $X(t)$ is the state vector at time t and $u(t)$ is the desired force (see equation (8.14) in [2]).

$$I = \int_0^{t_f} L(X(t), u(t))dt \qquad 3.1$$

The cost function is shown in equation 3.2, where Q is a n x n constant coefficient diagonal matrix and R is a m x m constant coefficient matrix. The value of n is equal to the number of states and m is equal to the number of control inputs, so n is 4 and m is 1. Note, $L(X(t)\ and\ u(t))$ will be scalar values.

$$L\big(X(t), u_d(t)\big) = X^T(t) * Q * X(t) + u^T(t) * R * u(t) \quad 3.2$$

The product of $X^T(t) * Q * X(t)$ represents the cost associated with the states or the amount of time it takes to have them decay, the evaluation of this product is shown in equation 3.3.

$$X^T(t) * Q * X(t) = \ q_1 * X_1^2 + q_2 * X_2^2 + q_3 * X_3^2 + q_4 * X_4^2 \quad 3.3$$

The product of $u^T(t) * R * u(t)$ represents the cost associated with control or the amount of cost that will appropriately decay the response, the evaluation of this product is shown in equation 3.4.

$$u^T(t) * R * u(t) = \ r_1 * u^2 \quad 3.4$$

Note that Q and R are determined by the designer preference and that the larger the cost or weight associated with Q will in turn make the cost or weight associated with R smaller. When Q and R are determined, the gain values are found by using Matlab's built-in function "lqr". Shown in equation 3.5 is the Matlab command, where A and B are the matrices shown in equations (8.11) and (8.12) in [2].

$$K = lqr[A, B, Q, R] \quad 3.5$$

3.2.2.3. Matlab-Simulink Results

The current Matlab-Simulink model incorporates the EMSA model with the quarter-car control model as well as the input road profile. It includes a Matlab script or code that allows the user to input parameters/properties of the desired quarter-car model as well as modifying values that are used to formulate the matrix, K. After running the code, the Simulink model can then evaluate the dynamics of the quarter-car model given the properties of the system and the controller design. At this point, the data is then passed to Microsoft Excel for post-processing. The Excel file automatically calculates the

RMS (Root-mean-square) values for the states, $\ddot{x}_s$ and $\ddot{x}_u$ (The accelerations of the sprung and unsprung masses). The Excel file also creates two plots that critique the performance of the controller in terms of maximum suspension deformation and road holding ability. Multiple trials were performed using properties and gain values obtained from [3] and [4]. These trials were performed to ensure the correctness of the model.

Four more sets of trials were performed in order to obtain suitable gain values for each location of the vehicle. After the gain values were determined, the results were analyzed to ensure that the performance of the vehicle suspension system was improved in terms of comfort and road holding ability as well as satisfying the physical constraints. Shown in Figure 3.39 is the entire Simulink model, the block diagram of this model is shown in Figure 8.29 in [2]. It is very hard to understand the model by simply examining Figure 3.39 due to the details in the image.

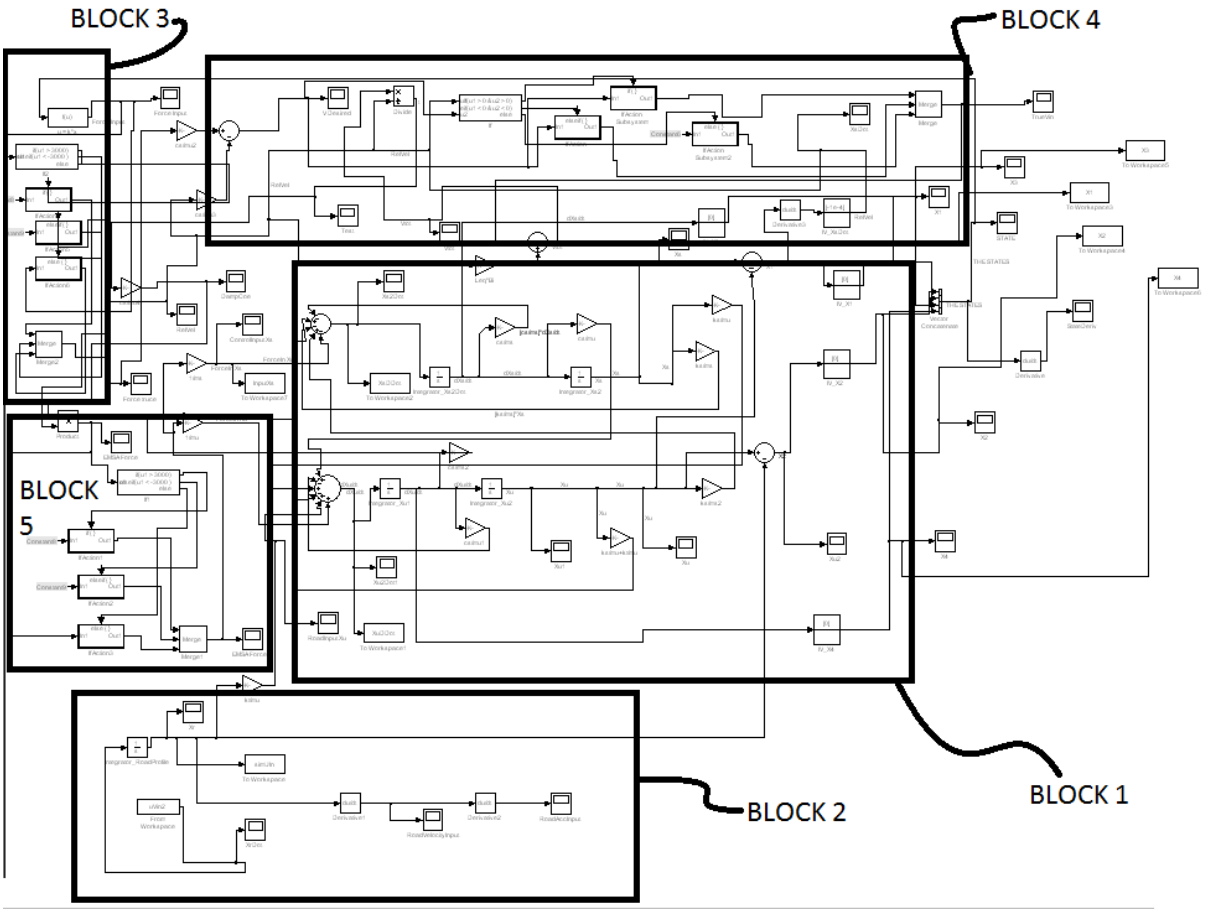

Figure 3.39: Screenshot of the entire Simulink model

In order to explain the model effectively, Figure 3.39 was separated into "Blocks" as shown. Block 1 is the quarter-car dynamics; this involves two 2nd order ordinary differential equations. In other words block 1 is basically equations (8.8) and (8.9) in [2]. Block 2 involves the road profile that represents the

road disturbance. Block 3 is the controller portion; this includes equation (8.14) in [2] and also has conditional statements that limit the desired force value due to the saturation or limit of the EMSA. Blocks 4 and 5 are the reverse model of the EMSA, which is based upon the desired force. They output the actual EMSA force that is then sent to Block 1. Blocks 4 and 5 also include two conditional statements. One conditional statement ensures proper operation of the EMSA by checking if the generated voltage is acting in the opposite direction then the desired voltage. The other conditional statement ensures that the EMSA force is limited to the absolute maximum producible force of the EMSA.

Since this model is designed for a quarter-car system, the front driver and passenger as well as the rear driver and passenger locations were analyzed using the Matlab-Simulink model and the results are compared with the passive systems. The most important aspects to consider are: the acceleration of the vehicle body, $\ddot{x}_s$, the tire deflection, X_2, the EMSA force, and the suspension deflection, X_1.

Shown in Table 3.9: are the gain values used for the front driver semi-active simulation. The road input for this simulation is shown in Figure 8.14 in [5] and it is assumed that the vehicle is traveling at a constant velocity of 30 m/s. For each simulation the road input remains constant as well as the vehicles velocity.

Table 3.9: Gain values for the front driver location

K_1	K_2	K_3	K_4
-1.717	18980.772	-96.404	441.724

Table 3.10: displays the RMS values of the passive and semi-active cases, note that a negative percent improvement indicates the opposite of improvement. Although the semi-active RMS value for the suspension deflection, X_1, is slightly larger than that of the passive value as shown in Table 3.10:, the suspension deflection in both cases are much lower than the deflection limit which is 0.004m.

Table 3.10: RMS value comparison for the front driver location

	Passive	Semi-Active	Percent Improvement
$\ddot{X}_s$	0.2182 $\left(\frac{m}{s^2}\right)$	0.1347 $\left(\frac{m}{s^2}\right)$	38.28
$\ddot{X}_u$	7.5412 $\left(\frac{m}{s^2}\right)$	0.6718 $\left(\frac{m}{s^2}\right)$	91.10
X_1	0.001862 (m)	0.001907 (m)	-2.40
X_2	0.000253 (m)	6.219E-05 (m)	75.40
X_3	0.01867 $\left(\frac{m}{s}\right)$	0.01884 $\left(\frac{m}{s}\right)$	-0.91
X_4	0.04274 $\left(\frac{m}{s}\right)$	0.01602 $\left(\frac{m}{s}\right)$	62.51

Figure 3.40 displays the plot of acceleration of the vehicle body for both passive and semi-active cases. The tire deflection plot for both cases is shown in Figure 3.41. Figure 3.42 is a plot of the suspension deflection for both cases. The EMSA force plot is shown in Figure 3.43.

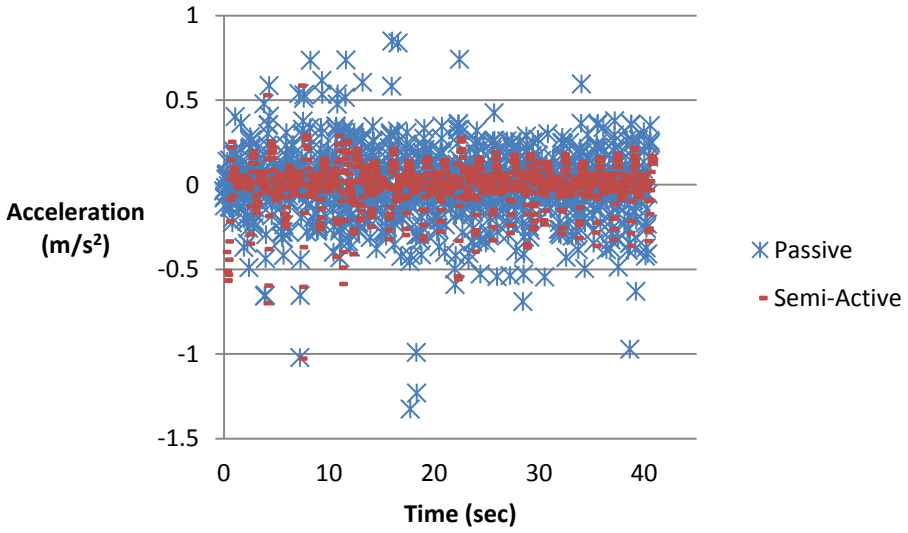

Figure 3.40: Front driver vehicle body acceleration

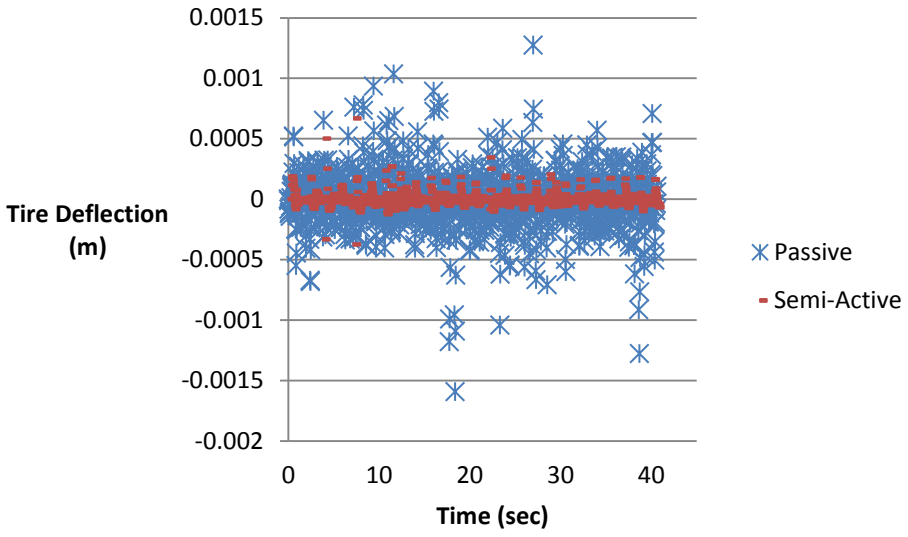

Figure 3.41: Front driver tire deflection

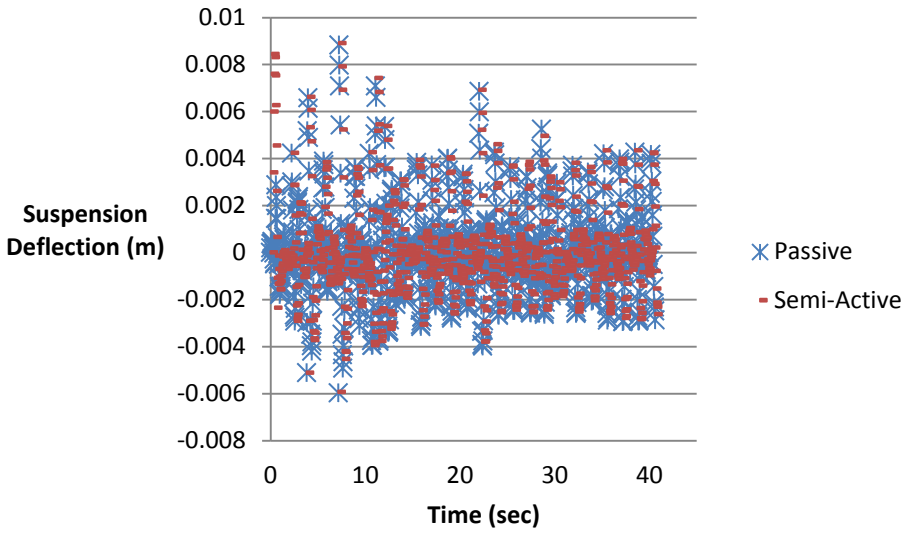

Figure 3.42: Front driver suspension deflection

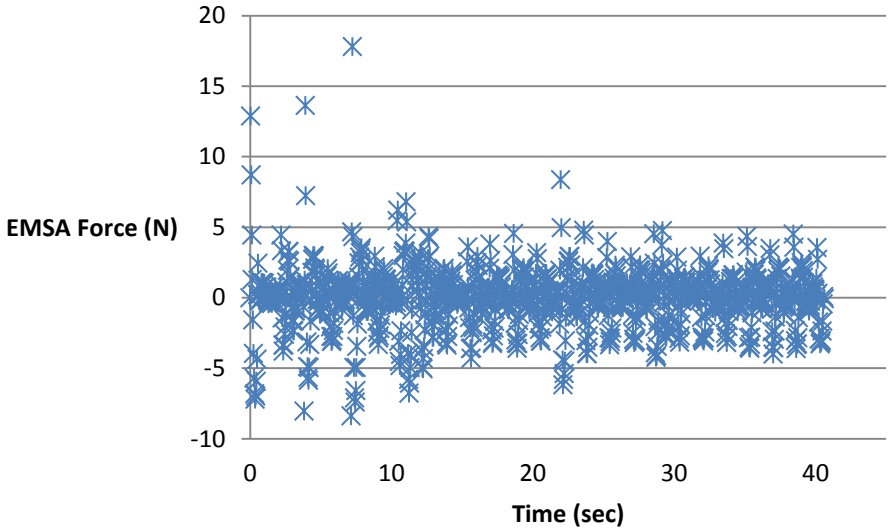

Figure 3.43: Front driver EMSA force input

Shown in Table 3.11: are the gain values used for the front passenger semi-active simulation. Notice that these gains are very close in magnitude to the gains shown in Table 3.9:. The plots for the front passenger location of the acceleration of the vehicle body, $\ddot{x}_s$, the tire deflection, X_2, the EMSA force, and the suspension deflection, X_1 are omitted for brevity since they nearly match Figure 3.40, Figure 3.41, Figure 3.42, and Figure 3.43. Table 3.12: displays the RMS values of the passive and semi-active cases.

Table 3.11: Gain values for the front passenger location

K_1	K_2	K_3	K_4
-1.720	18963.922	-90.200	411.007

Table 3.12: RMS values for the front passenger location

	Passive	Semi-Active	Percent Improvement
$\ddot{X}_s$	0.2275 $\left(\frac{m}{s^2}\right)$	0.1255 $\left(\frac{m}{s^2}\right)$	44.84
$\ddot{X}_u$	6.3040 $\left(\frac{m}{s^2}\right)$	0.5963 $\left(\frac{m}{s^2}\right)$	90.54
X_1	0.001783 (m)	0.001748 (m)	1.96
X_2	0.000227 (m)	5.91E-05 (m)	73.93
X_3	0.01825 $\left(\frac{m}{s}\right)$	0.01797 $\left(\frac{m}{s}\right)$	1.50
X_4	0.04412 $\left(\frac{m}{s}\right)$	0.01620 $\left(\frac{m}{s}\right)$	63.28

Shown in Table 3.13: are the gain values used for the rear driver semi-active simulation. Notice that these values are much different from those shown in Table 3.9: and Table 3.11:.

Table 3.13: Gain values for the rear driver location

K_1	K_2	K_3	K_4
-1244857.59	24766179.46	-262582.16	97799.05

Table 3.14: displays the RMS values of the passive and semi-active rear driver cases. Figure 3.44 is the plot of acceleration of the vehicle body for both passive and semi-active rear driver cases. The tire deflection plot for both cases is shown in Figure 3.45 for the rear driver location. Figure 3.46 is a plot of the suspension deflection for both cases. The EMSA force plot is shown in Figure 3.47.

Table 3.14: RMS values for the rear driver location

	Passive	Semi-Active	Percent Improvement
$\ddot{X}_s$	3.9274 $\left(\frac{m}{s^2}\right)$	1.0871 $\left(\frac{m}{s^2}\right)$	72.32
$\ddot{X}_u$	8.7202 $\left(\frac{m}{s^2}\right)$	2.6196 $\left(\frac{m}{s^2}\right)$	69.96
X_1	0.007336 (m)	0.001459 (m)	80.11
X_2	0.002125 (m)	0.000517 (m)	75.65
X_3	0.1921 $\left(\frac{m}{s}\right)$	0.04582 $\left(\frac{m}{s}\right)$	76.15
X_4	0.08165 $\left(\frac{m}{s}\right)$	0.02919 $\left(\frac{m}{s}\right)$	64.25

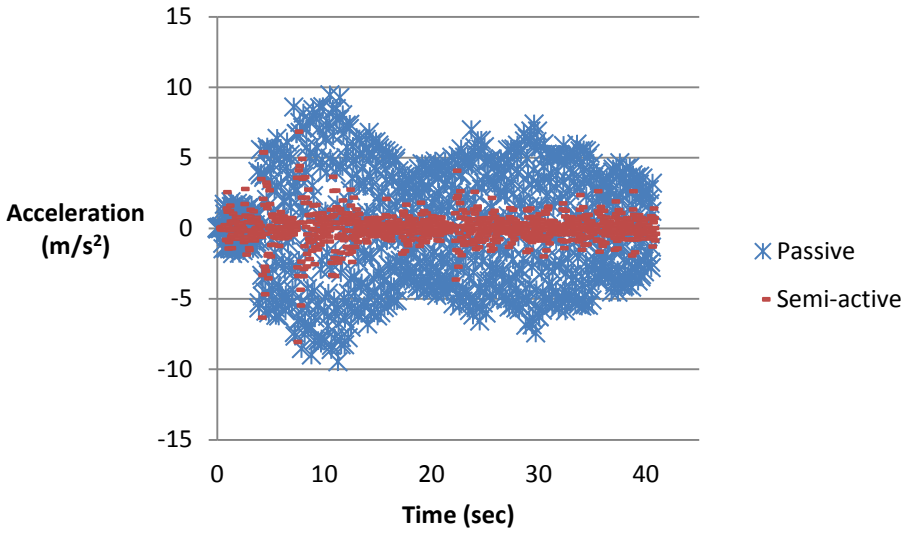

Figure 3.44: Rear driver vehicle body acceleration

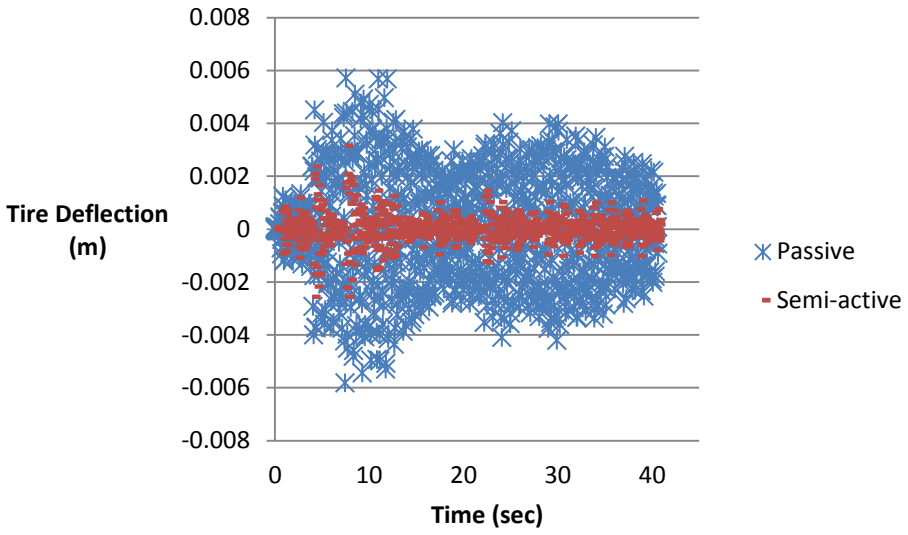

Figure 3.45: Rear driver tire deflection

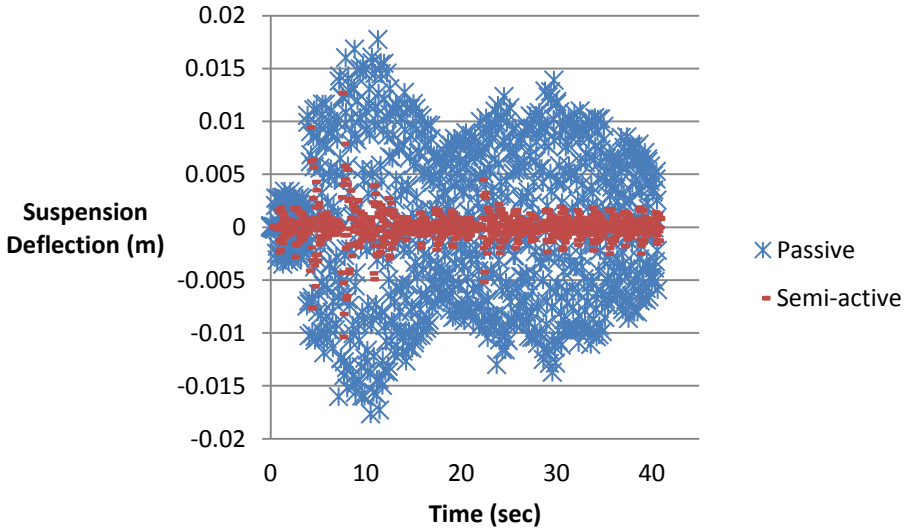

Figure 3.46: Rear driver suspension deflection

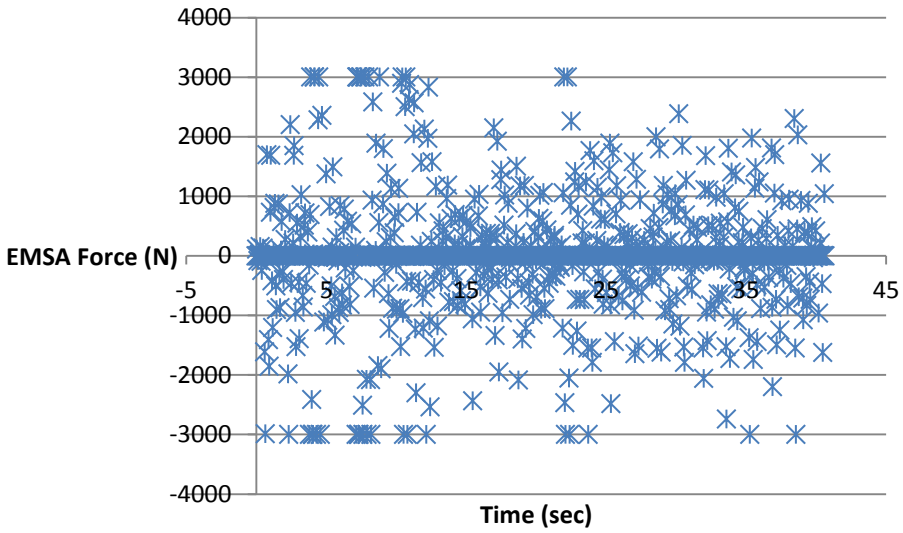

Figure 3.47: EMSA force for rear driver location

Shown in Table 3.15: are the gain values used for the rear passenger semi-active simulation. Notice that these gains are very close in magnitude to the gains shown in Table 3.13:. The plots for the rear passenger location of the acceleration of the vehicle body, $\ddot{x}_s$, the tire deflection, X_2, the EMSA force, and the suspension deflection, X_1 are omitted for brevity since they nearly match Figure 3.44, Figure 3.45, Figure 3.46 and Figure 3.47. Table 3.16 displays the RMS values of the passive and semi-active cases.

Table 3.15: Gain values for the rear passenger location

K_1	K_2	K_3	K_4
-1244858	24766185	-262582	97799.41

Table 3.16: RMS values for the rear passenger location

	Passive	Semi-Active	Percent Improvement
$\ddot{X}_s$	3.9274 $\left(\frac{m}{s^2}\right)$	1.0841 $\left(\frac{m}{s^2}\right)$	72.40
$\ddot{X}_u$	8.7116 $\left(\frac{m}{s^2}\right)$	2.6430 $\left(\frac{m}{s^2}\right)$	69.66
X_1	0.007336 (m)	0.001454 (m)	80.17
X_2	0.002125 (m)	0.000518 (m)	75.63
X_3	0.1921 $\left(\frac{m}{s}\right)$	0.04572 $\left(\frac{m}{s}\right)$	76.20
X_4	0.08159 $\left(\frac{m}{s}\right)$	0.02889 $\left(\frac{m}{s}\right)$	64.59

It is shown from the Matlab-Simulink model that the EMSA does offer an improvement in terms of reducing the acceleration of the sprung and unsprung masses. The front and rear locations have very different mass and suspension properties and that is why their respective gain values are very different. Future work will include the application of high wind loading.

3.2.2.4. References

1) Gordon, T.J.; “Non-Linear Optimal Control of a Semi-Active Vehicle Suspension System”, Chaos, Solutions And Fractals, Vol. 5, No. 9, 1995, pp. 1603-1617.
2) Ley, H. Transportation Research and Analysis Computing Center (TRACC) Year 5 Quarter 2 Progress Report, ANL-11/TRACC-USDOT-Y5Q2, May 2011.
3) Gao, H.; Lam, J.; Wang, C.; “Multi-objective Control of Vehicle Active Suspension Systems Via Load-dependent Controllers,” Journal of Sound and Vibration, Vol. 290, 2006, pp. 654-675.
4) Du, H.; Sze, K.Y.; Lam, J.; “Semi-active H[infinity] control of vehicle suspension with magneto-rheological dampers”, Journal of Sound and Vibration, Vol. 283, No. 3-5, 2005, pp. 981-996.
5) Ley, H. Transportation Research and Analysis Computing Center (TRACC) Year 5 Quarter 3 Progress Report, ANL-11/TRACC-USDOT-Y5Q2, August 2011.

Energy Systems Division
Argonne National Laboratory
9700 South Cass Avenue, Bldg. 362
Argonne, IL 60439-4815

www.anl.gov